博士論文

Coherent Control and Phase Measurement in Electron Quantum Interferometer

（量子干渉計における電子のコヒーレント制御と位相測定）

高田　真太郎

Coherent control and phase measurement in electron quantum interferometer

Shintaro Takada

Department of Applied Physics

The University of Tokyo

This dissertation is submitted for the degree of

Doctor of Philosophy

2014

Acknowledgements

The present work has been performed under the guidance of Professor Seigo Tarucha at Tarucha Laboratory, the department of Applied physics, University of Tokyo. First I would like to express my sincerest gratitude to Prof. Seigo Tarucha. Prof. Tarucha has given me exciting experimental topics and always encouraged me to work on it, which really motivated me. His advice taught me the importance to see experimental results from various points of view. I am really grateful to Assistant Professor Michihisa Yamamoto for teaching me not only the techniques but also the stance to face difficult experimental problems. Discussion with him always give me new insights into or deeper understanding of physics. I feel heartfelt gratitude to Dr. Christopher Bäuerle (Institute Néel, CNRS) for instructing me not only experimental techniques but also pleasure of studying physics always kindly. He also offered me the environment to perform the experiment when I could not do in Japan after the huge earthquake. I would like to express special appreciation to him for that.

I am grateful to Lecturer Akira Oiwa for supporting my device fabrication and experiments a lot. I owe a very important debt to the members of the *Wire group*, especially Mr. Kenta Watanabe (Fuji film), Mr. Shunya Nakamura (Asamitsu lab., Univ. of Tokyo) and Mr. Ryo Ito, who work with me on the experiments. I would like to thank Dr. Sylvain Hermelin (Université de Genéve), Dr. Tristan Meunier (Institute Néel, CNRS), Prof. Jan von Delft (LMU, Munich), Dr. Andreas Weichselbaum (LMU, Munich) and Dr. Arne Alex (LMU, Munich) for collaborating works and fruitful discussions.

The experiments described here relied on the exceptionally quiet wafers from Prof. Andreas D. Wieck (Ruhr-Universität Bochum). I am grateful to him. I would like to thank Mr. Katsuharu Yoshida (Tarucha-lab) for lots of help in device fabrication. Some of the device preparation were performed in NTT Basic Research Laboratories. I express my gratitude to people in NTT for kindly allowing me to use equipments. About understanding of our experiment, I especially thank Dr. Rui Sakano (ISSP, Univ. of Tokyo) for useful discussions about our results.

I was greatly supported by the members of Tarucha-Laboratory. Thanks to all of them. In particular discussions with Mr. Fujita and Mr. Yoneda always stimulated me to study

harder. I am very happy to work with them. I really enjoyed my research life for five years in Tarucha-lab. I gratefully appreciate the financial support from JSPS for the Research Fellow- ships that made it possible to complete my thesis. Lastly, I thank my parents and family for their encouragement, help during my master and Ph.D. course and throughout my life.

Abstract

This thesis presents experiments studying coherent electron transport in nanostructures. In coherent transport transmission phase of electrons plays an important role. Control of the phase enables leads to qubit operations and therefore can be applied to quantum information. Measurement of the phase also provides deep understandings of coherent scattering phenomena. The simplest way to control and measure the transmission phase of electrons is utilizing a quantum two-path interferometer.

We realize a *pure* two-path interferometer by employing a complex system of an Aharonov-Bohm ring and tunnel-coupled wires (chapter 3). Then we measure transmission phase shift across a quantum dot (QD). Firstly we focus on the Kondo regime (chapter 5), where $\pi/2$-phase shift resulting from the many-body singlet Kondo ground state is expected theoretically [1, 2]. We succeed in observing the $\pi/2$-phase shift when the temperature T is lower than the Kondo temperature T_{K}, with a pronounced $\pi/2$ plateau at the Kondo valley around $T \sim T_{\mathrm{K}}$. Above T_{K}, the phase shifts by more than $\pi/2$ at each Coulomb peak, approaching the behavior observed for the standard Coulomb blockade regime. We compare these results with 2-level numerical renormalization group calculations and find remarkable agreement. The work thus allows for obtaining a detailed and consistent understanding of the behavior of the Kondo phase shift. Secondly we measure the transmission phase shift across a QD with a relatively large number of electrons (chapter 6), where an universal phase behavior was observed in previous experiments [3, 4] regardless of intrinsic properties of the QD. In particular we study the QD around the crossover from single level to multi-level transport. In contrast to the previous experiments the universal phase behavior is not observed in our large QDs. This result suggests that the universal phase behavior is not so robust as expected from the previous experiments. For further understanding of the universal phase behavior we need more experiments to examine what kind of conditions are required to observe it.

Our original two-path interferometer also works as a flying charge qubit. We perform qubit operations about two independent rotation axes by electrostatic gate voltages in an AB ring and a tunnel-coupled wire respectively (chapter 4). From the temperature dependence we confirm that our flying qubit is highly coherent at low temperatures. Finally we study

electron transport by surface acoustic waves (SAWs). The SAW gives a way to control highly coherent single electrons, which is important to further improve the visibility of our flying qubit. Once a flying qubit with high enough visibility is realized, it is possible to create and confirm a non-local quantum entangle state [5]. Here we achieve a beam splitter for single flying electrons transferred by SAWs in a depleted tunnel-coupled wire (chapter 7). This technique is an important step to realizing the high visibility flying qubit and is a key tool for quantum electron optics using SAWs. We also develop a technique to send a single electron from a QD through an isolated quantum channel and to catch it at a distant QD with high efficiency (chapter 8). This result corresponds to the realization of a single electron source and detector for quantum electron optics using SAWs. Further more we show that the transfer of the electron can be triggered on a timescale shorter than the coherence time T_2^* of GaAs spin qubits. Therefore this technique answers potential scalability of the electron spin qubits.

Contents

List of Figures

Nomenclature

Roman Symbols

G	Conductance
e	Elementary charge $\simeq 1.60 \ldots \times 10^{-19}$
h	Plank constant $\simeq 6.62 \ldots \times 10^{-34}$

Greek Symbols

π	$\simeq 3.14\ldots$
$\boldsymbol{\sigma}$	Pauli matrices

Other Symbols

E_{F}	Fermi energy
$H_n(x)$	Hermite function
L_{m}	Mean free path
l_ϕ	Phase relaxation length
l_{th}	Thermal diffusion length for diffusive systems, thermal length for ballistic systems
m^*	Effective mass ($m^* \approx 0.067 m_e$ for a GaAs-based semiconductor)
m_e	Mass of electron, $m_e \simeq 9.10 \ldots \times 10^{-31}$
τ_ϕ	Phase relaxation time
T_{K}	Kondo temperature
v_{F}	Fermi velocity

Acronyms / Abbreviations

1D One dimension or one dimensional

2DEG 2 dimensional electron gas

AB Aharonov-Bohm

CI Constant Interaction

CP Coulomb peak

FFT fast Fourier transform

FWHM Full width of half maximum

HEMT High mobility electron transistor

IDT Interdigital transducer

MBE Molecular beam epitaxy

QD Quantum dot

QPC Quantum point contact

RF Radio frequency

SAW Surface acoustic wave

SCR Strong Coupling Regime

SEM Scanning electron micrograph

UCF Universal conductance fluctuation

WCR Weak Coupling Regime

Chapter 1

General introduction

The continuous need for miniaturization and increase in speed of microelectronic devices lead industry as well as the scientific community to a world where quantum effects are crucial at the nanoscale. Understanding and harnessing the quantum mechanical behavior of electrons in nanoscale circuits is the object of intensive work. Recent advances in nano-fabrication and semiconductor technologies enable us to design and fabricate nano- and micro-structures, where the phase relaxation length is longer than the device size and hence electron-transport becomes coherent. In such coherent transport, the transmission phase of an electron is the key ingredient. Indeed this is the case for a variety of quantum interference phenomena such as the Aharonov-Bohm (AB) effect, universal conductance fluctuations, weak localization etc. observed to date. To fully characterize the coherent transport, study of transmission phase is required. However it cannot be directly measured by normal conductance measurement since conductance is proportional to the square modulus of transmission coefficient as known from the Landauer-Büttiker formula [6, 7].

The simplest way to measure the transmission phase should be to utilize a quantum two-path interferometer. Numerous attempts to realize a two-path interferometer have been made using an AB interferometer [8–10]. However in a two-terminal AB ring, gauge invariance and time reversal symmetry between macro-scale contacts impose a boundary condition, the so-called *phase rigidity* for the electron transport, in which linear conductance is an even function of the magnetic field (Onsager's law) [7, 11]. The two-path contribution is always accompanied by complicated multi-path interference to satisfy the boundary condition, which scrambles the quantum phase difference between the direct two paths. To avoid the phase rigidity and to realize a two-path interferometer, a multi-terminal AB interferometer has been employed in a series of pioneering experiments by a group of the Weizmann Institute in Israel [3, 4, 12, 13]. Lifting of the phase rigidity is then verified by

the observation of a smooth phase shift induced by a gate voltage, i.e. each conductance matrix element does not have to be an even function of the magnetic field. The transmission phase shift across a quantum dot (QD) has been intensively studied, where the phase behavior described by Friedel's sum rule [14] and the one reflecting spin screening of the many-body singlet ground state in the Kondo regime [2] are predicted. The transmission phase contains complementary information to the conductance and gives a deep insight into the understanding of such scattering problems.

The π-phase shift across a Coulomb peak in the Coulomb blockade regime as expected from Friedel's sum rule was observed in the multi-terminal AB interferometer [3]. However unexpected results were reported: universal phase lapse in many-electron QD [3, 4] and the phase behavior contradicting to the theoretical expectations [2, 15] in the Kondo regime [12, 13]. On the other hand it was pointed out theoretically that in a multi-terminal AB interferometer, the two-path contribution is properly extracted only when the interferometer is under the appropriate conditions [16–18]. Otherwise, multi-path contributions might smear the correct transmission phase. This may not be ruled out in the multi-terminal AB interferometer when gate voltages of the QD are varied to change the transmission phase. A new scheme for measuring the transmission phase across a QD, in which contributions from multiple paths are safely excluded, is therefore required.

In addition, once electrical control of the two-path interferometer becomes possible, it can provide quantum information with flying qubits defined by propagating electrons between the two paths [19, 20]. An electron confined in semiconductor QDs is considered as a promising candidate for a qubit since solid-state systems are assumed to be advantageous to realize scalable quantum computers due to the similarity of such devices with classical ones. Both spin and charge degrees of freedom are pursued and basic operations have already been performed [21–24]. However as these qubits are static in QDs, creation of a non-local entanglement, which is a key concept in quantum information, requires to combine them with other techniques to transfer a qubit from one place to another. In this respect coherent transfer of a single electron between distant QDs should be important [25, 26], which makes it possible to transfer information between separated static qubits. This technique is also attractive as a single electron source and detector for quantum electron optics, aiming at the realization of photon experiments with flying electrons in nanostructures [27–31]. On the other hand a flying qubit is an architecture, where a quantum state is controlled during transfer, and hence it should be more suitable to create a non-local entangled state compared to static qubits. The solid-state realization of a non-local entanglement known as an essential quantum mechanical state, is not only attractive for understanding fundamen-

tals of quantum physics but also inevitable for constructing scalable semiconductor quantum information devices in which many qubits are manipulated.

1.1 Motivation of the present work

As mentioned above, a quantum two-path interferometer is a extremely useful tool to study transmission phase shift across a QD and also works as a flying charge qubit. However due to the boundary condition for linear transport it is not easy to realize a *true* two-path interferometer in solid-state electronic systems. The motivation of the present work is to realize an original *true* two-path interferometer utilizing an AB ring with tunnel-coupled wires and pursue the application of the interferometer for measurements of the transmission phase across a QD and a flying charge qubit.

Regarding the transmission phase across a QD, we focus on the two different regimes. One is the phase behavior in the Kondo regime, where a $\pi/2$-phase shift reflecting spin screening by a many-body singlet ground state is expected at $T \lesssim T_{\mathrm{K}}$ but which has stayed elusive until now. The other one deals with a QD with a relatively large number of electrons, where the universal phase lapse between Coulomb peaks was observed in previous experiments [3, 4]. Appearance of the phase lapses between Coulomb peaks itself can be explained by theory [32]. However the origin of its universality in a relatively large QD is not well understood since only a few experimental works related to this issue have been reported. We address this issue in the present thesis.

Concerning the application for a flying qubit, we demonstrate how our original two-path interferometer works as a flying qubit and actually perform full electrical control of the single qubit. The robustness of the operation as a function of temperature is also examined and its scalability is discussed.

Finally we study electron transport by surface acoustic waves (SAWs) [33]. It allows us to manipulate highly coherent single flying electrons without backscattering, which is necessary to improve the fidelity of our flying qubit for testing a non-local entanglement. We manipulate single electrons in a depleted tunnel-coupled wire by injecting electrons one by one using the potentials of the SAWs. We realized a beam splitter operation for single electrons with much higher fidelity than that for ballistic electrons. This is an important step towards realization of a high fidelity flying qubit. Further more a beam splitter for single flying electrons is a key component to perform quantum electron-optical experiments in a single electron unit. We also perform single electron transfer between distant QDs through a depleted quantum channel using a SAW [25, 26]. This technique opens a way to generate

a non-local entanglement in combination with static qubits. It can also be used as a single electron source and detector for quantum electron optics.

1.2 Organization of the thesis

The organization of the thesis is as follows: in Chapter 2 we review the basic concepts to understand this thesis, including the quantum wire, the quantum dots, some properties of coherent electron transport, etc. Chapter 3 describes the distinct interference features observed in an AB ring with a tunnel-coupled wires. We explains how can we understand the appearance of the distinct interferences and how to realize a *true* two-path interference. From Chapter 4 to 6, we show experimental results acquired by using the two-path interferometer realized in Chapter 3. In Chapter 4 we demonstrate full flying charge qubit operations by means of electrostatic gate voltages. Then we discuss the scalability of the flying charge qubit. Chapter 5 is distributed to study the transmission phase shift across a QD in the Kondo regime. We reveal the phase behavior from the strong Kondo correlation regime $T < T_{\mathrm{K}}$ to the weak Kondo correlation regime $T \gg T_{\mathrm{K}}$ across the crossover regime $T \sim T_{\mathrm{K}}$. In Chapter 6 we investigate the universal phase behavior in QDs with a relatively large number of electrons. In particular we focus on the crossover region from single-level to multi-level transport. In Chapter 7 electron transport by SAWs is studied to realize a high fidelity flying charge qubit. As a first step, we perform the control of single flying electrons transferred by SAWs in a depleted tunnel-coupled wire. Finally in Chapter 8 we develop a technique to transfer single electron between distant QDs through a depleted quantum channel using a SAW. The possibility to create a non-local quantum entanglement is also pursued by sending one of two electrons in a QD to the other separated QD. We show that such an electron transfer can be performed within typical spin coherence time in GaAs based QDs.

Chapter 2

Background

A brief review of backgrounds needed for understanding experimental results of the present thesis are described in this chapter. First in section 2.1 a quantum wire, a quasi one dimensional system, is dealt with, and we explain its specific features. Next coherent properties of electron transport are discussed in section 2.2. In the next section 2.3, characteristic features of a quantum dot are shown. Section 2.4 describes the Kondo effect in a QD, which is known as a typical many-body correlation. Then in section 2.5 theoretical expectations and preceding experimental results about transmission phase across a quantum dot are explained. Finally section 2.6 explains how to generate a surface acoustic wave and transport electrons by it.

2.1 Quantum wire

2.1.1 2 dimensional electron gas

Since 1970s, development of ultra thin film deposition technique by molecular beam epitaxy (MBE) allows to fabricate heterojunctions with flatness in the atomic scale. In a GaAs/AlGaAs heterojunction electrons are accumulated at the heterointerface due to the band gap discontinuity between the two semiconductors. Fig.2.1 shows the conduction band edge profile of a GaAs/AlGaAs high electron mobility transistor (HEMT). The structure consists of a thick undoped GaAs layer, undoped AlGaAs spacer, a Si-doped AlGaAs layer and GaAs cap layer. The conduction band of the GaAs thick layer bends due to the electric field between the spatially separated electrons and donors, and this gives rise to the formation of a triangular potential well at the GaAs/AlGaAs interface. Electrons, provided by the Si donors, are trapped in this well, and their motion is quantized in the growth direc-

tion. If the well contains only one occupied subband, an ideal 2 dimensional electron gas (2DEG) is formed.

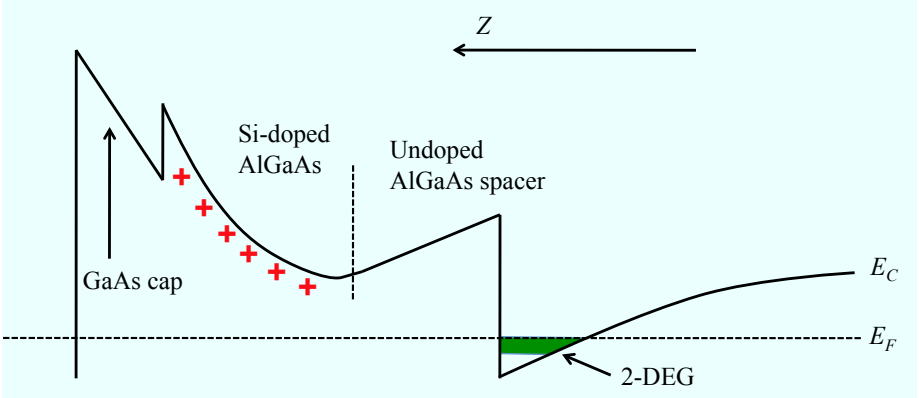

Fig. 2.1 The conduction band edge profile of a GaAs/AlGaAs high electron mobility transistor (HEMT).

2.1.2 Quantum wire

A quantum wire is a quasi one-dimensional system, in which an energy spectrum of an electron is quantized about two dimensions. In mesoscopic systems, a quantum wire formed in a 2DEG using a split gate technique has been widely used (See Fig.2.2). By applying negative gate voltage to split gates, electrons underneath these are depleted and a narrow strip of electrons is left. If the width of this strip is comparable to the Fermi wavelength of the 2DEG, one-dimensional channels are formed inside the strip. When the gates are more negatively biased, the depletion regions spread out. Then the conducting channel is narrowed and eventually pinched off.

The confinement potential for electrons in the y-direction (Fig.2.2) is approximated by a parabolic potential since the realistic wire width is much smaller than the distance between the metal split gates. If the potential in the x-direction is neglected, the Hamiltonian for the wire is

$$H = \frac{\boldsymbol{p}^2}{2m^*} + \frac{1}{2}m^*\omega^2 y^2 \,, \tag{2.1}$$

where m^* is effective mass ($m^* \approx 0.067 m_e$ for a GaAs-based semiconductor). By solving

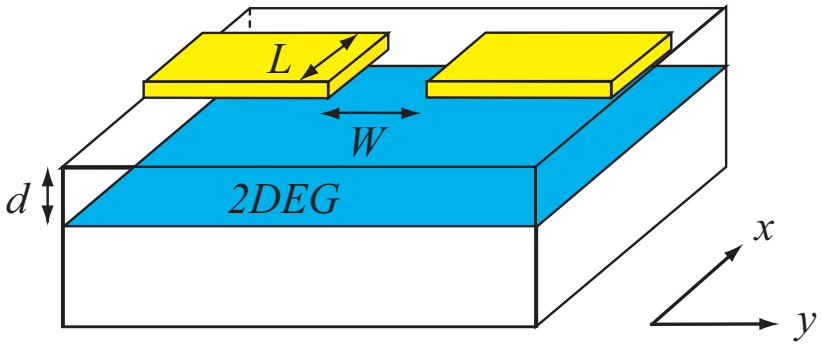

Fig. 2.2 A schematic figure of a Schottky split-gate (Width W and Length L) wire device fabricated on a wafer having a 2DEG (depth d).

the Schrödinger equation, total energies and eigenstates are derived:

$$E_{n,k_x} = \frac{\hbar^2 k_x^2}{2m^*} + \left(n+\frac{1}{2}\right)\hbar\omega \qquad n = 0,1,2,\ldots \tag{2.2}$$

$$\psi_{n,k_x}(x,y) = (\pi^{\frac{1}{2}} l 2^n n!)^{-\frac{1}{2}} \exp(ik_x x) H_n\left(\frac{y}{l}\right) \exp\left(\frac{y^2}{2l^2}\right) , \tag{2.3}$$

where k_x is the Fermi wave vector of the one-dimensional electron system, $l = \sqrt{\frac{\hbar}{m^*\omega}}$ is the spread of the wave function, H_n is the Hermite function, and n represents the subband index. Since the confinement potential can be modulated by the Schottky gate voltage V_g, the Fermi wave vectors and electron density in the wire are controlled by V_g.

The density of states in this quantum wire is the summation of the density of states in each subband:

$$D(E) = \sum_{E_n \le E} D_n(E)$$

$$= \sum_{E_n \le E} \frac{g_s}{h} \sqrt{\frac{m^*}{2(E-E_n)}} \tag{2.4}$$

$$E_n = \left(n+\frac{1}{2}\right)\hbar\omega , \tag{2.5}$$

where E_n is the energy of the n-th subband bottom and g_s is the spin degeneracy.

Transport properties of a quantum wire have been studied for the past more than 25 years. One of the most characteristic features of this system is quantization of conductance. At sufficiently low temperatures, a mean free path L_m in GaAs semiconductor 2DEGs is typically tens of microns. In ballistic wires, where wire length and width are both much

smaller than L_{m}, electrons are not scattered inside the wire and conductance becomes quantized [34, 35] as discussed below.

2.1.3 Quantized conductance

When the wire length L is much shorter than the mean free path L_{m} in a quantum wire, conductance of the wire becomes quantized. This property is usually robust for a short wire, called a ballistic quantum point contact (QPC). Fig.2.3 shows the quantized conductance of a QPC in units of $\frac{2e^2}{h}$ [35].

In conductance measurement, a vanishingly small bias voltage δV is applied across the wire, and all the occupied subbands contribute to the net current:

$$I = \sum_{E_n \leq E_{\mathrm{F}}} I_n \cdot T_n = \sum_{E_n \leq E_{\mathrm{F}}} D_n(E_{\mathrm{F}}) e v_n(E_{\mathrm{F}}) e \cdot \delta V \cdot T_n \ , \tag{2.6}$$

where E_{F} is the Fermi energy, T_n is the transmission probability of each subband and $v_n = \sqrt{\frac{2(E_{\mathrm{F}}-E_n)}{m^*}}$ is the Fermi velocity of each subband. T_n ($E_n \leq E_{\mathrm{F}}$) is equal to 1 for a ballistic QPC. Thus the conductance is given by

$$G = \frac{I}{\delta V} = N g_s \frac{e^2}{h} = \frac{2e^2}{h} N \ , \tag{2.7}$$

where N is the number of subbands below E_{F}. Eq. 2.7 indicates that conductance for each subband is quantized in units of $\frac{2e^2}{h}$. In the experiment shown in Fig.2.3, the number of occupied subbands N decrease as the negative gate bias increase, resulting in the conductance step as a function of the gate voltage. This remarkable feature happens since energy dependent terms of devotion to conductance from each subband is canceled out in one dimensional system.

2.1.4 Tunnel-coupled quantum wire

A tunnel-coupled wire is a system, where two parallel quantum wires are coupled through a tunnel-barrier. In this subsection how an electron-state evolves in this system is described. For simplicity only a single conducting mode for each part of the wire is considered. A pseudo spin $|\uparrow\rangle$ ($|\downarrow\rangle$) is defined by a state, where an electron exists in an upper (a lower) part of the wire. Using these pseudo spins, we can write down Hamiltonian of the system as

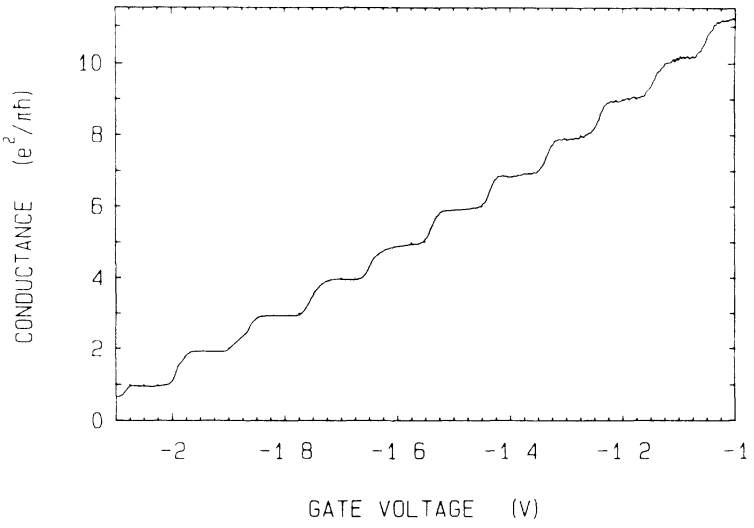

Fig. 2.3 Quantized conductance of a quantum point contact as a function of the split-gate voltage (cited from reference [34]).

follows:

$$H = H_K + H_T \tag{2.8}$$

$$H_K = \sum_k \varepsilon_k |k\rangle \langle k| \tag{2.9}$$

$$\langle x|k\rangle = \mathrm{e}^{ikx},\ \varepsilon_k = \frac{\hbar^2 k^2}{2m^*} \tag{2.10}$$

$$H_T = \varepsilon_\uparrow |\uparrow\rangle \langle\uparrow| + \varepsilon_\downarrow |\downarrow\rangle \langle\downarrow| - \tau(|\downarrow\rangle \langle\uparrow| + |\uparrow\rangle \langle\downarrow|)\ , \tag{2.11}$$

where m^* is effective mass of an electron, $\varepsilon_{\uparrow(\downarrow)}$ is confinement potential of the upper (lower) part of the wire and τ is tunnel-coupling energy between two parts of the wire.

When symmetric confinement potential ($\varepsilon_\uparrow = \varepsilon_\downarrow = \varepsilon_0$) is assumed, eigenstates in the system become symmetric ($|\psi_\mathrm{S}\rangle = \frac{|\uparrow\rangle + |\downarrow\rangle}{\sqrt{2}}$) and anti-symmetric ($|\psi_\mathrm{AS}\rangle = \frac{|\uparrow\rangle - |\downarrow\rangle}{\sqrt{2}}$) hybridized states of $|\uparrow\rangle$ and $|\downarrow\rangle$ as shown in Fig. 2.4. Eigen energies of H_T for these states are $E_\mathrm{S} = \varepsilon_0 - \tau$ and $E_\mathrm{AS} = \varepsilon_0 + \tau$, respectively. In a 2DEG system with low energy excitation only electrons at the Fermi surface contribute to transport and hence only state evolution of such electrons is taken into account. Using k_S, k_A, which satisfy the relation $E_\mathrm{S} + \frac{\hbar^2 k_\mathrm{S}^2}{2m^*} = E_\mathrm{A} + \frac{\hbar^2 k_\mathrm{A}^2}{2m^*} = E_\mathrm{F}$, an electron-state in a tunnel-coupled wire $|\psi_\mathrm{T}\rangle$ can be expressed by

$$|\psi_\mathrm{T}\rangle = \alpha |k_\mathrm{S}\rangle |\psi_\mathrm{S}\rangle + \beta |k_\mathrm{AS}\rangle |\psi_\mathrm{AS}\rangle\ . \tag{2.12}$$

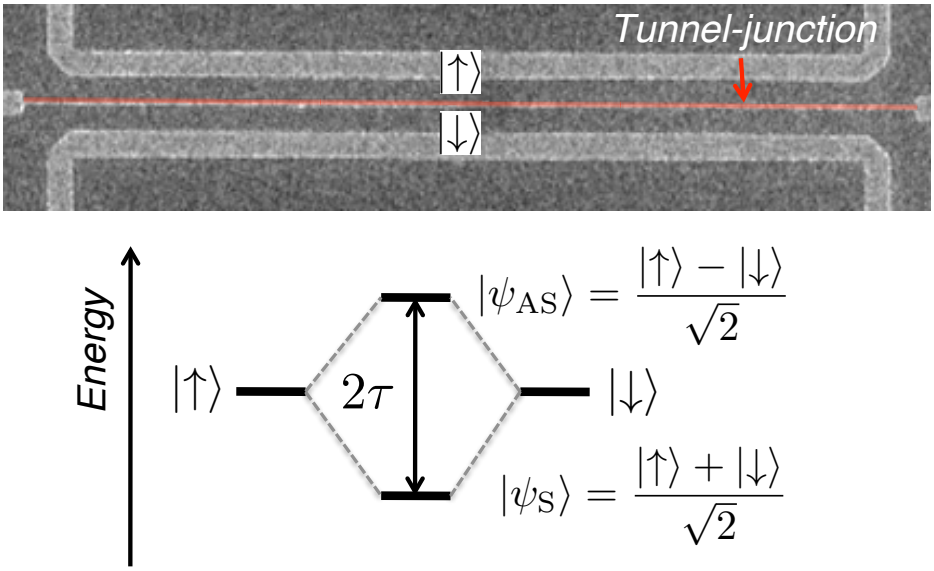

Fig. 2.4 A SEM picture of a tunnel-coupled wire in a GaAs/AlGaAs 2DEG system and an energy diagram of the system. A state, where an electron exists in an upper (a lower) part of the wire is defined as $|\uparrow\rangle$ ($|\downarrow\rangle$).

Then the state evolution from the initial state at the entrance ($x = 0$) to the final state at the exit ($x = L$) of a tunnel-coupled wire is considered. At $x = 0$ an electron-state is

$$\begin{aligned} |\psi_{\mathrm{T}}(x=0)\rangle &= \alpha \langle 0|k_{\mathrm{S}}\rangle |\psi_{\mathrm{S}}\rangle + \beta \langle 0|k_{\mathrm{AS}}\rangle |\psi_{\mathrm{AS}}\rangle \\ &= \alpha |\psi_{\mathrm{S}}\rangle + \beta |\psi_{\mathrm{AS}}\rangle \ . \end{aligned} \tag{2.13}$$

At $x = L$ an electron-state is

$$\begin{aligned} |\psi_{\mathrm{T}}(x=L)\rangle &= \alpha \langle L|k_{\mathrm{S}}\rangle |\psi_{\mathrm{S}}\rangle + \beta \langle L|k_{\mathrm{AS}}\rangle |\psi_{\mathrm{AS}}\rangle \\ &= \alpha e^{ik_{\mathrm{S}}L} |\psi_{\mathrm{S}}\rangle + \beta e^{ik_{\mathrm{A}}L} |\psi_{\mathrm{A}}\rangle \\ &= \frac{\alpha e^{ik_{\mathrm{S}}L} + \beta e^{ik_{\mathrm{A}}L}}{\sqrt{2}} |\uparrow\rangle + \frac{\alpha e^{ik_{\mathrm{S}}L} - \beta e^{ik_{\mathrm{A}}L}}{\sqrt{2}} |\downarrow\rangle \ . \end{aligned} \tag{2.14}$$

When an initial state is $|\uparrow\rangle$, $\alpha = \frac{1}{\sqrt{2}}$ and $\beta = \frac{1}{\sqrt{2}}$. As a result,

$$\begin{aligned} |\psi_{\mathrm{T}}(x=L)\rangle &= \frac{e^{ik_{\mathrm{S}}L} + e^{ik_{\mathrm{A}}L}}{\sqrt{2}} |\uparrow\rangle + \frac{e^{ik_{\mathrm{S}}L} - e^{ik_{\mathrm{A}}L}}{\sqrt{2}} |\downarrow\rangle \\ &= \sqrt{2} e^{i\frac{k_{\mathrm{S}}+k_{\mathrm{A}}}{2}L} \left[\cos(\frac{k_{\mathrm{S}} - k_{\mathrm{A}}}{2} L) |\uparrow\rangle + i \sin(\frac{k_{\mathrm{S}} - k_{\mathrm{A}}}{2} L) |\downarrow\rangle \right] \ . \end{aligned} \tag{2.15}$$

For an initial state of $|\downarrow\rangle$, $\alpha = \frac{1}{\sqrt{2}}$ and $\beta = -\frac{1}{\sqrt{2}}$. As a result,

$$\begin{aligned} |\psi_{\mathrm{T}}(x=L)\rangle &= \frac{e^{ik_{\mathrm{S}}L} - e^{ik_{\mathrm{A}}L}}{\sqrt{2}} |\uparrow\rangle + \frac{e^{ik_{\mathrm{S}}L} + e^{ik_{\mathrm{A}}L}}{\sqrt{2}} |\downarrow\rangle \\ &= \sqrt{2} e^{i\frac{k_{\mathrm{S}}+k_{\mathrm{A}}}{2}L} \left[i \sin(\frac{k_{\mathrm{S}} - k_{\mathrm{A}}}{2} L) |\uparrow\rangle + \cos(\frac{k_{\mathrm{S}} - k_{\mathrm{A}}}{2} L) |\downarrow\rangle \right] . \end{aligned} \tag{2.16}$$

From these results, operation of a tunnel-coupled wire of length L can be rewritten in the form as follows,

$$U_{\mathrm{T}}(\theta) = \cos\left(\frac{\theta}{2}\right) [\, |\uparrow\rangle\langle\uparrow| + |\downarrow\rangle\langle\downarrow| \,] + i \sin\left(\frac{\theta}{2}\right) [\, |\uparrow\rangle\langle\downarrow| + |\downarrow\rangle\langle\uparrow| \,] , \tag{2.17}$$

where $\theta = (k_{\mathrm{S}} - k_{\mathrm{A}})L$.

For the initial state $|\uparrow\rangle$ probabilities of finding the electron at $x = L$ in the upper and the lower contact are

$$|\langle\uparrow|\psi_f\rangle|^2 = \frac{1+\cos\theta}{2} \tag{2.18}$$

$$|\langle\downarrow|\psi_f\rangle|^2 = \frac{1-\cos\theta}{2} . \tag{2.19}$$

Since L is a fixed parameter in this structure, output currents oscillate between the upper and the lower contacts as functions of $(k_{\mathrm{S}} - k_{\mathrm{AS}})$, which can be controlled by τ through the voltage on the thin tunnel-coupling gate.

2.2 Coherent electron transport

2.2.1 Landauer Büttiker formula

In a classical electric circuit, electron transport is diffusive and is described by Ohm's law and Kirchhoff's law. However coherent transport in mesoscopic systems has no dissipation and cannot be described in the same way but by Landauer Büttiker formula [6]. Here we introduce Landauer Büttiker formula [36, 37].

We consider a multi-terminal device as shown in Fig. 2.5. The terminal p is connected to a contact, whose electrochemical potential is $\mu_p = eV_p$. As shown in section 2.1.3, conductance of a quantum wire can be written by $G = N\frac{2e^2}{h}$, where N is the number of occupied subbands in a quantum wire. Therefore when we define the total transmission $\bar{T}_{qp}$ from the terminal p to q as sum of the transmission probability of all subbands, the current J_p flow

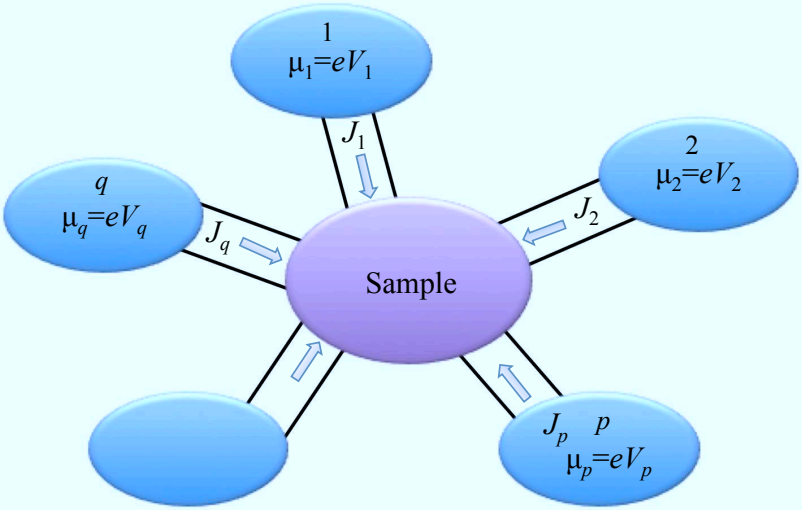

Fig. 2.5 Model for introducing Landauer Büttiker formula

into the sample from the terminal p is

$$J_p = \frac{2e^2}{h}\sum_q [\bar{T}_{qp}\frac{\mu_p}{e} - \bar{T}_{pq}\frac{\mu_q}{e}] \,. \tag{2.20}$$

We define $G_{pq} \equiv \frac{2e^2}{h}\bar{T}_{pq}$ and rewrite Eq. 2.20 as

$$J_p = \sum_q [G_{qp}V_p - G_{pq}V_q] \,. \tag{2.21}$$

This gives the general expression of the current.

There are some restrictions for currents and conductance coefficients. From the current conservation, current J_p must satisfy

$$\sum_q J_q = 0 \,. \tag{2.22}$$

When the potential V_p of all the contacts are equal, the current should be zero:

$$\sum_q [G_{qp} - G_{pq}] = 0 \,. \tag{2.23}$$

This is the so called gauge invariance and allows us to rewrite Eq. 2.21 in an equivalent form

$$J_p = \sum_q G_{pq}[V_p - V_q] \,. \tag{2.24}$$

Finally conductance coefficients (G) also obey the relation

$$G_{qp}(B) = G_{pq}(-B) \ . \tag{2.25}$$

Eq. 2.25 is Onsager's reciprocity law [38–40] and satisfied in the linear response regime regardless of the nature of the transport.

Landauer Büttiker formula gives a general expression for describing transport.

2.2.2 Aharonov-Bohm effect

In classical electrodynamics, the vector potential was introduced as a convenient mathematical aid for calculating the field and does not play a role by itself. In the quantum mechanics, however, the vector potential cannot be ignored and does play a role, which adds the extra phase to a particle traveling through electromagnetic environment [41]. This phase is called Aharonov-Bohm (AB) phase and can cause quantum interference [42, 43]. In the following the mechanism of the AB effect is briefly explained.

Hamiltonian of an electron inside electromagnetic environment H and a wave function ψ satisfying it are expressed by

$$H = \frac{(\boldsymbol{p}+e\boldsymbol{A})^2}{2m} + V(\boldsymbol{r}) \tag{2.26}$$

$$i\hbar\frac{\partial\psi}{\partial t} = H\psi \ , \tag{2.27}$$

where e is an elemental charge, $\boldsymbol{A}$ is the vector potential and $V(\boldsymbol{r})$ is the other potential energy. Here when we perform gauge transformation $\boldsymbol{A} = \boldsymbol{A}^{'} + \nabla\chi$, Hamiltonian becomes

$$H^{'} = \frac{(\boldsymbol{p}+e\boldsymbol{A}^{'})^2}{2m} + V(\boldsymbol{r}) \tag{2.28}$$

and a wave function becomes

$$\psi^{'} = \psi e^{i\frac{e}{\hbar}\chi}. \tag{2.29}$$

Then when $\nabla\chi$ is set to $\boldsymbol{A}$, $\boldsymbol{A}^{'}$ becomes $\boldsymbol{0}$. Therefore $H^{'}$ corresponds to H_0, which is Hamiltonian without magnetic field, and $\psi^{'}$ becomes ψ_0 ($i\hbar\frac{\partial\psi_0}{\partial t} = H_0\psi_0$). Hence

$$\psi = \psi_0 e^{-i\frac{e}{\hbar}\int\boldsymbol{A}\cdot d\boldsymbol{r}} \tag{2.30}$$

is obtained. As a result an electron traveling through the electromagnetic environment ac-

quires the AB phase $e^{-i\frac{e}{\hbar}\int \boldsymbol{A}\cdot d\boldsymbol{r}}$, which is called AB effect.

2.2.3 Quantum interference in mesoscopic systems

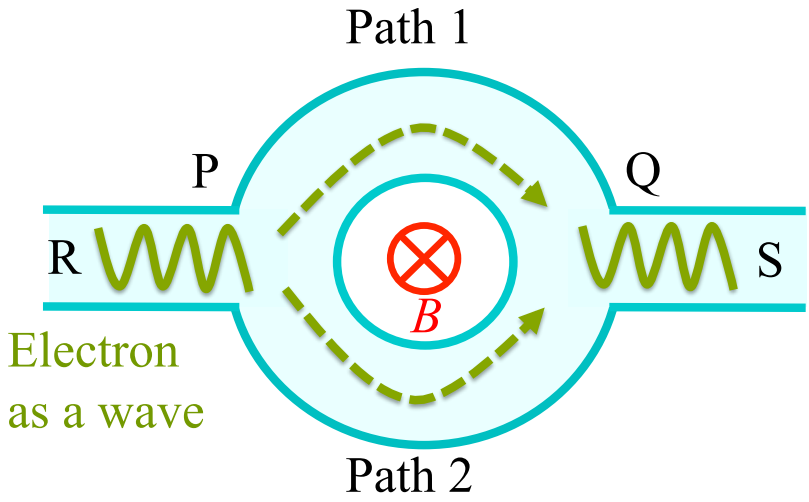

Fig. 2.6 An Aharonov-Bohm(AB) ring penetrated by the magnetic flux B and an electron as a wave. The electron wave becomes superposition of two paths in the ring and those waves interfere at the exit of the ring.

Observation of quantum interference is a powerful tool to measure quantum phase or phase relaxation length of electrons. In mesoscopic systems,it is observed that a conductance of a small ring structure oscillates as a function of the magnetic flux enclosed by the ring, which is usually referred to as AB oscillation since it originates from the AB phase. This oscillation can be understood as interference of waves traversing two arms of the ring (Fig. 2.6). When the waves are considered as plane waves, the wave in path 1 (path 2) becomes $\psi_1 = \exp\left[-i\int_{\text{path1}}(\boldsymbol{k}-\frac{e}{\hbar}\boldsymbol{A})\cdot d\boldsymbol{l}\right]$ ($\psi_2 = \exp\left[-i\int_{\text{path2}}(\boldsymbol{k}-\frac{e}{\hbar}\boldsymbol{A})\cdot d\boldsymbol{l}\right]$). In this case the wave function at the exit Q of the ring becomes $\psi_1+\psi_2$. As a result, the probability

amplitude at Q becomes

$$\begin{aligned}
|\psi_1+\psi_2|^2 &= \left|\exp\left[-i\int_{\text{path1}}(\boldsymbol{k}-\frac{e}{\hbar}\boldsymbol{A})\cdot \mathrm{d}\boldsymbol{l}\right]+\exp\left[-i\int_{\text{path2}}(\boldsymbol{k}-\frac{e}{\hbar}\boldsymbol{A})\cdot \mathrm{d}\boldsymbol{l}\right]\right|^2 \\
&= 2+2\cos\left[\oint \boldsymbol{k}\cdot \mathrm{d}\boldsymbol{l}-\frac{e}{\hbar}\oint \boldsymbol{A}\cdot \mathrm{d}\boldsymbol{l}\right] \\
&= 2+2\cos\left[\oint \boldsymbol{k}\cdot \mathrm{d}\boldsymbol{l}-\frac{e}{\hbar}\oint B\mathrm{d}S\right] \\
&= 2+2\cos\left[\oint \boldsymbol{k}\cdot \mathrm{d}\boldsymbol{l}-\frac{e}{\hbar}BS\right] \\
&= 2+2\cos\left[\oint \boldsymbol{k}\cdot \mathrm{d}\boldsymbol{l}-2\pi\frac{\Phi}{\Phi_0}\right] , \qquad (2.31)
\end{aligned}$$

where $\oint \boldsymbol{k}\cdot \mathrm{d}\boldsymbol{l}$ is the geometrical phase, $\Phi = BS$ is the magnetic flux enclosed by the two paths and $\Phi_0 = \frac{e}{h}$ is a flux quantum.

In reality, the interference is not so simple because the electron going through one path can be scattered to the other path depending on the nature of the *beam splitter* at P and Q. Such paths enclose the ring many times and generate higher order oscillations, whose oscillation period corresponds to $\frac{h}{e}$ divided by integer N. However the higher order oscillations are more difficult to observe since it is more difficult to maintain the phase coherence in a longer path. The $\frac{h}{Ne}$ oscillation involves a length NL (L: length of one arm), therefore its amplitude reduces by a factor of $\exp(-\frac{2NL}{L_\phi})$, where L_ϕ is a phase relaxation length of a sample.

2.2.4 Phase rigidity

In subsection 2.2.1 we describe Landauer Büttiker formula and some restrictions in coherent transport between contacts. When the restrictions (Eq. 2.23, 2.25) are applied to a two-terminal AB ring structure in Fig. 2.6, we get relations below.

$$\begin{aligned}
G_{\text{RS}}(B) &= G_{\text{SR}}(B) \\
G_{\text{RS}}(B) &= G_{\text{SR}}(-B)
\end{aligned}$$

When these relations are combined, we get a boundary condition

$$G_{\text{RS}}(B) = G_{\text{RS}}(-B) \ . \qquad (2.32)$$

Eq. 2.32 shows that two-terminal conductance always has to be an even function of the magnetic field. This restriction for a two-terminal devices is called *phase rigidity*.

The argument of the phase rigidity was presented by Levy Yeyati and Büttiker [14] to explain the experimental results by Yacoby [8]. Since the conductance through the two-terminal AB ring has to be an even function of B, G can be expanded in a Fourier series

$$G(B) = G_0 + G_1 \cos(BS + \delta_1) + \dots , \tag{2.33}$$

where S is the area enclosed by the two electron paths and the dots indicate the higher harmonics. Combining expansion Eq. 2.33 with symmetry Eq. 2.32, one finds that the phase δ_1 can only be either 0 or π.

2.2.5 Source of decoherence

Quantum coherence of an electron is lost when it interacts with other degrees of freedom such as electrons, phonons and electromagnetic field. Average length through which electrons can coherently propagate is called phase relaxation length l_ϕ and corresponding average time is called phase relaxation time τ_ϕ. l_ϕ is determined by various scattering processes, for example electron scattering, phonon scattering and spin scattering by magnetic impurities. When we define average time interval of such various inelastic scattering processes as τ_i, Matthiessen-rule can be applied for the simplest approximation.

$$\frac{1}{\tau_\phi} = \sum_i \frac{1}{\tau_i} \tag{2.34}$$

Another source of decoherence is thermal smearing of the Fermi surface. In electric transport measurements, we measure flux of electrons whose energies are in the vicinities of the Fermi surface. In subsection 2.2.3, we assume that all electrons have the same wave vector, but which is not the case in general. An observed interference pattern generally results from interferences of many electrons with slightly different wave vectors. When interference patterns of each electron are too different, we loose a interference pattern. This phase randomization by difference of wave vectors of electrons becomes larger when electrons propagate through a longer path. In diffusive transport, the length in which electrons loose their coherence is called thermal diffusion length l_{th} and is expressed:

$$l_{th} = \sqrt{D\tau_{th}} = \sqrt{\frac{hD}{k_\mathrm{B}T}} , \tag{2.35}$$

where $\tau_{th} = \frac{h}{k_B T}$ is time in which electrons loose their phase coherence by thermal smearing and D is a diffusion constant [37]. In ballistic transport, the length is called thermal length and is expressed:

$$l_{th} = v_F \tau_{th} = \frac{h v_F}{k_B T} \tag{2.36}$$

l_{th} can be determined with high accuracy since D and v_F are relatively easy to estimate and other parameters are universal constant. On the other hand, l_ϕ has to be determined by quantum interference phenomena and it is more difficult to estimate it with high accuracy.

2.2.6 Phase relaxation length in ballistic conductors

In diffusive one-dimensional (1D) and 2D conductors, the phase relaxation length at low temperatures has been studied intensively, both theoretically and experimentally [44, 45]. Quantum interference phenomena such as weak localization and universal conductance fluctuations (UCFs) are used as powerful tools to study phase coherence in diffusive systems.

On the other hand, there are less studies for clean electronic systems because weak localization and UCFs cannot be used. However recently several experimental and theoretical works for ballistic conductors using the AB effect have been reported [46–49]. Hansen *et al.* [46] experimentally studied the temperature dependence of AB oscillation amplitude in a ballistic AB ring and measured a decoherence rate linear in temperature, which indicates the phase relaxation length inversely proportional to the temperature $l_\phi \propto T^{-1}$. Around the same period, Seelig *et al.* [48] theoretically explained a linear dependence of decoherence rate in a AB ring formed by metallic gates, where fluctuation of charge induced by capacitive coupling between the 2DEG and the metallic gates is considered as a decoherence source.

Later Kobayashi *et al.* [47] investigated the measurement-configuration dependence of the decoherence rate in a AB ring with four terminals where two terminals served as current probes and the other two terminals were used as voltage probes. They found a strong dependence of the decoherence rate on the probe configuration. Seelig *et al.* [49] explained such configuration dependence by considering voltage fluctuation in the measurement circuit. According to their theory, when average injectivities from the leads to two different arms of the AB ring are equal, effects of voltage fluctuation are cancelled out and the decoherence is suppressed.

2.3 Quantum dot

A quantum dot (QD) is a small droplet of electrons, where strong confinement from three dimensions quantize orbital energy levels. Furthermore charging energy originating from strong Coulomb interaction between electrons inside a QD lifts degeneracy of orbital and spin degree of freedom. As a result energy levels inside a QD is completely quantized, which allows to control the number of electrons inside a QD in a unit of single electron. There are QDs of many different sizes and materials: for instance, InAs self-assembled QDs [50], and vertically [51] or laterally [52] defined QDs in GaAs 2DEG systems. They were shown to be rich test grounds for quantum mechanics [51, 53, 54] and recently also attract a lot of interests as a candidate of a system for quantum computation [21–23, 55].

Measurements of electron-transport across a QD is performed by attaching source and drain leads on both sides of a QD and energy levels are controlled by capacitively coupled gate voltages (Fig. 2.7). With this setup a characteristic behavior called *Coulomb oscillation*

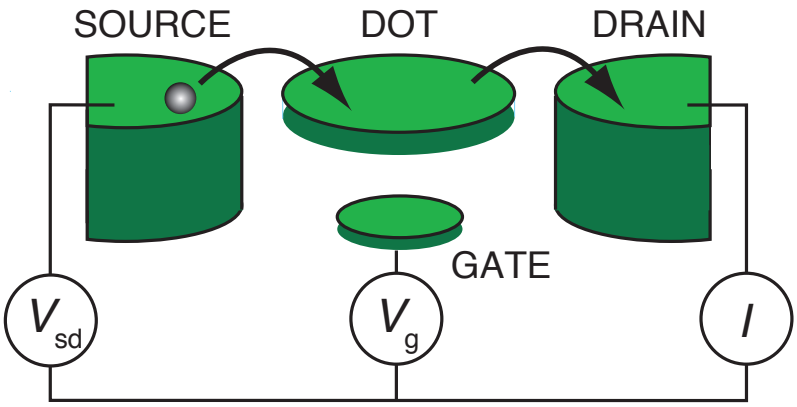

Fig. 2.7 Schematic picture of a QD with setup for transport measurement.

is observed. In the following we explain the Constant Interaction (CI) model [56, 57] to understand the Coulomb oscillation, which is the simplest way to describe main features of a QD. Then we consider resonant tunneling in the one-dimensional double barrier structure.

2.3.1 Constant interaction model

The CI model based on the two assumptions:

1. Coulomb interactions between electrons in the QD and those in the environment are parameterized by a single constant capacitance C.

2. The single-particle energy level spectrum of the QD is independent of these interactions.

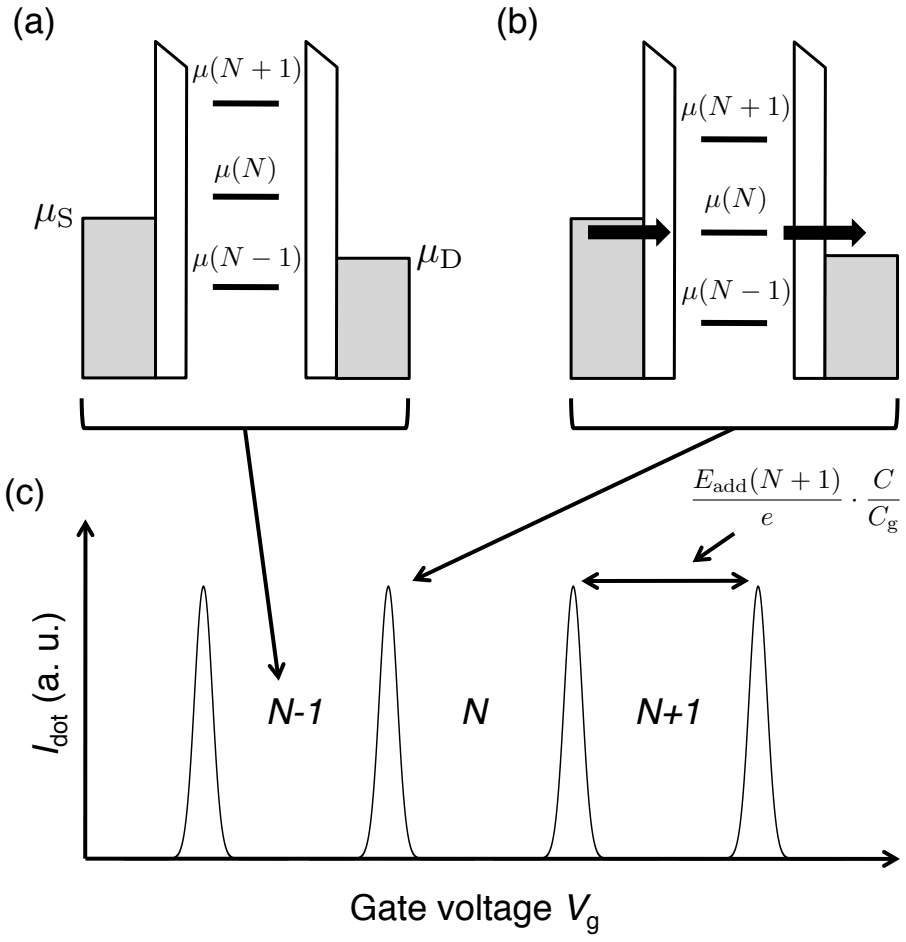

Fig. 2.8 Electrochemical potential ladders of a QD: (a) and (b) correspond to the Coulomb blockade and the Coulomb peak, respectively. (c) Coulomb oscillations as a function of the gate voltage $V_{\rm g}$.

Initially C is given by $C = C_{\rm S} + C_{\rm D} + C_{\rm g}$, where $C_{\rm S}$, $C_{\rm D}$ and $C_{\rm g}$ are the capacitance between the QD and the source, the drain and the gate to control the energy level of the QD. Total energy of the QD containing N electrons are then expressed by

$$U(N) = \sum_{p=1}^{N} E_p(B) + \frac{[-|e|(N-N_0) + C_{\rm S}V_{\rm S} + C_{\rm D}V_{\rm D} + C_{\rm g}V_{\rm g}]^2}{2C}\,, \tag{2.37}$$

where $-|e|$ is the elementary charge and N_0 is the charge in the QD compensating the positive background charge originating from the donors in the heterostructure. V_S, V_D and V_g are the voltage applied to the source, the drain and the gate. $E_p(B)$ is the p-th orbital energy level in the QD including spin degree of freedom at the external magnetic field B. The terms $C_S V_S$, $C_D V_D$ and $C_g V_g$ represent the charges induced by the capacitive coupling between the QD and the source, the drain and the gate. The electrochemical potential $\mu(N)$ of the QD is hence defined as

$$\mu(N) \equiv U(N) - U(N-1) \tag{2.38}$$

$$= \left(N - N_0 - \frac{1}{2}\right) E_C - \frac{E_C}{|e|}(C_S V_S + C_D V_D + C_g V_g) + E_N \,, \tag{2.39}$$

where $E_C = e^2/C$ is the charging energy.

When the electrochemical potential of the source and the drain is positioned in between the ones of the QD, tunneling of electrons through the QD is blocked, which is so called the *Coulomb blockade* (Fig. 2.8a). On the other hand when the electrochemical potential of the QD is positioned in between the one of the source and the drain, the resonant tunneling (see section 2.3.2) occurs and electrons tunnel from the source to the drain through the QD (Fig. 2.8b). As a result, the current oscillations are observed as a function of the V_g by changing the electrochemical potential, which is the *Coulomb oscillation* (Fig. 2.8c). The distance between Coulomb peaks for the gate voltage ΔV_g is given by

$$|e|\Delta V_g(N) \cdot \frac{C_g}{C} = E_{add}(N) \tag{2.40}$$

$$E_{add}(N) \equiv \mu(N+1) - \mu(N) = E_C + \Delta E(N) \tag{2.41}$$

$$\Delta V_g(N) = \frac{E_{add}(N)}{|e|} \cdot \frac{C}{C_g} \,, \tag{2.42}$$

where $E_{add}(N)$ is so called addition energy and $\Delta E(N) = E_{N+1} - E_N$ is the energy difference between N-th and $(N+1)$-th orbital energy levels. ΔE becomes 0 when N-th and $(N+1)$-th orbital energy levels are spin degenerated orbitals.

In the discussion above we only consider the ground state of the QD, which is appropriate at the low bias regime ($|e(V_S - V_D)| \ll \Delta E,\ E_C$). However at high bias regime ($|e(V_S - V_D)| \geq \Delta E$) not only the ground state but also the excited state contribute to the transport, which allows excitation spectroscopy. Fig. 2.9a shows the transport at $\mu_S > \mu(N) + \Delta E(N) > \mu(N) > \mu_D$, where both the ground state and the first excited state are inside the bias window and hence the conductance across the QD depends on tunnel-coupling

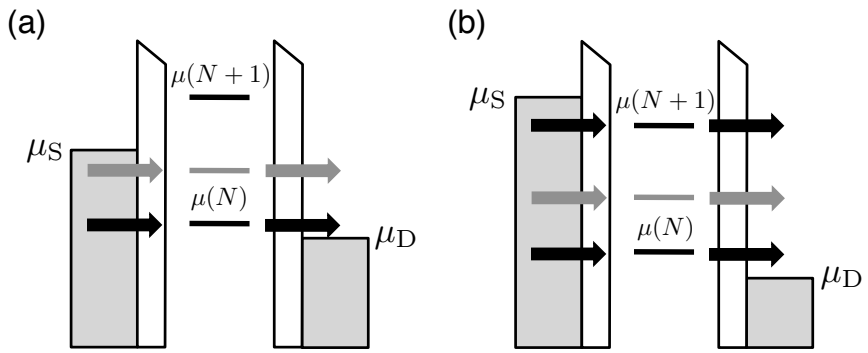

Fig. 2.9 Electron transport at high bias regime. (a) ($\mu_S > \mu(N) + \Delta E(N) > \mu(N) > \mu_D$), (b) ($\mu_S > \mu(N+1) > \mu(N) + \Delta E(N) > \mu(N) > \mu_D$).

of the both states. For the even larger source-drain bias as shown in Fig. 2.9b, the ground state of the $(N+1)$-th electron contributes to the transport, where the number of electrons inside the QD fluctuates between $(N-1) \leftrightarrow N \leftrightarrow (N+1)$.

Finally we describe the excitation spectroscopy called a *Coulomb diamond*. It is a powerful tool to examine the energy scale of the QD. Fig. 2.10a shows the energy diagram of

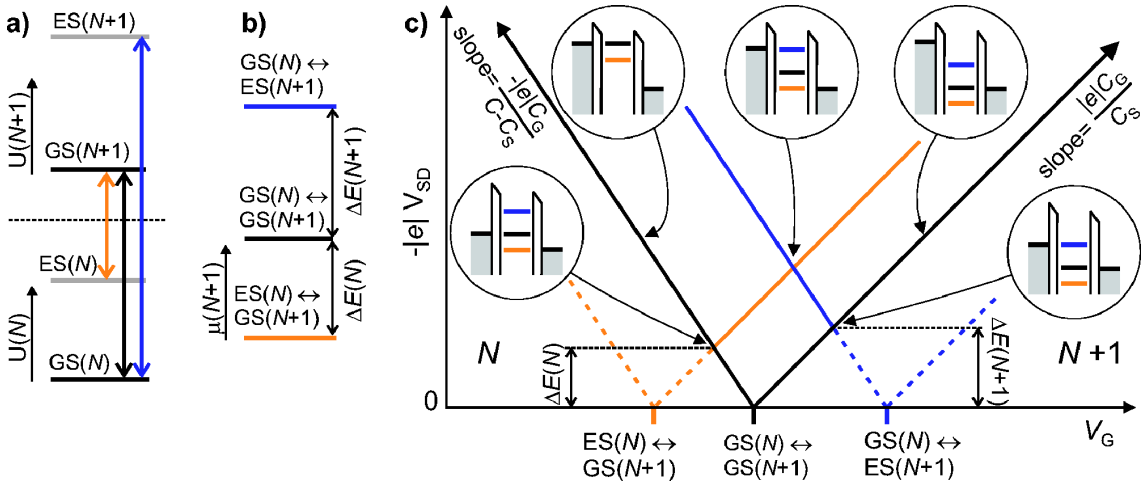

Fig. 2.10 (a)Energy diagram of the N and $N+1$-th ground and the first excited state. (b) Electrochemical potential of the transition appeared in (a). (c) Coulomb diamond of a QD: map of non-zero differential conductance (dI_{dot}/dV_{sd}) in the plane of $-|e|V_{sd} = -|e|(V_S - V_D)$ and V_g. (cited from ref. [57])

the ground and the first excited state of N and $N+1$ electron-state. The electrochemical potential appeared in Fig. 2.10a is shown in Fig. 2.10b. Fig. 2.10c illustrates the typical

feature of a Coulomb diamond, where differential conductance $\frac{dI_{dot}}{dV_{sd}}$ is mapped in a plane of a source-drain voltage $V_{sd} = (V_S - V_D)$ and gate voltage V_g. Along the zero source-drain bias three electrochemical potentials shown in Fig. 2.10b are pointed. Two lines are originated from those points, where the differential conductance becomes finite. Left (right) going lines are the condition, where the electrochemical potential is aligned with the one of the source (the drain). Below the black solid line the number of electrons in the QD is fixed to N for the left side and $N+1$ for the right side. This region is called *Coulomb blockade* region. The lines related to N $(N+1)$-electron excited state is interrupted at the boundary of the N $(N+1)$-electron Coulomb blockade region since inside the blockade region the N $(N+1)$-electron ground state is occupied and hence N $(N+1)$-electron excited state is not available. From the Coulomb diamond it is possible to find the energy level spacing $\Delta E(N)$ as shown in Fig. 2.10c.

2.3.2 Resonant tunneling in one-dimensional double barrier structure

When the electrochemical potential of a QD is positioned in between that of the source and the drain, resonant tunneling occurs and an electron tunnels from the source to the drain through the QD. In this section we consider the resonant tunneling utilizing an one-dimensional double barrier structure (Fig. 2.11). Suppose a plane wave of wave vector k is

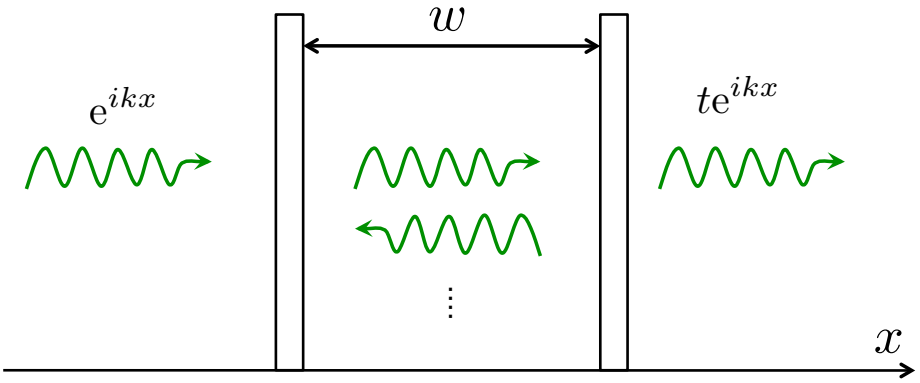

Fig. 2.11 One dimensional double barrier structure.

injected to the structure, transmission coefficient t is considered. Here scattering matrix of the left (right) barrier is defined by

$$S_{1(2)} = \begin{pmatrix} r_{1(2)} & t'_{1(2)} \\ t_{1(2)} & r'_{1(2)} \end{pmatrix} . \tag{2.43}$$

The transmission coefficient t becomes

$$\begin{aligned} t &= t_1 e^{ikw} t_2 [1 + r_2 e^{i2kw} r_1^{'} + (r_2 e^{i2kw} r_1^{'})^2 + ...] \\ &= \frac{t_1 e^{ikw} t_2}{1 - r_2 e^{i2kw} r_1^{'}} \end{aligned} \tag{2.44}$$

The transmission probability $T = |t|^2$ hence becomes

$$\begin{aligned} T &= \frac{T_1 T_2}{1 + R_1^{'} R_2 - 2\sqrt{R_1^{'} R_2}\cos\theta} \\ &= \frac{T_1 T_2}{(1 - \sqrt{R_1^{'} R_2})^2 + 2\sqrt{R_1^{'} R_2}(1 - \cos\theta)} , \end{aligned} \tag{2.45}$$

where $T_{1(2)}^{(')} = |t_{1(2)}^{(')}|^2$, $R_{1(2)}^{(')} = |r_{1(2)}^{(')}|^2$, $r_1^{'} = \sqrt{R_1^{'}} e^{i\alpha_1}$, $r_2 = \sqrt{R_2} e^{i\alpha_2}$ and $\theta = (2kw + \alpha_1 + \alpha_2)$. We are considering the situation, where each tunnel-barrier is very high ($T_1^{(')}, T_2^{(')} \ll 1$). As a result T can be written in the form:

$$T \approx \frac{T_1 T_2}{(\frac{T_1^{'} + T_2}{2})^2 + 2(1 - \cos\theta)} . \tag{2.46}$$

From Eq. 2.46, T becomes non-zero only at the vicinity of $\theta(E_r) = 2n\pi$, so we expand $(1 - \cos\theta)$ at the vicinity of the resonant energy E_r and consider the leading order. Then we obtain

$$\begin{aligned} T(E_r) &\approx \frac{T_1 T_2}{(\frac{T_1^{'} + T_2}{2})^2 + \left(\frac{d\theta}{dE}\right)^2 (E - E_r)^2} \\ &= \frac{\Gamma_1 \Gamma_2}{(E - E_r)^2 + (\frac{\Gamma_1^{'} + \Gamma_2}{2})^2} , \end{aligned} \tag{2.47}$$

where $\Gamma_{1(2)}^{(')} \equiv \frac{dE}{d\theta} \cdot T_{1(2)}^{(')} \approx \hbar \cdot \frac{v}{2w} \cdot T_{1(2)}^{(')}$ is physically $\hbar$ times the rate at which an electron confined between two barriers would tunnel out through the barriers in to the left (right) lead. When we define $\Gamma = \Gamma_1^{'} + \Gamma_2$, T can be further deformed as follows:

$$T \approx \frac{\Gamma_1 \Gamma_2}{\Gamma} \cdot \frac{\Gamma}{(E - E_r)^2 + (\frac{\Gamma}{2})^2} . \tag{2.48}$$

The right hand part of this expression becomes Lorenzian function, so the transmission probability shows a Lorenzian line shape when passing through the resonance. This approximation is only valid around the resonance ($E \sim E_r$). Therefore at low bias and low

temperature ($\Gamma > k_{\mathrm{B}}T,\ V_{\mathrm{sd}}$), we observe a Coulomb peak of the Lorentzian line shape when scanning through the resonance by the gate voltage V_{g}.

2.4 The Kondo effect in a QD

The Kondo effect, a typical electron-correlation, arises from the interaction between a localized spin and surrounding conducting electrons [58]. It is characterized by a many-body singlet ground state, often refereed to as the Kondo cloud. It was first observed in metals with a small inclusion of magnetic impurities, manifests itself by the increase of the electrical resistance at low temperatures. On the other hand, the advance in nanotechnology has led to a revival of the Kondo effect, as it is now possible to study the interaction of a single impurity spin in contact with an electron reservoir, in particular in semiconductor quantum dots [59–61].

The Kondo effect originates from the interaction between the spin of a magnetic impurity S_i and conduction electron spin at the impurity site s_i and is described by so called $s-d$ Hamiltonian:

$$H_{sd} = -\frac{J}{2N_{\mathrm{A}}} \sum_{\boldsymbol{k}k'\sigma\sigma'} c^{\dagger}_{\boldsymbol{k}\sigma} \boldsymbol{\sigma}_{\sigma\sigma'} c_{\boldsymbol{k}'\sigma'} \cdot \boldsymbol{S}\,, \tag{2.49}$$

where J is the parameter characterizing the interaction, N_{A} is the total number of atom, $c^{(\dagger)}_{\boldsymbol{k}\sigma}$ is annihilation (creation) operator with the wave vector $\boldsymbol{k}$ and the spin $\sigma(=\uparrow,\downarrow)$, $\boldsymbol{\sigma}$ is Pauli matrices and $\boldsymbol{\sigma}_{\sigma\sigma'}$ is the element of it and $\boldsymbol{S}$ is the vector of spin operator for the impurity. This effective Hamiltonian can be derived from the Hamiltonian of the Anderson model, where the exchange term between a localized electron and conduction electrons is treated by perturbation up to the second order. When the scattering rate by this effective Hamiltonian is calculated using Born approximation up to the second order, logarithmic dependence of the resistance can be obtained. The ground state of the localized spin and the conduction electrons becomes a many-body singlet state usually referred to the Kondo singlet state, where the localized spin is screened by surrounded conduction electrons due to frequent scattering with spin flip. The corresponding resonant state appears at the Fermi surface below the characteristic temperature defined as the Kondo temperature T_{K}:

$$k_{\mathrm{B}}T_{\mathrm{K}} = D\exp\left(\frac{1}{JN(\varepsilon_{\mathrm{F}})}\right)\,, \tag{2.50}$$

where D corresponds to the band width of the conduction band and $N(\varepsilon_{\mathrm{F}})$ is the density of

state at the Fermi surface.

In a QD the number of electrons are fixed in the Coulomb blockade region. When the number of electrons is even and all the electrons form spin pairs, the total spin inside the QD becomes zero. On the other hand when the number of electrons is odd, the spin should be always left and it is considered as a localized spin. Therefore the Kondo effect occurs originating from the interaction between the conduction electrons in the source-drain leads and the localized spin inside the QD. As a result, the Kondo resonant state appears at the Fermi surface, through which electrons transport across the QD even in the Coulomb blockade region. Indeed in the experiments [59–61] the Kondo effect in a QD is observed with specific features listed below:

1. When lowering the temperature, the conductance increases in alternate Coulomb blockade valley. The conductance in the valley without the Kondo effect decreases with the temperature, whereas the one with the Kondo effect increases.

2. The above mentioned increase of the conductance has logarithmic dependence on temperature.

3. The Kondo state appears at the Fermi surface, which is on resonance at zero source-drain bias. Therefore the conductance decreases with increasing the source-drain bias, different from the usual case, which is called *zero bias anomaly*.

4. Since at strong magnetic field scattering with spin flip is suppressed, the Kondo effect seems to disappear. However it comes back by applying the source-drain bias to compensate the Zeeman energy. As a result, zero bias anomaly mentioned above splits by applying the magnetic field.

Though the Kondo effect is referred for various many-body phenomena, some of the above features, such as the alternative appearance of the Kondo effect and the zero bias anomaly in the energy spectroscopy, were first observed in QD systems owing to the various tunable parameters. On the other hand the alternative appearance of the Kondo effect depends on the confinement potential of the QD and is not always observed. It only appears when the total spin of the QD changes between 0 and $\frac{1}{2}$ according to the even and odd number of electron-occupation. In the QD other than the observations above, a variety of new Kondo related phenomena have been reported [62–64], which contains rich physics about electron-correlations.

2.5 Transmission phase across a quantum dot

2.5.1 Transmission phase across a Breit-Wigner resonance

As known from the Landauer-Büttiker formula, electron transport in mesoscopic systems is considered as a scattering problem, where scattering matrix is defined at each part of a circuit. Transmission probability is then calculated by using transmission coefficients, which are elements of the scattering matrix. Transmission phase across a QD is the phase term of the transmission coefficient of a QD ($t_{\mathrm{QD}} = |t_{\mathrm{QD}}|e^{i\alpha}$). From Eq. 2.44 the transmission coefficient across a QD at the low bias and the low temperature condition ($\Gamma > k_{\mathrm{B}}T$, V_{sd}) is expressed by

$$t_{\mathrm{QD}} = \frac{t_1 e^{ikw} t_2}{1 - r_2 e^{i2kw} r_1'} \ . \tag{2.51}$$

When we consider this coefficient around the resonance $|t_{\mathrm{QD}}|^2 \approx 1$, we can obtain approximated expression as follows:

$$t_{\mathrm{QD}}(E) = \frac{\sqrt{\Gamma_1 \Gamma_2} e^{i\beta}}{(E - E_r) + i\frac{\Gamma}{2}} \ , \tag{2.52}$$

where E_r is the energy at the resonance, $\Gamma = \Gamma_1' + \Gamma_2$, β is the constant phase term. From

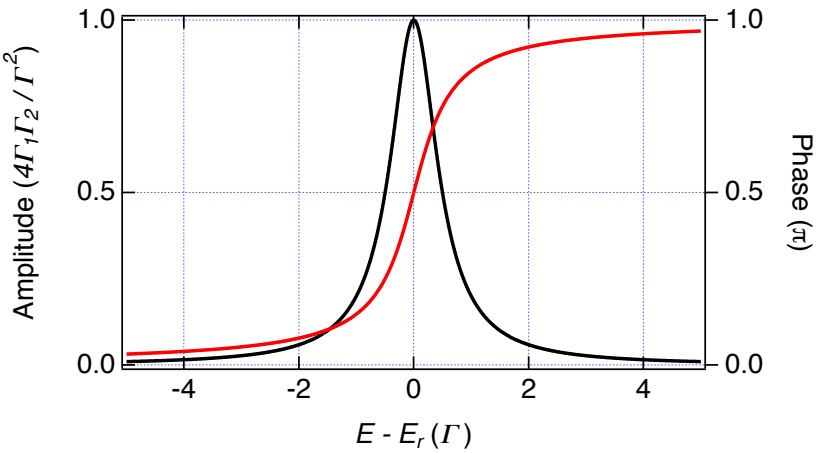

Fig. 2.12 Transmission amplitude $|t_{\mathrm{QD}}|^2$ (black curve and left axis) and transmission phase α (red curve and right axis) as a function of energy around the resonance calculated from Eq. 2.52, where the constant phase term β is set to 0.

this expression, the transmission phase across a QD changes by π through the resonance at

a Coulomb peak (CP), as shown in Fig. 2.12.

Here the phase shift across the resonance can be also understood in terms of Friedel's sum rule, which relates a change of the number of electrons inside a QD ΔN to transmission phase shift across the QD $\Delta\alpha$ as follows [14]:

$$\Delta\alpha = \pi \cdot \Delta N \ . \tag{2.53}$$

ΔN as a function of ΔV_{p} is given by the integrated area under the CP divided by the total area of the CP. Therefore the number of electrons inside the QD changes by 1 across the CP. The phase shift calculated from this ΔN and Eq. 2.53 is exactly the same and is shown in Fig. 2.12.

First experiment concerning such transmission phase shift across a QD was performed using the AB effect (section 2.2.2) [8], where, however, the observed phase was smeared by multi-path interferences as expected from the phase rigidity (section 2.2.4) in the two-terminal setup [11]. Two years later, in an experiment using a multi-terminal AB ring, π-phase shift expected from the Lorentzian type of the resonance was confirmed [3], where the phase rigidity was lifted by breaking the unitarity adding extra ohmic contacts inside the AB ring.

2.5.2 Phase lapse and universal behavior in many electron QDs

In the experiment of ref. [3] abrupt phase lapse (PL) between Coulomb peaks (CPs) was found, which occurred shorter energy scale than any other energy scale related to the QD such as tunnel-coupling energy Γ and temperature $k_{\mathrm{B}}T$. It is theoretically proposed that the PL can be understood by using the generalized Friedel's sum rule [32]. When orbital parity relation between CPs is the same, a singular point called *transmission zero* appears and the PL occurs at the point. On the other hand when it is different, there is no singular point between CPs and smooth phase evolution should be observed.

Another important findings in the experiment [3] is that a PL appears at all valleys between the CPs, which means that the orbital parity of all the CPs is the same. This observation contradicts with the naive expectation that there are both valleys with and without PLs. Such phase behavior with and without PLs were reported later from the same group in a few electron QD, which contains less than 10 electrons, using a similar multi-terminal AB ring [4]. However also in this experiment when increasing the number of electron inside the QD to more than 14, PLs in all successive Coulomb blockade valleys were recovered. This continuous PL behavior for large QDs containing many electrons observed in the multi-terminal

AB ring is called *universal* PL problem since it is robust irrespective of QD parameters.

To explain the universal PL, several mechanisms such as the existence of strong coupling state [65–67], elastic co-tunneling with finite Coulomb interaction at finite temperature [68, 69] and a chaotic QD within the constant interaction model [70] were proposed. Regardless of such intensive theoretical works, the mechanism of the universal behavior is still controversial. The problem is that there have only been a few experiments on this matter. Further experimental works are therefore needed for better understanding of the phase behavior of many electron QDs.

2.5.3 Transmission phase across a QD with the Kondo correlation

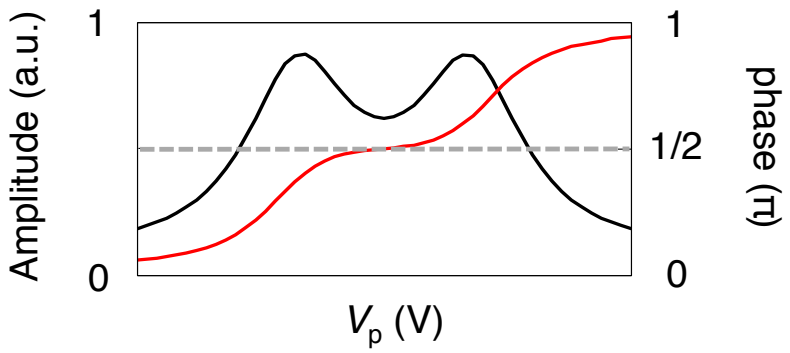

Fig. 2.13 Transmission amplitude (black line, left axis) and phase (red line, right axis) in the Kondo regime (cited from NRG calculations performed by Arne Alex). It is calculated by using an 1-level Anderson model [15]. The parameters used here are $\Gamma/U = 0.2$, $T/U = 0.003$.

As explained in section 2.5.1, transmission phase changes by π across a CP and it can be understood in terms of Friedel's sum rule. However across two CPs with the Kondo correlation in the valley between them, which we call the Kondo valley, the phase behavior is altered. At temperature lower than the Kondo temperature $T \lesssim T_K$ the Kondo singlet state is formed at the Fermi energy in the Kondo valley. From the Noziéres' Fermi liquid theory [1] an electron scattered through the Kondo singlet state acquires $\pi/2$-phase shift without a spin flip.

Across the first CP the phase shifts by $\pi/2$ during the formation of the Kondo singlet state. In the valley an electron is scattered through the Kondo singlet state and hence the phase shift stays at $\pi/2$. Then across the second CP the phase again evolves by $\pi/2$ as shown in Fig. 2.13 [2]. Observation of the $\pi/2$-phase shift in the Kondo valley provides an evidence of the Kondo singlet state.

2.6 Electron transport by surface acoustic wave

Electron pumping by a surface acoustic wave (SAW) through a depleted quantum wire was thought as a promising candidate for determining the value of the elementary charge. If that value is determined with enough precision, Quantum metrological triangle is closed and the units of practical measurement systems can be defined by true invariants of nature. Hence it has been intensively studied for the past 20 years in the view point of field of quantum metrology. Recently it has also become of considerable interest as a technique for coherent transport of electrons [71]. In this section, we explain how to generate a SAW and transport electrons.

2.6.1 Generation of surface acoustic wave by IDT

A SAW is a wave propagating on a surface of an elastic body. More than 90% of its energy is concentrated on the depth shorter than its wave length due to exponential decay along depth direction. Thus it is possible to generate, detect and reflect SAWs on the substrate surface. In our experiment, we use Interdigital transducer (IDT) to generate SAWs. Fig. 2.14 shows the schematic picture of generation of SAWs. When we apply RF voltages on the IDT deposited on a piezoelectric substrate, SAWs are generated due to the piezoelectric effect. When the wave length of SAWs corresponds to the distance of IDT electrodes d, SAWs generated by each electrode of the IDT are on resonance and strong SAWs propagate along the surface. In contrast, when the wave length does not correspond to d, each wave destructively interfere and SAWs are not generated.

Here the wave length of SAWs is determined by frequency of RF voltages and sound velocity of the piezoelectric substrate. In our experiment, we used a GaAs/AlGaAs 2DEG system. Since GaAs is a piezoelectric material, it is possible to generate SAWs by applying RF voltages on a IDT evaporated on the surface. A crystal orientation of the surface in our GaAs substrate is (001), where SAWs propagate along the crystal axis [110]. Accordingly the sound velocity near the surface is about 2862 m/s [72]. A relation between the wave length of a SAW and RF frequency is $f = 2862/\lambda$ [Hz]. When the distance of the IDT electrodes is 1μm ($d = 1\mu$m), the resonant frequency should be

$$f_0 \sim \frac{2862\ [\mathrm{m/s}]}{1\times 10^{-6}\ [\mathrm{m}]} = 2.862\ \ [\mathrm{GHz}]. \tag{2.54}$$

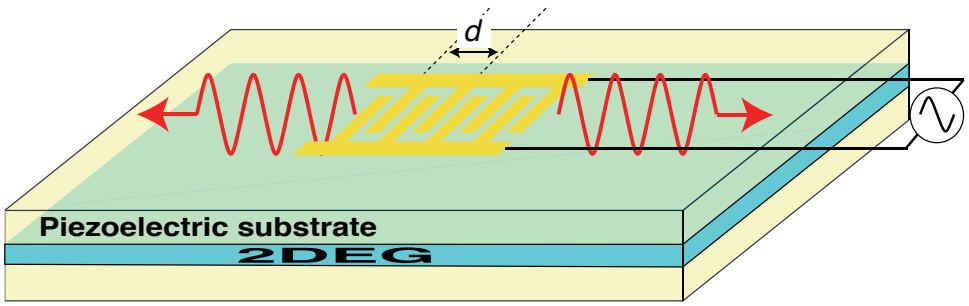

Fig. 2.14 Generation of SAWs. A pair of comb-shaped metallic electrodes on piezoelectric substrate is called an interdigital transducer (IDT). d shows distance between electrodes in a comb-shaped electrode. When resonant RF voltages are applied to the IDT, SAWs propagating both directions are generated due to piezoelectric effect.

2.6.2 Electron pumping by a surface acoustic wave

When SAWs are applied to a 2DEG wafer, the potential wave generated by SAWs is basically screened by electrons. However when SAWs propagate through a depleted region of the 2DEG, they effectively modulate the potential profile. Indeed when SAWs are applied to a depleted quantum wire, electrons are picked up from the 2DEG and transferred across the wire as follows.

Fig. 2.15a shows the potential profile around a depleted quantum wire when SAWs are applied. The dark region is the area where electrons exist. Inside the quantum wire, electrons are transported by moving QDs formed by the potential of SAWs and the quantum wire. FIg. 2.15b is a plot of potential energy along the center of the quantum wire in Fig. 2.15a. Since the wire is depleted without SAWs, the potential inside the wire exceeds the Fermi energy E_{F}. Confinement of the moving QDs can be controlled by amplitude of SAWs and electrostatic gate voltages of the quantum wire. When the amplitude of SAWs is strong enough to transfer electrons over the potential slop and the separation of the quantized energy levels of the moving QDs is large enough, the number of electrons inside each QD is quantized to an integer number. As a result, the observed current becomes $I = nef$ [74, 75], where n is the number of electrons inside each QD, e is an elementary charge and f is a frequency of SAWs.

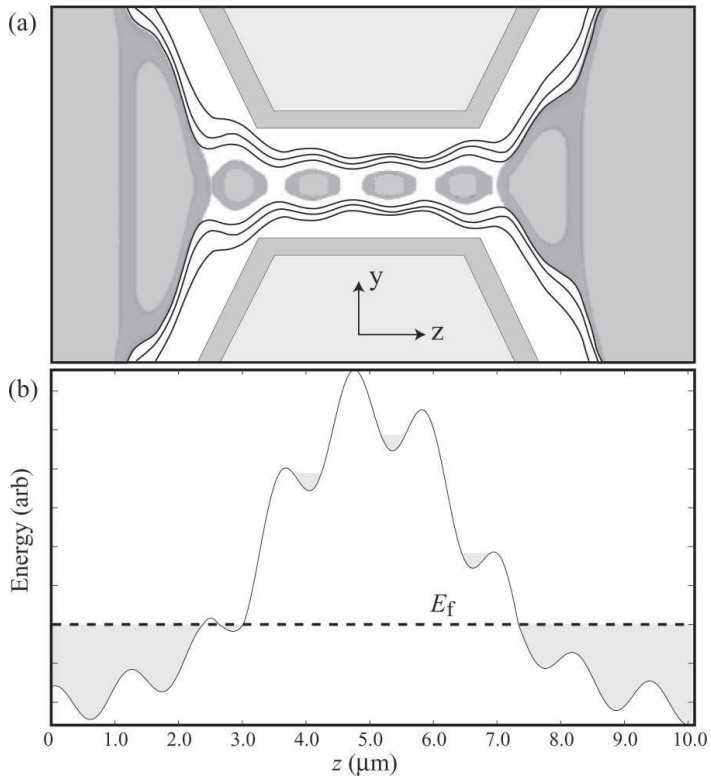

Fig. 2.15 Formation of moving QDs in a depleted quantum wire (cited from ref. [73]). (a) A schematic picture of potential contours around a depleted quantum wire when SAWs are applied. (b) A schematic picture of potential energy along the center of the quantum wire in (a). The dark region is the area where electrons exist in both (a) and (b).

Chapter 3

Realization of a *true* two-path interferometer

3.1 Introduction

A two-path interferometer is a strong tool to measure the transmission phase of an electron, which is not readily apparent from standard conductance measurements. When a QD is inserted into one of the two paths of the interferometer, it is possible to detect the transmission phase shift of electrons passing through the QD from measurement of the interference pattern of the conductance. However realization of a *true* two-path interferometer is not a simple task since in mesoscopic systems linear conductance is bound to a contact geometry as discussed in the section 2.2.1. For example a conventional two-terminal AB interferometer, which could be considered as a two-path interferometer, suffers from the phase rigidity problem (subsection 2.2.4), in which the interference becomes a complicated multi-path interference. Realization of a *true* two-path interferometer requires a novel approach. Multi-terminal AB ring structures [3, 9] have been employed to avoid the phase rigidity problem and to realize a two-path interferometer. In these preceding experiments lifting of phase rigidity was confirmed by the fact that the conductance was not an even function of the magnetic field. However even if the phase rigidity is lifted, it is difficult to confirm whether contributions from multi-path interferences are fully suppressed or not. Here we employed an AB ring with tunnel-coupled wires to realize a *true* two-path interferometer [76]. In the following the device structure and the measurement setup are presented. Then we describe in detail how the device works.

3.2 Device and measurement

The device was fabricated in a 2DEG ($n \approx 1.9 \times 10^{11}$ cm^{-2}, $\mu \approx 2 \times 10^{6}$ cm^{2}/Vs, depth $= 125$ nm) formed at an AlGaAs/GaAs hetero-interface with a standard Schottky gate technique (Fig. 3.1). The AB ring at the center is connected to the leads at both ends through

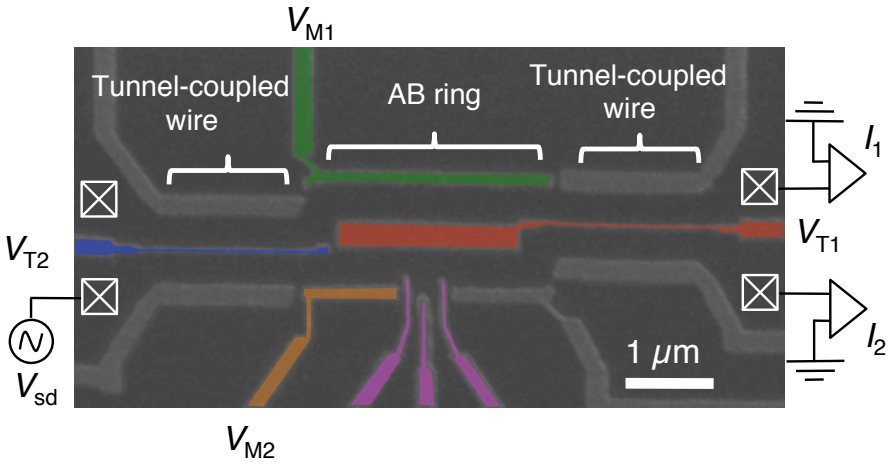

Fig. 3.1 Scanning electron micrograph (SEM) picture of the device and measurement setup.

two parallel quantum channels coupled via a tunnel-barrier. The gate voltage V_{T1} is used to form the AB ring and to control the tunnel-coupling between the two wires of the right tunnel-coupled wire whereas the gate voltage V_{T2} is used only to control the tunnel-coupling of the left tunnel-coupled wire. The gate voltages V_{M1} and V_{M2} allow to modulate the wave vector of an electron traversing through the upper and lower path of the AB ring, respectively. The three gates colored in pink are prepared to form a QD. However in the experiment discussed in this section we did not use the QD but just applied the voltage on the center gate out of three to form a quantum channel. For transport measurements we applied a source-drain voltage on the lower or upper left contact and measured currents flowing through the upper and lower right contacts, I_1 and I_2, using a standard lock-in technique ($V_{sd} = 50\ \mu$V, $f = 23.3$ Hz). The measurements presented in this chapter were performed at 70 mK.

Fig. 3.2 shows the electrical circuit for the measurement. Each line is electrically filtered by a copper powder filter and a two stage RC-filter at base temperature.

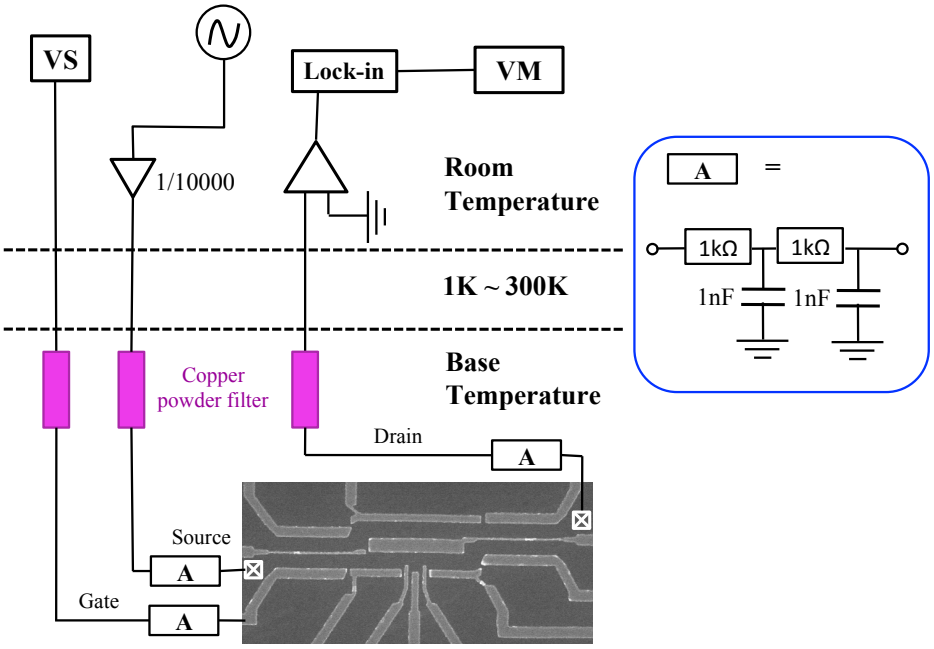

Fig. 3.2 Electrical circuit for measurement.

3.3 Quantum interference in two different regimes

We describe distinct interference features of the output currents observed in two different regimes in this section. For this measurement we applied zero voltage ($V_{T2} = 0$V) on the center gate of the left tunnel-coupled wire and floated the upper-left ohmic contact. Then the device has effectively three terminals having the AB ring connected to the left lead through a single quantum wire and to the right lead through a tunnel-coupled wire. In the first regime, which we call a Strong Coupling Regime (SCR), only small negative voltage V_{T1} was applied to the center gate of the right tunnel-coupled wire, so that the 2DEG underneath the AB ring was fully depleted but the center tunnel-coupling of the right lead was still strong. In this case the right tunnel-coupled wire behaves as a single quantum wire as well. On the other hand in the second regime, which we call the Weak Coupling Regime (WCR), we made V_{T1} more negative than in the SCR such that a tunnel-coupled wire was formed in the right lead. In these two regimes we observed quantum interferences as a function of the magnetic field and the gate voltage V_{M1}.

Fig. 3.3 shows raw currents I_1 and I_2 in the SCR (a) and the WCR (b) as a function of magnetic field applied perpendicularly to the surface of the device. Oscillations originating from the AB phase (Section 2.2.2, 2.2.3) were clearly observed in both regimes. Visibility of the oscillations defined by the oscillation amplitude divided by the mean value is about

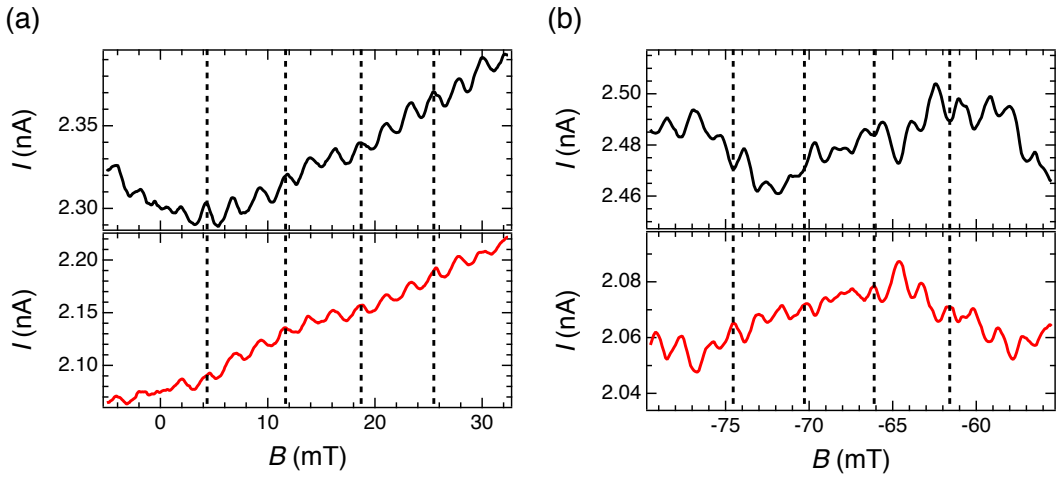

Fig. 3.3 Quantum interferences as a function of magnetic field in the SCR (a) and the WCR (b). The black (red) curve in both (a) and (b) is the current observed at I_1 (I_2).

~ 0.3 %. To see the interference features more clearly, we extracted the oscillating part of the currents. Here we used two different methods since the observed interference contains different contributions between the SCR and the WCR as we will see later. The first is to subtract a smooth background current from the raw data, which can be regarded as a high pass filter. The other is a band pass filter using a fast Fourier transform (FFT), where the oscillating part is extracted by performing a complex FFT to filter out the noise outside the peak region, followed by an inverse complex FFT. For the SCR we used a high pass filter since not only a main frequency component but also a higher harmonics is expected to appear in the signal. For the WCR we expected the signal only around a single frequency and hence we used a band pass filter for analysis.

Fig. 3.4 shows the oscillating part of the currents in the two regimes. In the SCR (Fig. 3.4a) two output currents I_1 and I_2 oscillate in phase. This in-phase oscillation indicates oscillation of the total conductance through the AB ring, and therefore suggests that a standing wave is generated inside the AB ring by interferences of electrons encircling the AB ring multiple times and the total conductance oscillates depending on whether the interference at the exit of the AB ring is either constructive or destructive as depicted in Fig. 3.5a. On the other hand in the WCR (Fig. 3.4b) the two output currents oscillate with anti-phase. These anti-phase oscillations reflect the fact that the total conductance through the AB ring is almost independent of the magnetic field, and therefore means that there is no standing wave inside the AB ring due to the absence of interferences of electrons encircling the AB ring multiple times. The anti-phase oscillations also indicate that the electron state is formed

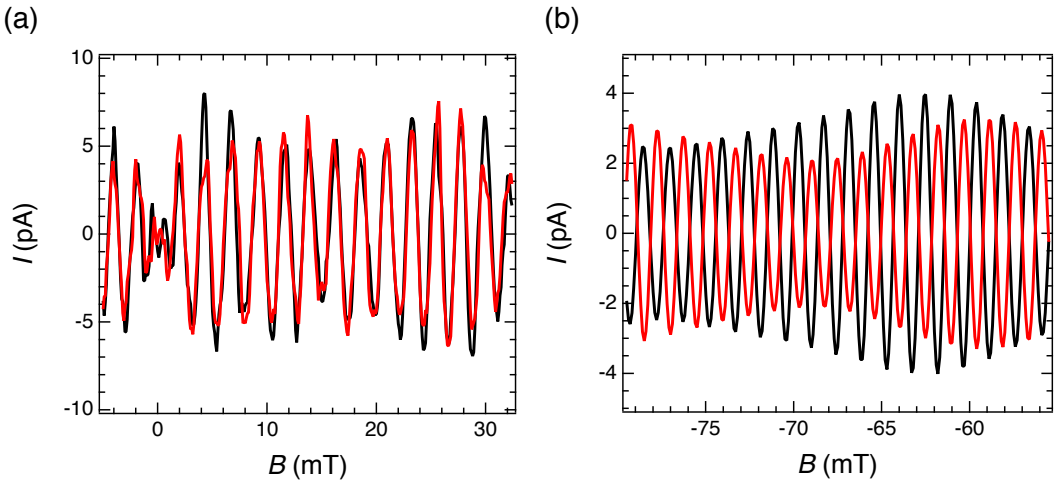

Fig. 3.4 Oscillating parts of quantum interferences as a function of magnetic field in the SCR (a) and WCR (b). The black (red) curve in both (a) and (b) is the current observed at I_1 (I_2).

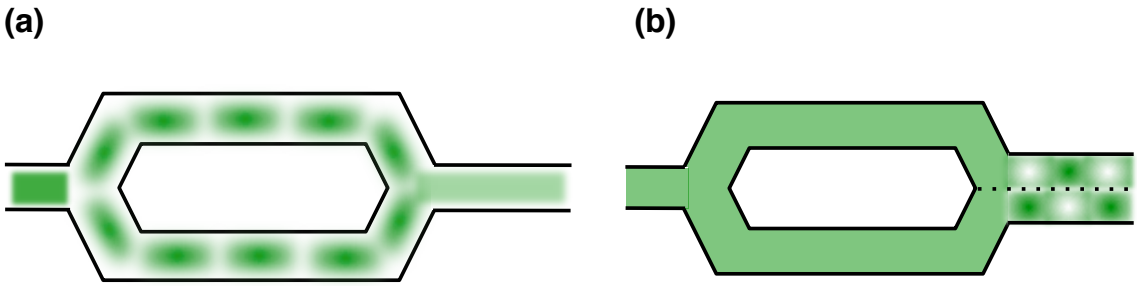

Fig. 3.5 Schematic image of probability density of electrons in the SCR (a) and the WCR (b).

by superposition of symmetric and anti-symmetric states of the upper and lower part of the coupled-wire, which leads to the oscillation of an electron between the two parts. As a result, coherent electrons, which contribute to the anti-phase oscillation, follow the two direct trajectories without encircling the AB ring and oscillate between the upper and lower part in the tunnel-coupled wire as shown in Fig. 3.5. We therefore consider anti-phase oscillations with equal amplitude as such *true* two-path interferences. However the observed oscillation amplitude in Fig. 3.4b is different in a certain range of the magnetic field. A possible reason is that the series conductance to the right leads is different between the upper and the lower path, which depends on the magnetic field probably because the magnetic field affects the connection of the electron wave function.

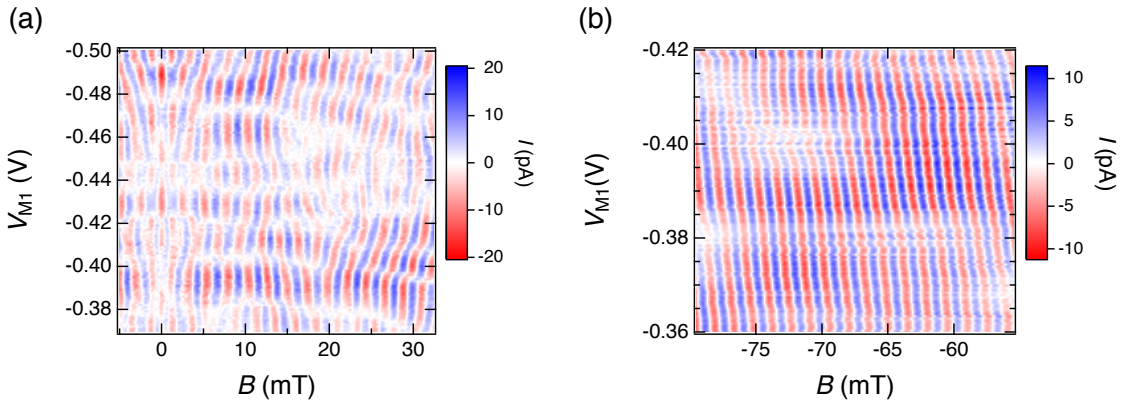

Fig. 3.6 Modulation of the geometrical phase in two regimes. For the SCR (a) and the WCR (b), oscillations of the current as a function of magnetic field are plotted for different gate voltage of V_{M1} along the vertical axis. About the SCR we plotted the oscillation of sum of the currents $I_1 + I_2$ to extract only in-phase components, whereas for the *new* regime we plotted the difference between the currents $I_1 - I_2$ to extract only anti-phase components.

Next we tried to modulate the geometrical phase by linearly modulating the wave vector of electrons with gate voltage V_{M1} in the two regimes (Fig. 3.6). In Fig. 3.6 AB oscillations along the lateral axis is plotted for various voltages of V_{M1} along the vertical axis. In the SCR (Fig. 3.6a) the phase of the AB oscillations jumps at some V_{M1} along the vertical axis. At the zero magnetic filed the phase of the AB oscillation is fixed to either 0 or π and the oscillation pattern is symmetric about zero magnetic field. This is a typical feature of the phase rigidity (section 2.2.4) for a multi-channel AB ring. We therefore see in the SCR that the interferometer effectively becomes a typical two-terminal interferometer bound to the phase rigidity, consistent with the setup where the AB ring is connected to the leads through

single quantum wires at the both sides. On the other hand in the WCR the phase of the AB oscillation smoothly shifts with V_{M1} as expected for a direct two-path interference (Eq. 2.31 in section 2.2.3). This result also supports that the observed anti-phase oscillations in the WCR are *true* two-path interferences.

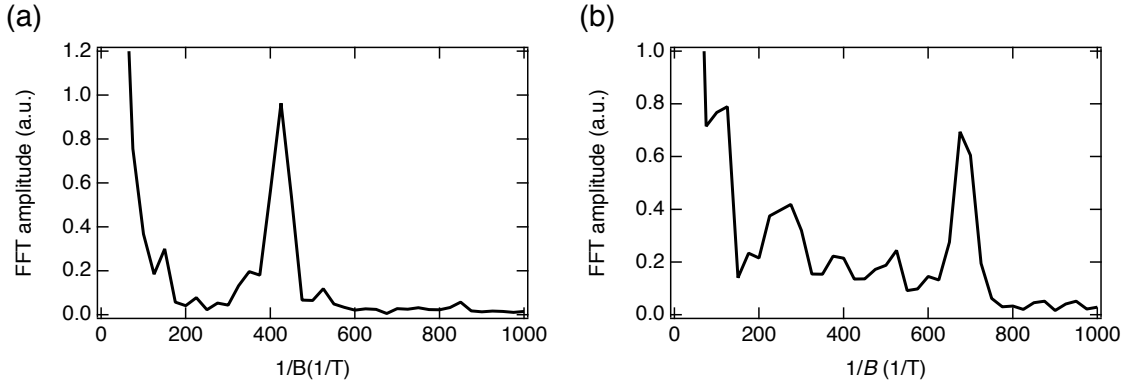

Fig. 3.7 FFT amplitude of AB oscillations. For the SCR an oscillating part of $I_1 + I_2$ is analyzed by a complex FFT, whereas for the WCR an oscillating part of $I_1 - I_2$ is analyzed to obtain FFT amplitude as a function of the reciprocal of the magnetic field. The large signal at around zero shows dc components of currents.

Finally we refer to the difference of the area enclosed by an electron in the interferometer, which appears in the different periods of the AB oscillations. Fig. 3.7 shows the FFT spectrum of sum of the currents, $I_1 + I_2$, for the SCR (a) and difference between the currents, $I_1 - I_2$, for the WCR (b). The peak position in frequency is much higher in the WCR. This peak position is proportional to the area enclosed by an electron in the interferometer. Therefore Fig. 3.7 implies that an electron encloses a much larger area in the WCR. In the WCR a more negative gate voltage of $V_{T1} = -600$ mV was applied to form a tunnel-coupled wire at the right side than $V_{T1} = -300$ mV in the SCR. This difference of V_{T1} leads to a difference of the depleted area of the center island in the AB ring. However it does not explain such a large difference (SCR: ~ 425 [1/T], WCR: ~ 680 [1/T]) observed here. When we assume that an electron encloses the AB ring passing through the center of the quantum wire defined by the metallic gate pattern, we expect the peak position of ~ 455 [1/T]. In this device the width of the quantum wire in the AB ring is about 375 nm. When we form the quantum wire in GaAs/AlGaAs 2DEG systems using Schottky gates, the depleted region underneath the metallic gate typically expands from the edge of the metal by the length scale comparable with the depth of 2DEG. The depth of 2DEG in this device is 125 nm and hence the actual confinement of the quantum wire is expected to be narrower than 125 nm.

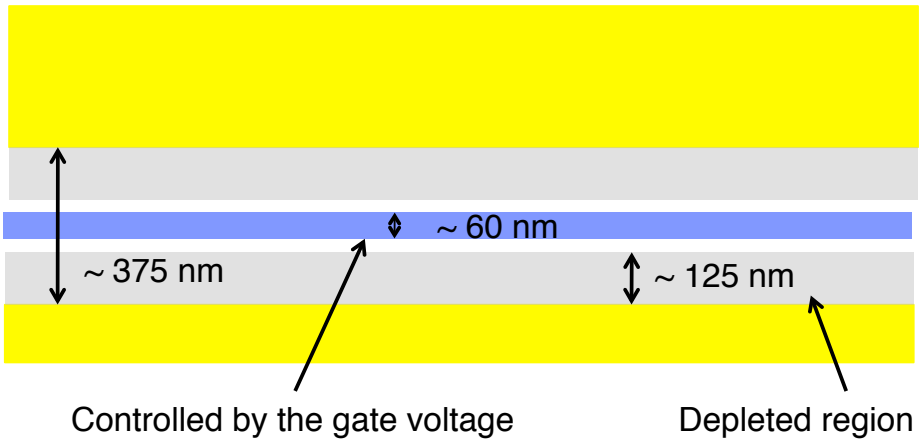

Fig. 3.8 Schematic image of the discussion about the area enclosed by electron trajectories.

Assuming that the center of the electron wave function can be controlled within half of the actual confinement width by the gate voltage (blue region in Fig. 3.8), the peak position can be modulated in the range of $390 \sim 520$ $[1/\mathrm{T}]$. The peak position of the SCR is within the range. However the peak at ~ 680 $[1/\mathrm{T}]$ for the WCR is out of this range, which implies that an electron also acquires the AB phase in the tunnel-coupled wire region.

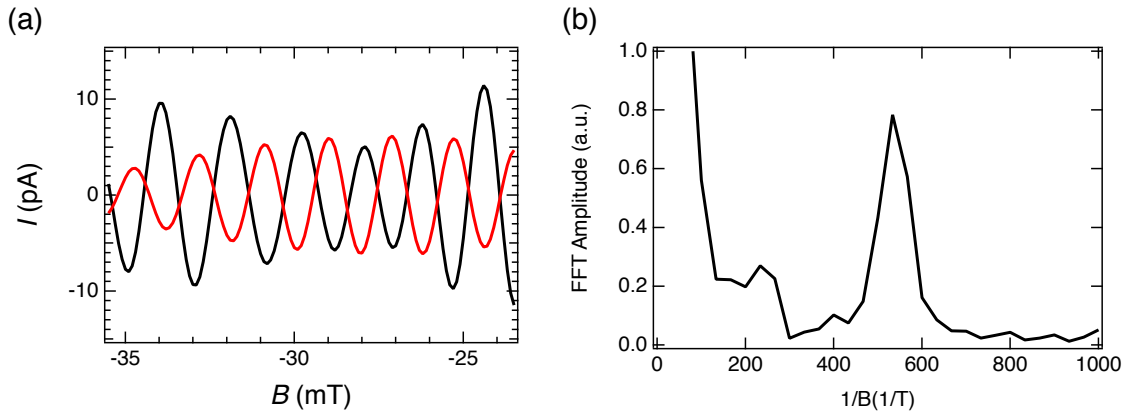

Fig. 3.9 Oscillating parts (a) and FFT amplitude (b) of the anti-phase oscillation in the WCR observed at a different gate voltage condition of the right tunnel-coupled wire from the data shown in Figs. 3.3b, 3.4b, 3.6b and 3.7b.

There is another experimental evidence that in the WCR an electron also acquires AB phase in the tunnel-coupled wire region. When we fixed V_{T1} and the gate voltages to form the AB ring and only made the voltages on the upper and lower gate to form the right tunnel-coupled wire more negative, we observed anti-phase oscillations with an FFT peak

at a smaller value of $1/B$ $(= 533)$ as shown in Fig. 3.9. The difference of the peak position between Fig. 3.7b and Fig. 3.9b originates from the different gate voltage configuration of the right tunnel-coupled wire. This suggests that an electron acquires the AB phase in the tunnel-coupled wire region.

3.4 Transition between two different regimes

In this section we discuss why distinct interferences appear in the two different regimes. Of importance is the wave function matching in the transition region between the AB ring and the tunnel-coupled wire. In a tunnel-coupled wire the eigenstates are the symmetric and anti-symmetric hybridized states of the upper and lower part of the wire as discussed in section 2.1.4. When the confinement energy of the two wires are the same ($\varepsilon_\uparrow = \varepsilon_\downarrow = \varepsilon_0$), the eigen energy is $E_{\mathrm{S(AS)}} = \varepsilon_0 - (+)\tau$, where τ is tunnel-coupling energy.

In the SCR V_{T1} is made slightly negative to deplete the region underneath the thicker part of the gate to form the AB ring but still keep the tunnel-coupling strong such that the tunnel-coupled wire behaves as a single quantum wire. Furthermore to observe nice in-phase oscillations as shown in Fig. 3.4a, we also applied more negative voltages to the side gates of the tunnel-coupled wire to make the wire narrower. As a result the width of the effective single quantum wire becomes close to the one of the AB ring. In such a situation the energy spacing between the transmitting modes of the effectively single quantum wire is quite large, so that the lower (higher) mode is adiabatically connected with the lower (higher) mode at the exit of the AB ring. Since the AB ring is connected to the two output contacts through a single quantum wire and each mode of the wire is adiabatically connected to that in the ring, i.e. with neither scattering nor interference between different modes of the wire, we naturally expect in-phase behavior for the two output currents I_1 and I_2 as expected for an interferometer with ideal single channel wires.

In the following, we consider the evolution of the electron-state at the transition region between the AB ring and the tunnel-coupled wire using pseudo spins $|\uparrow\rangle$, $|\downarrow\rangle$ and a wave function of the propagating direction $|k\rangle$ as defined in section 2.1.4. The final state of the AB ring at the transition region is expressed by $\frac{1}{\sqrt{2}}|k\rangle\left(|\uparrow\rangle + \mathrm{e}^{i\varphi}|\downarrow\rangle\right)$, where φ is the phase accumulated through the AB ring. Suppose that only the symmetric component is transmitted to the wire in the right side and the anti-symmetric one is reflected. The output currents are proportional to

$$\left|\langle k|k\rangle\left(\frac{\langle\uparrow| + \langle\downarrow|}{\sqrt{2}}\right)\cdot\left(\frac{|\uparrow\rangle + \mathrm{e}^{i\varphi}|\downarrow\rangle}{\sqrt{2}}\right)\right|^2 = \frac{1+\cos\varphi}{2} \tag{3.1}$$

and oscillate as a function of φ. In the discussion above we assumed that the interference is a *pure* two-path interference, which is not smeared by multi-path interferences. However in this two-terminal situation as discussed in section 2.2.4 actual interferences include complicated multi-path interferences to satisfy the boundary condition ($G(B) = G(-B)$). Therefore the correct understanding of the observed in-phase interferences should be as follows. A standing wave is formed inside the AB ring due to multi-path interferences such that the condition ($G(B) = G(-B)$) is satisfied. This standing wave is modified by applying the magnetic field and the output currents oscillate depending on whether the interference at the transition region is constructive or destructive as depicted in Fig. 3.5a. Nevertheless the important point is still that the tunnel-coupled wire behaves as a single quantum wire with large energy separation between the symmetric and anti-symmetric eigenstates so that the connection of the wave function at the transition region is adiabatic.

In the WCR the tunnel-coupling energy is smaller compared to that in the SCR due to existence of a tunnel-barrier and E_{S} and E_{AS} are close. Therefore both the symmetric and anti-symmetric hybridized states can be connected to a certain eigenstate in the AB ring, which allows to fully transfer an electron-state from the AB ring with a $\{|\uparrow\rangle, |\downarrow\rangle\}$ basis to a tunnel-coupled wire with a $\{|\psi_{\mathrm{S}}\rangle = \frac{|\uparrow\rangle+|\downarrow\rangle}{\sqrt{2}}, |\psi_{\mathrm{AS}}\rangle = \frac{|\uparrow\rangle-|\downarrow\rangle}{\sqrt{2}}\}$ basis. In this case when the confinement potential of each part of the wire at the transition region and that of each arm of the AB ring are well aligned, an electron is not backscattered to the other arm of the AB ring at the connection and oscillates between the two states because the typical length scale of the tunneling becomes larger than the length of the transition region. This results in anti-phase oscillation of the output currents I_1 and I_2 as shown in Fig. 3.4b and Fig. 3.9a. Since there is no backscattering and an electron-state fully transfers from the AB ring to the tunnel-coupled wire, the output currents which oscillate with anti-phase contain information about *true* two-path interference or phase information of the electron wave function (details are discussed in Chapter 4). Concerning the phase rigidity in the WCR the system becomes a three-terminal device, so the requirement of an even function of the magnetic field is not applied for each current of I_1 and I_2 but the sum of the currents $I_1 + I_2$. Indeed, anti-phase oscillation of I_1 and I_2 means that the total current $I_1 + I_2$ is independent of the magnetic field, which satisfies the boundary condition: $G(B) = G(-B)$.

3.5 AB phase accumulation in a tunnel-coupled wire

In section 3.3 we have put forward that in the WCR an electron acquires an AB phase not only in the AB ring but also in the tunnel-coupled wire. Here we discuss possible

mechanisms of the appearance of an AB phase in a tunnel-coupled wire.

Electron transport under low-energy excitation is basically assumed to be adiabatic, where an electron stays in its instantaneous eigenstates and the total energy is conserved during transport. When transport of an electron at the Fermi surface is considered, the electron state at the right exit of the AB ring can be expressed by $\frac{1}{\sqrt{2}}|k_0\rangle\left(|\uparrow\rangle+\mathrm{e}^{i\varphi}|\downarrow\rangle\right)$, where φ is the phase accumulated across the AB ring and sum of the confinement energy in y-direction and the kinetic energy in x-direction is equal to the Fermi energy ($\varepsilon_0+\frac{\hbar^2k_0^2}{2m^*}=E_\mathrm{F}$). Then when an electron enters the tunnel-coupled wire, the initial state becomes $\frac{1}{\sqrt{2}}[\frac{1+\mathrm{e}^{i\varphi}}{\sqrt{2}}|k_\mathrm{S}\rangle\frac{|\uparrow+\downarrow\rangle}{\sqrt{2}}+\frac{1-\mathrm{e}^{i\varphi}}{\sqrt{2}}|k_\mathrm{A}\rangle\frac{|\uparrow\rangle-|\downarrow\rangle}{\sqrt{2}}]=\frac{1}{2}[(1+\mathrm{e}^{i\varphi})|k_\mathrm{S}\rangle|\psi_\mathrm{S}\rangle+(1-\mathrm{e}^{i\varphi})|k_\mathrm{A}\rangle|\psi_\mathrm{A}\rangle]$ by adiabatic evolution, where $|\psi_\mathrm{S}\rangle=\frac{|\uparrow\rangle+|\downarrow\rangle}{\sqrt{2}}$, $|\psi_\mathrm{A}\rangle=\frac{|\uparrow\rangle-|\downarrow\rangle}{\sqrt{2}}$ are the eigenstates of y-direction in the tunnel-coupled wire and those energy satisfy $E_\mathrm{S}+\frac{\hbar^2k_\mathrm{S}^2}{2m^*}=E_\mathrm{F}$ and $E_\mathrm{A}+\frac{\hbar^2k_\mathrm{A}^2}{2m^*}=E_\mathrm{F}$. In this adiabatic case the electron-state is formed by a superposition of $|\psi_\mathrm{S}\rangle$ and $|\psi_\mathrm{A}\rangle$ and the phase accumulation through the AB ring is terminated immediately after the electron enters the tunnel-coupled wire, i.e. an electron does not acquire extra AB phase in the tunnel-coupled wire. This is also confirmed by a detailed analytical calculation using a ladder model [77]. To reproduce the large AB area with constant oscillation frequencies, we need to assume a potential offset between the two parts of the tunnel-coupled wire, in which case $|\psi_\mathrm{S}\rangle$ and $|\psi_\mathrm{A}\rangle$ approaches $|\uparrow\rangle$ and $|\downarrow\rangle$. However, this gives rise to a significant reduction of the oscillating amplitude, which is inconsistent with the experimental result.

The above discussion does not take into account for the two dimensionality of the tunnel-coupled wire. When we consider the Lorentz force, the center of the symmetric and anti-symmetric wave functions shifts to the opposite directions along y-direction due to the orthogonality of the wave functions. Hence an extra AB phase can be accumulated between those trajectories as discussed in the reference [78]. This effect also depends on the potential profile of the tunnel-coupled wire. When the confinement is stronger, this effect should be smaller. From the simulation in ref. [78], this effect becomes larger at higher magnetic field and weaker tunnel coupling (wider tunneling barrier) because the difference of the center of mass between the two states becomes larger. But this does not fully explain the experimental observation for an obvious reason. Once the wave functions are shifted towards y-direction, $|\psi_\mathrm{S}\rangle$ and $|\psi_\mathrm{A}\rangle$ approaches $|\uparrow\rangle$ and $|\downarrow\rangle$, similarly to the tunnel-coupled wire with a potential offset. When the influence of the Lorentz force becomes more significant, it simply approaches the situation where the AB ring is not closed. According to the simulation for a similar interferometer[78], the visibility is already reduced by an order of magnitude when the AB area increases by less than 5%.

The other possibility to account for the larger AB area is the "non-adiabaticity" where an electron does not immediately fall onto the eigenstates when it enters a weakly tunnel-coupled wire. But we need further careful studies in terms of reproducibility and consistency for different parameters such as the wire length, wire width, the magnetic field, and the tunnel-coupling strength.

3.6 Summary and future plans

We found distinct interferences in an AB ring with tunnel-coupled wires. In the SCR, where an AB ring is connected to ohmic contacts through a single quantum wire, the system is equivalent to a two-terminal AB ring structure and we observed in-phase oscillations in two contacts. When the geometrical phase was modulated by the gate voltage, the phase of the AB oscillation at zero field was fixed to either 0 or π, which is a clear signature of the phase rigidity. On the other hand, in the WCR the AB ring is connected to the contacts through the tunnel-coupled wire on the right, where a superposition state of the upper and the lower path in the AB ring can be fully transferred to the one of the symmetric and anti-symmetric hybridized states in the tunnel-coupled wire. Furthermore the system is equivalent to a three terminal and for each of the output currents in the right leads phase rigidity is no longer maintained. As a result the observed quantum interference becomes a *true* two-path interference and the two output currents oscillate with anti-phase. When the geometrical phase was modulated in this WCR, the phase of the AB oscillation smoothly shifts as expected. The possibility of the unambiguous phase measurement was further confirmed by both analytical and numerical calculations [77, 78].

We also found a difference of the area where an electron acquires the AB phase between two regimes. In particular an electron seems to acquire the AB phase also in the tunnel-coupled wire region in the WCR. However the mechanism of the AB phase acquisition has still to be investigated and further studies using different length and width of a tunnel-coupled wire will be required.

Chapter 4

Flying charge qubit operation in an Aharonov-Bohm ring with tunnel-coupled wires

4.1 Introduction

A qubit in solid-state systems is attractive for quantum information since it has an advantage in scalability. In particular spin qubits with quantum dots made in GaAs/AlGaAs 2DEG systems are intensively studied and single qubit operation and two qubit operation have already been reported [21–23]. These spin qubits are localized, and it is difficult to transfer information from one place to the other, which should be useful for networking quantum systems and performing complicated quantum calculations. As a technology to realize such information transfer, recently a single electron transfer between distant QDs connected through a depleted quantum channel driven by surface acoustic wave within its typical spin coherence time $T_2^* \sim 10$ ns has been demonstrated (see chapter 8) [25, 26]. Also information transfer by capacitive coupling between qubits was proposed theoretically [79]. However there has been no demonstration of scalable 'flying qubit' architectures in solid-state systems, where quantum operations on qubits are performed while they are coherently transferred.

When pseudo spin states are defined by a traveling electron in either of the two paths, a two-path interferometer can be considered as a two-level system. It can be used to make a flying qubit by controlling the phase difference and superposition of the two states. From this point of view Mach-Zehnder interferometers of quantum Hall edge channels [80, 81] are considered to be useful for making flying qubits and in addition are rich testing grounds

for quantum physics such as two-particle interference [30, 82]. However, phase relaxation length of such a device was shown to be 24μm at 20 mK [81]. This, together with the requirement of a high magnetic field, limits their scalability. On the other hand, the AB ring with tunnel-coupled wires described in chapter 3 works under a low magnetic field without quantum Hall edge channels. As we will see later in this chapter, this makes the system less sensitive to voltage fluctuations of the environment and this increases the phase relaxation length of the system. In this chapter we describe quantum operations of a flying qubit and explain its specific features [76].

4.2 Device and measurement

The device and the measurement technique used in this chapter are basically the same as the one used in chapter 3 (See section 3.2). However we used two different setups in the experiments. Setup A is the one shown in Fig. 3.2, where all lines are filtered by a copper powder filter and a two stage RC-filter at base temperature. In Setup B we put cold grounds connected to ohmic contacts through certain resistances (Fig. 4.1) in addition to Setup A. Currents $I_{1(2)}$ flowing through the two contacts at the right side are converted from voltages $V_{1(2)}$ measured across the load resistance R using $I_{1(2)} = V_{1(2)}/R$. When R is large, the output voltage becomes large and the measurement resolution is improved, but the large resistance reduces the currents flowing through the device since it is connected in series to the device. Therefore we chose the resistance comparable to the resistance of the device ($\sim 10\text{k}\Omega$) in the experiments described in this chapter, where $V_{1(2)}$ becomes the most sensitive to the device conductance. Usually in the low temperature measurement thermoelectric voltage between the room temperature and low temperature parts of each line is different by a few tens of μV, which produces an offset voltage between the ohmic contacts and reduces quantum interference effect. In Setup B the electrical potential of each contact is determined at low temperature by a cold ground and hence dephasing due to the thermoelectric voltage can be suppressed. However we cannot make ohmic contacts floating during the measurement as in Setup A. For the transport measurement a lock-in technique with a source-drain voltage of $8 \sim 50$ μV and reference frequency $f = 23.3$ Hz was employed. All measurements were done at the base temperature of ~ 70 mK except when the temperature is specified. Again in this chapter a QD was not used but we just applied a negative voltage on the center plunger gate out of the three to form a quantum channel.

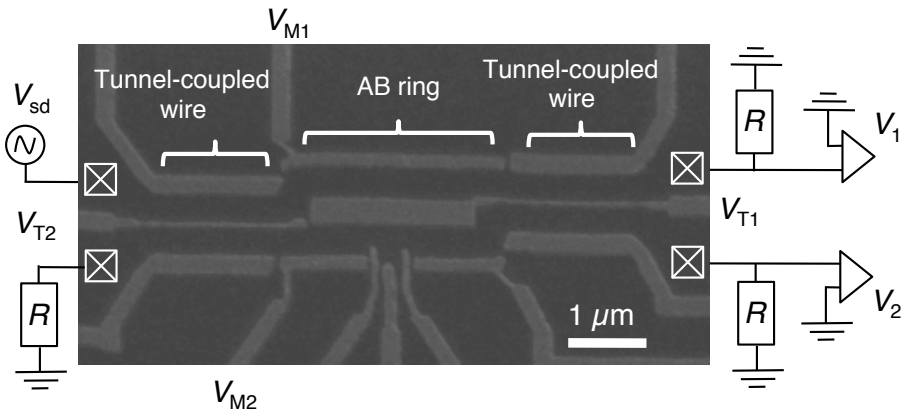

Fig. 4.1 Measurement setup for Setup B. In this setup a cold ground is put for each ohmic contact through resistance ($R = 10\text{k}\Omega$). A current flowing through a contact is calculated by $I = V/R$.

4.3 Flying qubit operations

Flying qubit operations in an AB ring with tunnel-coupled wires are described in this section. Operations of the system are considered in terms of pseudo spins ($|\uparrow\rangle$, $|\downarrow\rangle$) defined by the presence of an electron in either of the two wires (Fig. 4.2a). Figure 4.2b shows the Bloch sphere for a pseudo spin. We performed rotation about X-axis, and Z-axis in one of the tunnel-coupled wires, and an AB ring, respectively. Combination of the two operations allows to perform Ramsey-type interference experiments.

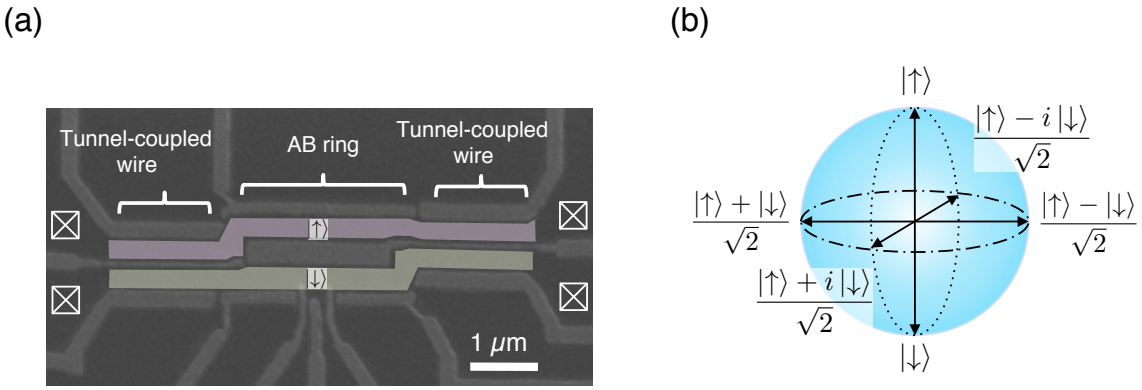

Fig. 4.2 (a) Definition of pseudo spins and (b) Bloch sphere of the pseudo spins

Firstly the X-axis rotation is considered. When there is no energy detuning between the

upper and lower part of the wire, operation of a tunnel-coupled wire can be written by

$$U_{\mathrm{T}}(\theta) = \cos\left(\frac{\theta}{2}\right)\left[\,|\uparrow\rangle\langle\uparrow| + |\downarrow\rangle\langle\downarrow|\,\right] + i\sin\left(\frac{\theta}{2}\right)\left[\,|\uparrow\rangle\langle\downarrow| + |\downarrow\rangle\langle\uparrow|\,\right], \tag{4.1}$$

where $\theta = (k_{\mathrm{S}} - k_{\mathrm{A}})L$ as discussed in section 2.1.4. In this operation an electron-state accumulates phase difference θ between the two eigenstates in a tunnel-coupled wire $\psi_{\mathrm{S}} = \frac{|\uparrow\rangle+|\downarrow\rangle}{\sqrt{2}}$, $\psi_{\mathrm{A}} = \frac{|\uparrow\rangle-|\downarrow\rangle}{\sqrt{2}}$, which corresponds to the rotation about X-axis (the axis connecting ψ_{S} and ψ_{A}) in the Bloch sphere (Fig. 4.3). It is possible to control θ by applying a gate voltage on the thin center gate of one of the two tunnel-coupled wires, which changes the tunnel-coupling energy τ as well as $(k_{\mathrm{S}} - k_{\mathrm{A}})$ between the two parts of the wire. When the kinetic energy of the propagating direction is large enough compared to the tunnel-coupling energy, the rotation angle θ can be written by

$$\begin{aligned}\theta &= (k_{\mathrm{S}} - k_{\mathrm{A}})L \\ &\approx \frac{2\tau}{\hbar}\cdot\Delta t \\ &= \frac{E_{\mathrm{A}} - E_{\mathrm{S}}}{\hbar}\cdot\Delta t\ ,\end{aligned} \tag{4.2}$$

where τ is the tunnel-coupling energy, Δt is traversing time of an electron through the tunnel-coupled wire and $(E_{\mathrm{A}} - E_{\mathrm{S}})$ is the energy difference between the two eigenstates. In our measurement when anti-phase oscillations are observed in the Weak Coupling Regime (WCR), this condition is usually satisfied.

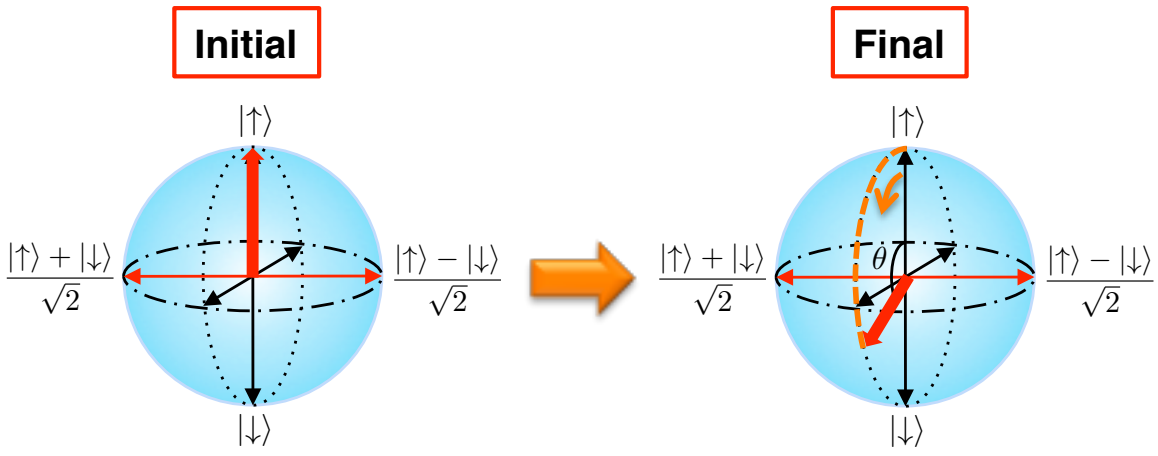

Fig. 4.3 Rotation about X-axis.

We initially perform the rotation about the X-axis in the tunnel-coupled wire in Setup A at $T \sim 2.2$ K to prevent current fluctuations due to impurity scattering which become larger

at lower temperatures. Since we have two tunnel-coupled wires in the device, we use one of them to demonstrate the X-rotation. We inject a current from the upper (lower) contact at one end of the coupled two wires to initialize the spin state to $|\uparrow\rangle$ ($|\downarrow\rangle$), and measure the current flowing through the upper or lower contacts at the other end. Fig. 4.4a shows the

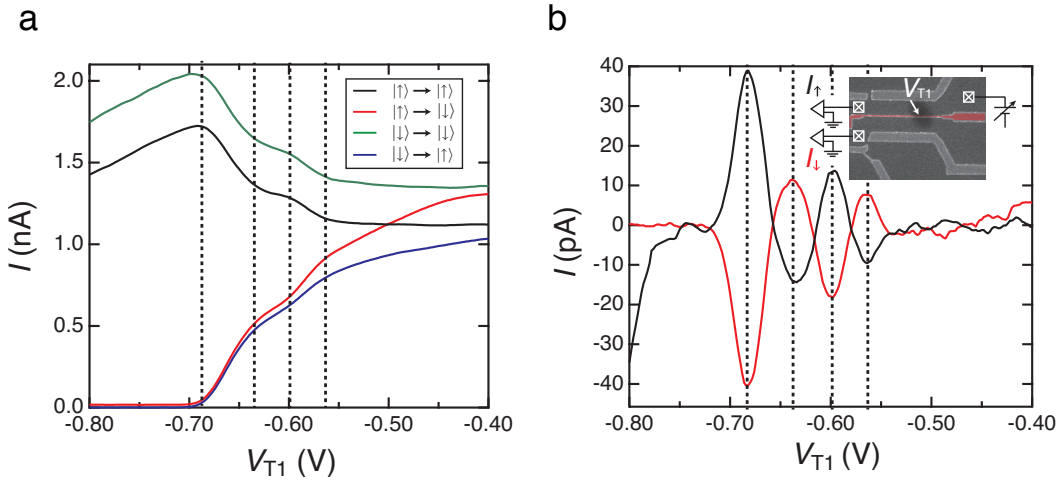

Fig. 4.4 Current oscillation as a function of V_{T1} (Fig. 2 in ref. [76]). (a) Raw data observed at the upper and lower contacts when the current is injected from both the upper and lower contacts. (b) Main: oscillating part of the current oscillation shown in (a). Inset: measurement setup. A source-drain bias of $V_{sd} = 50\ \mu$V, $f = 23.3$Hz is applied and the temperature is ~ 2.2 K.

output currents as a function of the voltage V_{T1} applied to the right tunnel-coupling gate. The black, and red curve is the data observed at the upper, and lower contact, respectively when the current is injected from the upper contact as shown in the inset of Fig. 4.4b. The green, and blue curve is the current observed at the lower, and upper contact, respectively when the current is injected from the lower contact. The currents from $|\uparrow\rangle$ to $|\uparrow\rangle$ ($|\downarrow\rangle$) and from $|\downarrow\rangle$ to $|\downarrow\rangle$ ($|\uparrow\rangle$) oscillate in the same way, which ensures that the observed oscillations do not come from the balance of the conductance between the two wires. Fig. 4.4b shows the oscillating part of the current in Fig. 4.4a when the current is injected from the upper wire. At around $V_{T1} = -0.68$V the two wires are totally decoupled. For more positive gate voltage, the current oscillations become clearer. One oscillation period corresponds to 2π rotation and hence in total 3π rotation is observed. The oscillation disappears for more positive gate voltage than -0.54 V. This is because the tunnel-coupled wire approaches a single quantum wire in such a strong tunnel-coupling condition.

Next the operation in the AB ring is described. When a *pure* two-path interference is

considered, an electron acquires a phase difference between the upper and lower arm of the AB ring as discussed in section 2.2.3, which corresponds to the rotation about Z-axis (axis connecting $|\uparrow\rangle$ and $|\downarrow\rangle$) in the Bloch sphere. This unitary operation can be written by

$$U_{\mathrm{AB}}(\varphi) = |\uparrow\rangle\langle\uparrow| + \mathrm{e}^{i\varphi}|\downarrow\rangle\langle\downarrow| \ , \tag{4.3}$$

where $\varphi = \oint \mathrm{k}\cdot \mathrm{d}\boldsymbol{l} - \frac{e}{\hbar}BS$ is the phase difference accumulated in the AB ring.

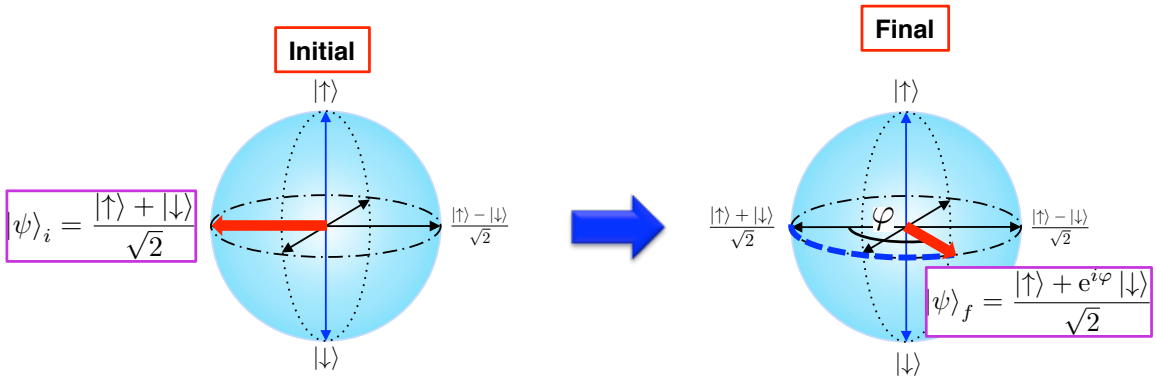

Fig. 4.5 Rotation about Z-axis.

We also confirm this rotation about Z-axis in the WCR. For this measurement we employ the three-terminal configuration and Setup A as in section 3.3. In that configuration the initial state is $|\psi_i\rangle = \frac{|\uparrow\rangle+|\downarrow\rangle}{\sqrt{2}}$ and then a phase difference φ is accumulated across the AB ring. Finally the resulting state vector is rotated about X-axis in the right tunnel-coupled wire by θ and the measurement of current I_1 and I_2 reads the projection onto Z-axis. Therefore the two output currents are expected to be

$$\begin{aligned} I_1 &\propto \left| \langle\uparrow| U_{\mathrm{T}}(\theta) U_{\mathrm{AB}}(\varphi) \left(\frac{|\uparrow\rangle + |\downarrow\rangle}{\sqrt{2}} \right) \right|^2 \\ &= \frac{1 - \sin\theta\sin\varphi}{2} \end{aligned} \tag{4.4}$$

$$\begin{aligned} I_2 &\propto \left| \langle\downarrow| U_{\mathrm{T}}(\theta) U_{\mathrm{AB}}(\varphi) \left(\frac{|\uparrow\rangle + |\downarrow\rangle}{\sqrt{2}} \right) \right|^2 \\ &= \frac{1 + \sin\theta\sin\varphi}{2} \ . \end{aligned} \tag{4.5}$$

In the measurement the tunnel-coupled wire is tuned to maximize the oscillation as a function of φ and hence θ is considered to be $\pi/2 \pmod{\pi}$. As a consequence I_1 and I_2 are expected to oscillate with anti-phase by the rotation about Z-axis. Fig. 3.4b and Fig. 3.9a are the data of Z-rotation with φ controlled by the magnetic field. Fig. 3.6b also shows

Z-rotation but with modulation of the geometrical phase through V_{M1}.

Finally we demonstrate the scheme of Ramsey interference employing Setup B, where the initial state $|\uparrow\rangle$ is prepared by injecting electrons from the upper contact and two $\theta = \pi/2$-rotations about X-axis in the two tunnel-coupled wires and φ-rotation about Z-axis in the AB ring are performed. The final state is projected to Z-axis and measured by the currents I_1 and I_2 (Fig. 4.6). These currents I_1 and I_2 are expected to be as follows:

$$\begin{aligned} I_1 &\propto \left| \langle\uparrow| U_{\mathrm{T}}\left(\frac{\pi}{2}\right) U_{\mathrm{AB}}(\varphi) U_{\mathrm{T}}\left(\frac{\pi}{2}\right) |\uparrow\rangle \right|^2 \\ &= \frac{1-\cos\varphi}{2} \end{aligned} \tag{4.6}$$

$$\begin{aligned} I_2 &\propto \left| \langle\downarrow| U_{\mathrm{T}}\left(\frac{\pi}{2}\right) U_{\mathrm{AB}}(\varphi) U_{\mathrm{T}}\left(\frac{\pi}{2}\right) |\uparrow\rangle \right|^2 \\ &= \frac{1+\cos\varphi}{2} \,. \end{aligned} \tag{4.7}$$

Therefore I_1 and I_2 should oscillate with anti-phase as in the three-terminal case.

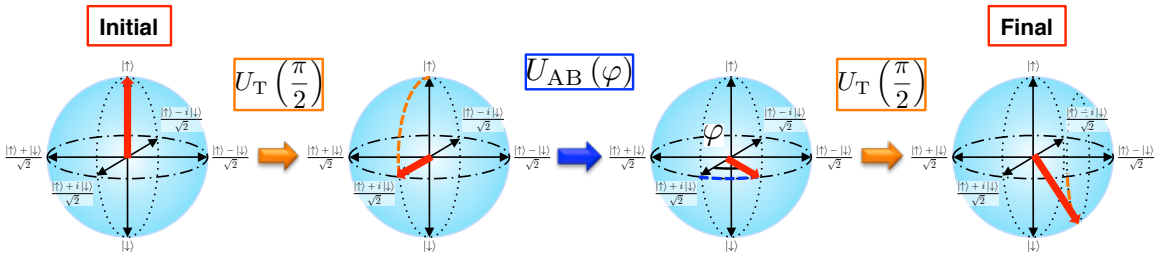

Fig. 4.6 Ramsey interference in an AB ring with tunnel-coupled wires.

For tuning the tunnel-coupled wires with $\theta = \pi/2 \pmod{\pi}$, we carefully adjust the gate voltages V_{T1} and V_{T2} to maximize the oscillation amplitude. Fig. 4.7 shows the amplitude of the magneto oscillation observed in I_1 as a function of the tunnel-coupling gate voltage. The oscillation amplitude is analyzed by a complex FFT and plotted as FFT amplitude. In both wires a peak structure appears and hence we set the gate voltages V_{T1} and V_{T2} to these values.

Then we perform the magnetic field control of φ. As expected from Eqs.4.6 and 4.7, the two output currents oscillate as a function of magnetic field (Fig. 4.8). We also modulate the rotation angle φ by changing the geometrical phase through $V_{\mathrm{M1(2)}}$. For both V_{M1} and V_{M2}, the AB oscillation phase smoothly shifts (Fig. 4.9). The phase shift with $V_{\mathrm{M1(2)}}$ is opposite between Fig. 4.9a and 4.9b, because V_{M1} modulates the wave vector of the upper path, whereas V_{M2} modulates that of the lower path. Here the shift of the geometrical phase is given by $\Delta\varphi = \Delta k_{\mathrm{F}} \cdot L_i = \frac{\pi C_i L_i}{2e} \Delta V_{\mathrm{Mi}}$, where $L_{1(2)}$ is the length of the gate $V_{\mathrm{M1(2)}}$ and $C_{1(2)}$

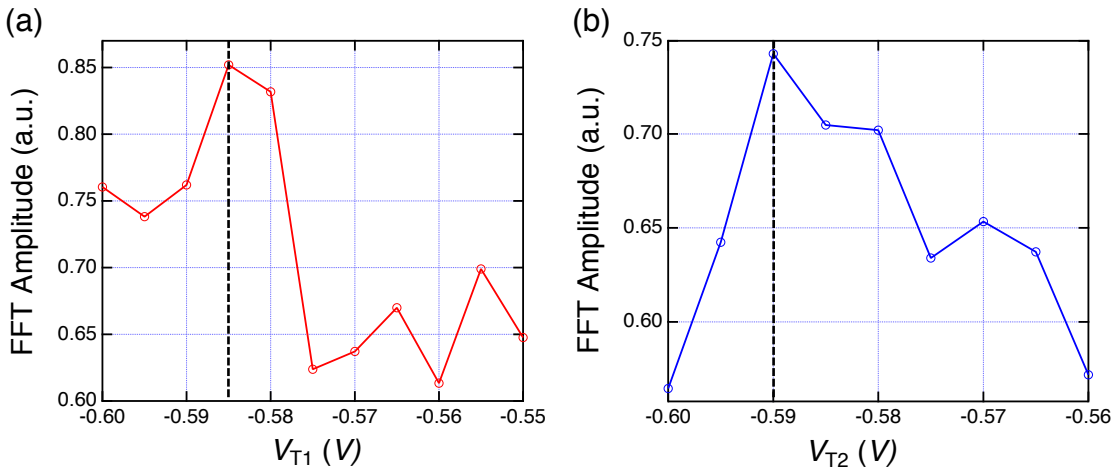

Fig. 4.7 Magneto oscillation amplitude for I_1 as a function of V_{T1} (a) and V_{T2} (b). Magneto oscillation ranging from -11.5 mT to 18.5 mT was analyzed by a complex FFT and oscillation amplitude is shown as FFT amplitude.

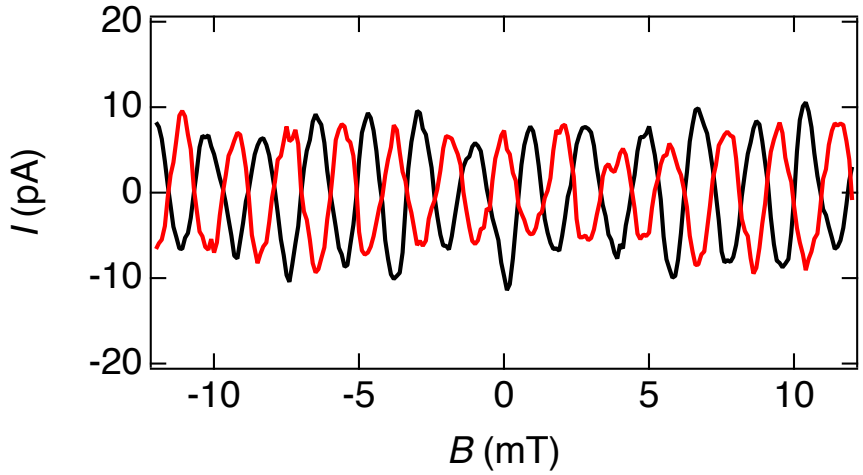

Fig. 4.8 Magnetic field control of rotation angle φ about Z-axis. Smoothed background currents are subtracted from raw data and only oscillating part is plotted. The black and red curves correspond to the currents observed in I_1 and I_2, respectively, measured for $V_{sd} = 50\ \mu$V.

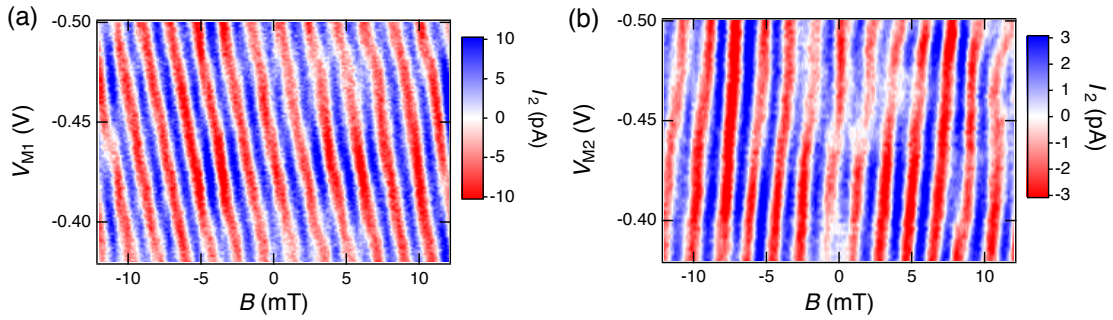

Fig. 4.9 Rotation about Z-axis in the scheme of Ramsey interference. Oscillating part of I_2 as a function of magnetic field extracted by subtraction of smoothed background is plotted for different voltages of V_{M1} (a) or V_{M2} (b), measured for $V_{sd} = 50\ \mu$V.

is the capacitance per length between the gate and the upper (lower) quantum wire. From this relation and data in Fig. 4.9, we can estimate $C_{1(2)}$ as follows:

$$\begin{aligned} C_1 &= \frac{2e(\Delta k_F \cdot L_1)}{\pi L_1 \Delta V_{M1}} \\ &= \frac{2 \cdot 1.6 \times 10^{-19}[\mathrm{C}] \cdot 4\pi}{\pi \cdot 2.73 \times 10^{-6}[\mathrm{m}] \cdot 0.16[\mathrm{V}]} \\ &\simeq 2.9\ [\mathrm{pF/m}] \end{aligned} \tag{4.8}$$

$$\begin{aligned} C_2 &= \frac{2e(\Delta k_F \cdot L_2)}{\pi L_2 \Delta V_{M2}} \\ &= \frac{2 \cdot 1.6 \times 10^{-19}[\mathrm{C}] \cdot \pi}{\pi \cdot 1.07 \times 10^{-6}[\mathrm{m}] \cdot 0.105[\mathrm{V}]} \\ &\simeq 2.9\ [\mathrm{pF/m}] \end{aligned} \tag{4.9}$$

These values are comparable to typical values of the geometrical capacitance of gates. In Fig. 4.9a the rotation angle φ about the Z-axis is modulated more than 2π by V_{M1}. The rotation angle θ about the X-axis can also be controlled by the gate voltage V_T and hence full control of the flying qubit can be done only by means of electrostatic gate voltages, which means that rapid manipulation of the qubit is possible. Furthermore considering the fact that the traversing time L/v_F of an electron through the entire structure is on the order of 10 ps, the operation time is much shorter than any of the other qubits in solid-state systems.

4.4 Electron coherence of the flying qubit

Coherence of electrons is crucial for quantum interference and long phase relaxation length is important for scalability of our flying charge qubit. Here we measure the temperature dependence of the quantum interference and deduce the corresponding phase coherence length l_ϕ from the amplitude of the interference in two different configurations of the flying qubit as schematically depicted in Fig. 4.10. In Configuration A the left tunnel-coupled

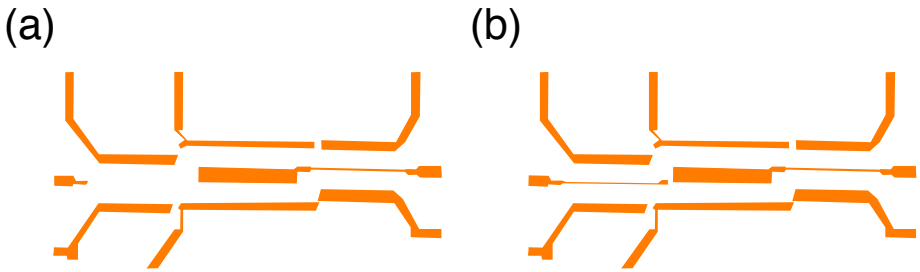

Fig. 4.10 Measurement configuration of temperature dependence: (a) The left tunnel-coupled wire is used as a single quantum wire and only the right one is tuned to a half beam splitter (Configuration A). (b) Both tunnel-coupled wires are tuned to a half beam splitter (Configuration B).

wire is not formed but just used as a single quantum wire, where a single rotation about the Z-axis and one rotation about the X-axis can be performed. The right tunnel-coupled wire is tuned to work as a half beam splitter to maximize the anti-phase oscillation as a function of magnetic field (see Eqs. 4.4, 4.5). In Configuration B both tunnel-coupled wires are used, so that a single rotation about the Z-axis and two rotations about the X-axis are performed. Both tunnel-coupled wires are tuned to a half beam splitter, which also maximize the anti-phase oscillation (see Eqs. 4.6, 4.7).

For both configurations we observe anti-phase oscillations as a function of magnetic field and analyzed the amplitude of $(I_1 - I_2)$ by performing a complex FFT to obtain the amplitude of the FFT component. Because the coherence of the electrons has to be kept over the interferometer to observe the oscillations, the amplitude of the oscillations reflects the coherence.

Fig. 4.11 shows the temperature dependence of the FFT amplitude measured for both configurations A and B. For both configurations the FFT amplitude exponentially decreases with increasing temperature in agreement with the previous experimental [46, 47] and theoretical works [48, 49]. The reduction of the AB amplitude is mainly explained by mainly two factors. One is the thermal smearing of the electron wave packet, which is expressed in the ballistic case to be proportional to $\exp(-\tau_L k_B T/\hbar)$, where $\tau_L = L/v_F$ (v_F: Fermi ve-

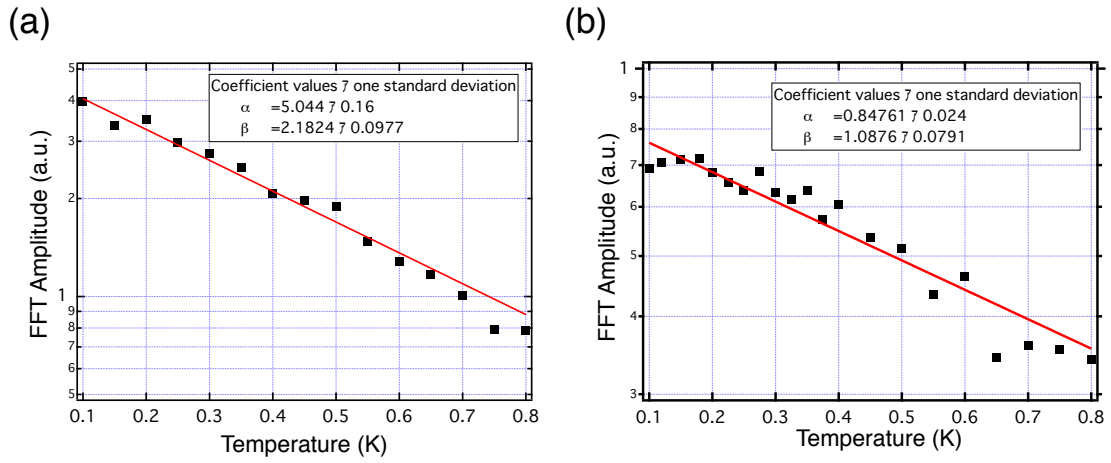

Fig. 4.11 Temperature dependence of FFT amplitude in two different configurations: (a) configuration A. (b) configuration B.

locity, L: length of the device). The other is the quantum decoherence, which contributes in proportion to $\exp(-\tau_{\rm L}/\tau_\phi(T))$. However a direct two-path interferometer with two arms of equal length is not affected by the thermal averaging [81] and hence the main contribution is the quantum decoherence.

As shown in Fig. 4.11, the oscillation amplitude of the present data can be fit by the function $\alpha\ \exp(-\beta T)$, where α and β are the fitting parameters. This result implies that τ_ϕ^{-1} is proportional to the temperature. The obtained value of β is 2.18 K^{-1} for (a) and 1.08 K^{-1} for (b), respectively. The phase relaxation length $l_\phi = L/\beta T$ is derived considering the relation of $L/l_\phi = \tau_{\rm L}/\tau_\phi(T) = \beta\ T$. The estimated l_ϕ at $T = 0.07$K is 30 μm in (a) and 86 μm in (b), respectively. Here the length of the device is 4.7 μm in (a) and 6.5 μm in (b), respectively. Note that the device length includes the length of the AB ring and one (two) tunnel-coupled wire(s) for Configuration A (B). The coherence length of Configuration A is estimated to be about three times shorter than that of Configuration B.

According to theories [48, 49], the main decoherence mechanism at low temperatures ($\lesssim$ 1K) is inelastic scattering induced by charge fluctuations inside the device or voltage fluctuations of the external contacts. Such a mechanism does not play an important role in the tunnel-coupled wire since the two eigenstates of the symmetric and anti-symmetric hybridized state are not well spatially separated. Therefore decoherence is considered to occur in the AB ring. Among the two different sources of decoherence, inelastic scattering induced by voltage fluctuation of the external contacts can be suppressed when the average injectivity of electrons from the contacts to the upper and lower path of the AB ring is set

to be equal [49]. This may explain the large difference of the coherence length between the two configurations. In Configuration A the average injectivity in the right side is controlled to be equal by the tunnel-coupled wire, but it is not in the left side. On the other hand in Configuration B it is controlled to be equal in both sides. More detailed studies about various tunnel-coupling conditions are required to figure out the results clearly. Nonetheless the important conclusion is that the coherence length of 86 μm at $T = 0.07$ K in Configuration B ensures the scalability of our flying qubit. This value is much longer than that reported for a Mach-Zehnder interferometer of a quantum hall edge state [81], in which limited coupling between the interferometer and the reservoir via only a few edge channels makes the interferometer sensitive to the charge fluctuations [48].

4.5 Summary and future plans

We have described the flying charge qubit operation in an AB ring with tunnel-coupled wires in the WCR. Rotations about X, and Z axis were performed in a tunnel-coupled wire, and an AB ring, respectively. Furthermore all operations can be performed by means of electrostatic gate voltages, and therefore fast qubit control is possible. We also investigated the temperature dependence of the oscillation amplitude and found that our flying qubit is highly coherent at low temperatures especially when both tunnel-coupled wires are tuned to work as half beam splitters.

The only drawback of the present arrangement is the low visibility of $\sim 0.3\%$. Because the coherence length is found to be much longer than the interferometer length, decoherence is not the origin of this low visibility. The visibility should be improved by optimizing the device design. For example, there are two possible 'geometrical' reasons for the low visibility. First, the entrance and exit of the tunnel-coupled wires are so narrow that the conductance may be restricted there and backscattering may occur. Second, there is a contribution from several transmitting channels in each part of the tunnel-coupled wires and in each arm of the AB ring, although only one in each wire contributes to the main oscillation. A possible remedy is to make use of a high-electron-density heterostructure to define strongly confined single-mode channels, and to make the electrons propagate through them without suffering from backscattering. Indeed, we have significantly improved the visibility up to ~ 10 % by using a high-electron density heterostructure and by defining narrower channels.

In addition to the quantum information transfer, it should also be possible to create a non-local entanglement state following the scheme proposed in refs [5] and [83], combined

with single electron sources [84, 85] to synchronize qubits. This flying qubit can also be used in combination with a static qubit [86]. Using a high-mobility heterostructure with a mean free path exceeding 100 μm, we would in principle be able to integrate 100 qubits because each quantum operation, including two-bit operation is performed within a 1 μm scale.

Chapter 5

Transmission phase across a quantum dot in the Kondo regime

5.1 Introduction

The Kondo effect, an archetype of many-body correlations, arises from the interaction between a localized spin and surrounding conduction electrons [58]. It is characterized by a many-body singlet ground state, often referred to as the Kondo cloud. It was first observed in metals with a small inclusion of magnetic impurities and manifests itself by the increase of the electrical resistance at low temperatures. The advance in nanotechnology has led to a revival of the Kondo effect, as it is now possible to study the interaction of a single impurity spin in contact with an electron reservoir, in particular in semiconductor quantum dots [59, 61]. These developments have also allowed access to the phase shift across a Kondo impurity, a central ingredient of Noziéres' celebrated Fermi-liquid theory for the low-energy fixed point of the Kondo effect [1]: when an electron of sufficiently low energy is incident on the impurity in the screened singlet state, it scatters coherently off the latter, acquiring a $\pi/2$ phase shift, but with zero probability for a spin flip. This $\pi/2$ phase shift is one of the hallmarks of the Kondo effect. Though it cannot be measured directly in conventional Kondo systems, it has been suggested [2] to be possible for a semiconductor quantum dot placed in one arm of an Aharonov-Bohm ring, where the transmission phase through the dot can be extracted from the Aharonov-Bohm oscillations of the conductance as a function of magnetic flux through the ring [3, 8]. For such geometries it has been predicted that the $\pi/2$ phase shift should persist, perhaps surprisingly, even up to temperatures as high as the Kondo temperature, T_{K} [15, 87].

Such Kondo phase measurements have indeed been pursued in a number of pioneering

experiments [12, 13, 88–90]. However, unexpected results have been obtained for the phase shift in the Kondo regime ($T \lesssim T_K$): Ref. [12] reported a $(3/2)\pi$-phase shift across two successive Coulomb peaks (CPs) for $T < T_K$ and Ref. [13] reported a $\pi/2$-phase shift across each CP, but at a temperature so high ($T/T_K \gtrsim 30$) that a $\pi/2$-phase shift is not expected theoretically. The theoretically expected $\pi/2$-phase shift in the Kondo regime has therefore stayed elusive.

Indeed, the measurement of the true transmission phase through a quantum dot in an Aharonov-Bohm (AB) setup is not at all trivial. Contributions from electrons that encircle the AB loop multiple times alter the phase of the observed AB oscillation and makes impossible to extract the *true* transmission phase through a quantum dot. The most conspicuous example is the so-called phase rigidity [7, 11] in a two-terminal setup. It has been shown that employing multi-terminal devices can lift the phase rigidity [3, 9, 12, 13, 88]. In a series of previous phase measurements, suppression of multiple path contributions was then assumed by observation of the smooth phase shift of the AB oscillation induced by the gate voltage shift.

Here we employ an original approach to measure the transmission phase shift through a quantum dot, using an AB ring with tunnel-coupled wires as a *pure* two-path interferometer (see also chapter 3). The unique advantage of our method is that it is possible to exclude multiple path contributions by checking the two output contacts, which is not possible for other multi-terminal devices. In the following we describe the experimental study of the phase behavior related to the Kondo effect in terms of our original method [1].

5.2 Device and measurement

We use two devices with slightly different geometries, which we call Device C and D, respectively. Both devices are fabricated in a 2DEG ($n \approx 3.21 \times 10^{11}$ cm^{-2}, $\mu \approx 0.86 \times 10^6$ cm^2/Vs, and depth = 100nm) formed at an AlGaAs/GaAs hetero-interface with a standard Schottky gate technique. A current is injected from the lower left contact by applying a source-drain voltage of 3 to 20 μV with $f = 23.3$ Hz and is measured at the right contacts. The output current $I_{1(2)}$ is converted into the voltage $V_{1(2)}$ using the resistance $R = 10$ kΩ at the base temperature. The upper left contact is grounded at the base temperature. The QD is formed by three gates with voltages V_L, V_p and V_R. V_L and V_R are used to control the left

[1] Experiments presented in this section have been achieved in close collaboration with the group in Grenoble. In particular I performed the experiments in section 5.3, 5.4 using the equipments in Grenoble. I discussed the results a lot with Sylvain Hermelin, Tristan Meunier and Christopher Bäuerle.

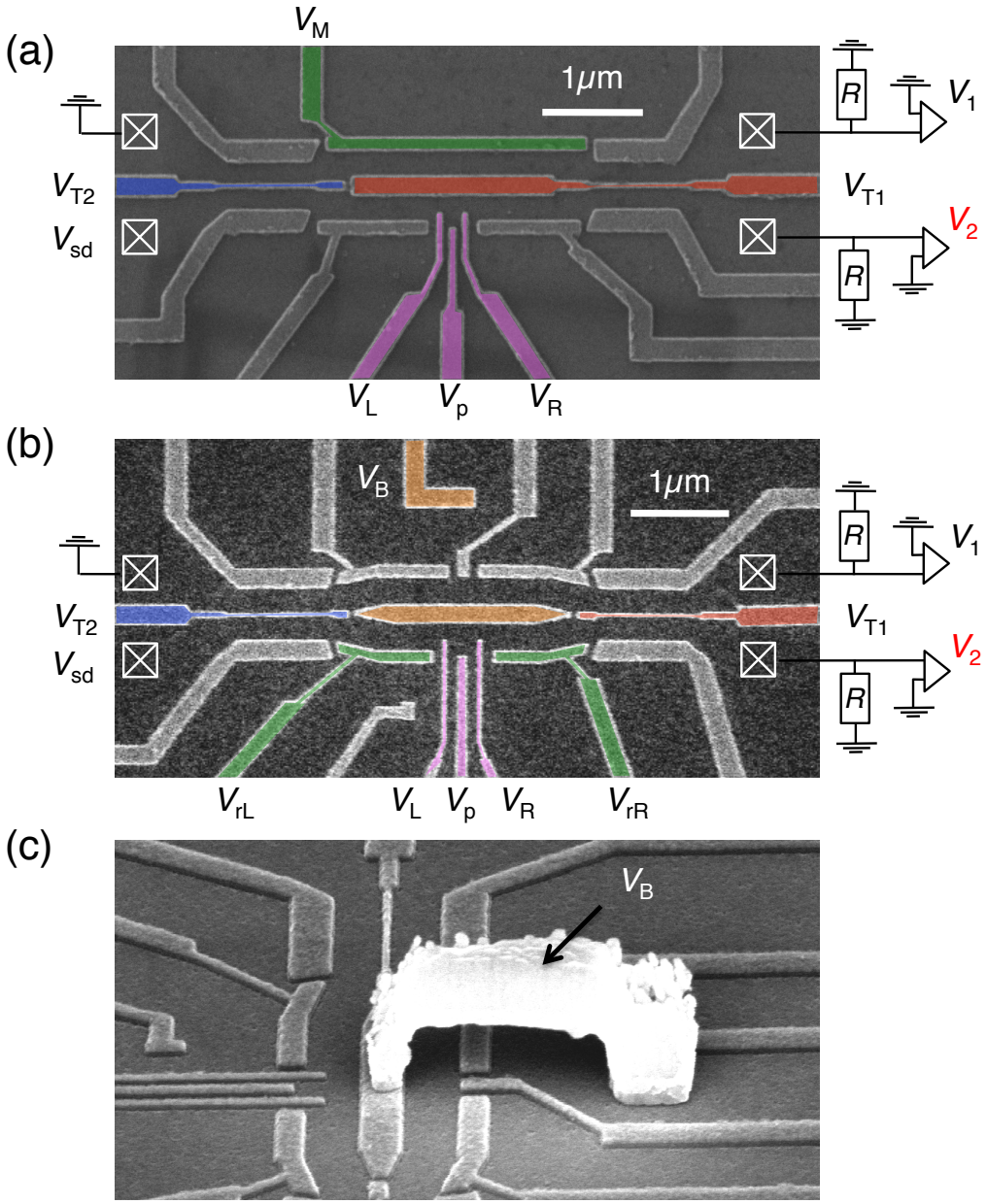

Fig. 5.1 (a), (b) SEM pictures of Device C (a) and Device D (b). (c) A SEM picture of Device D after the deposition of the metallic air bridge.

and right tunnel-barrier, respectively and $V_{\rm p}$ is used to control the energy level of the QD.

The QD size in Device C (Fig. 5.1a) is smaller than that in Device D (Fig. 5.1b). Another important difference is that the right tunnel-coupling gate with voltage $V_{\rm T1}$ is electrically isolated from the AB ring. The AB ring is formed by the gate with voltage $V_{\rm B}$ contacted via a metallic air bridge in Device D as shown in Fig. 5.1c. This difference allows more flexible tuning of the QD in Device D.

For the phase measurements the Ramsey interference scheme (see Fig. 4.9) is employed, where the two output currents oscillate with anti-phase as a function of phase φ accumulated across the AB ring. When we form the QD embedded into the lower arm of the AB ring, φ also depends on the transmission phase $\varphi_{\rm dot}$ accumulated across the QD. Since the initial state is $|\downarrow\rangle$ in the experiments here, the two output currents are represented by

$$I_{1(2)} \propto \frac{1+(-)\cos\varphi}{2} \tag{5.1}$$

$$\varphi = \oint \boldsymbol{k}\cdot \mathrm{d}\boldsymbol{l} - \frac{e}{\hbar}BS + \varphi_{\rm dot}\ . \tag{5.2}$$

Therefore observation of such an anti-phase current oscillation allows us to detect the phase shift across the QD.

5.3 Transmission phase shift across a Coulomb peak

We first examine the transmission phase across a *normal* QD without the Kondo correlation, or by setting the temperature much higher than the Kondo temperature. Device C is used for this measurement to form a small quantum dot so that transport is assumed to be mediated by a single level. Transport only through the QD is achieved by depleting the left tunnel gate $V_{\rm T2}$: the corresponding current I_2^* is shown in Fig. 5.2a. For the phase measurement, the left tunnel-coupled wire is tuned to work as a half beam splitter. The magnetic field dependence of the two output currents I_1 and I_2 are recorded for various values of $V_{\rm p}$ and the oscillating parts are extracted by performing a complex fast Fourier transform (FFT) and filtering out the noise outside the peak region, followed by an inverse complex FFT. The dependence of the transmission phase shift on $V_{\rm p}$ is extracted from the phase evolution of the magneto oscillations as it is shown in Fig. 5.2b. Reliable transmission phase can not be extracted for $V_{\rm p} > -0.623$V because the oscillation is significantly disturbed by charge noise. It must be noted that it is very important to use only nice anti-phase oscillations for analysis, otherwise extra contributions smear the real transmission phase.

The current I_2 mimics nicely the CP, with background current due to the current flowing

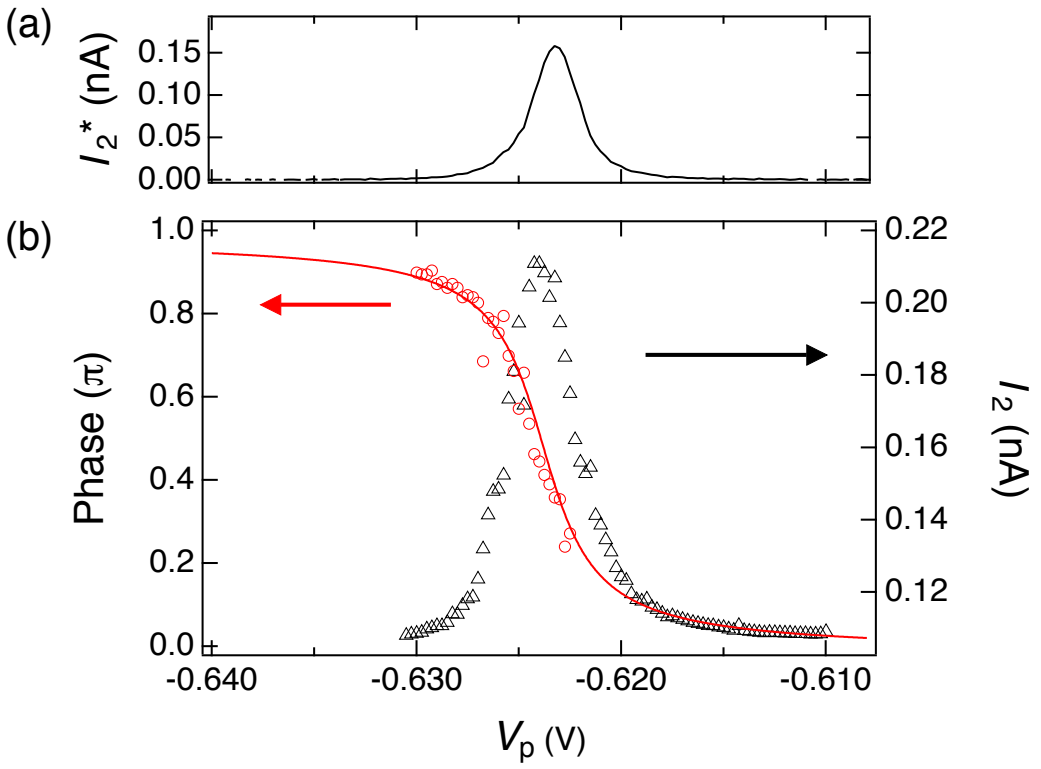

Fig. 5.2 (a) Coulomb peak of the QD in the Coulomb blockade regime in Device C, where I_2^* corresponds to the current passing only through the QD by completely depleting the left tunnel gate V_{T1}. The energy level of the QD is scanned across the Fermi energy by changing the plunger gate voltage V_p. A charging energy $U \sim 1.8$ meV, a tunnel-coupling energy $\Gamma \sim 40$ μeV and a single level spacing $\delta \sim 230$ μeV are estimated by mapping out the Coulomb diamond (not shown here). (b) Phase evolution across the Coulomb peak extracted from the anti-phase oscillations is plotted on the left axis (red circles). The current collected in I_2 is plotted on the right axis (black triangles), where I_2 is averaged over one oscillation period of magnetic field. The solid line shows the transmission phase determined from the shape of the Coulomb peak in I_2 using Friedel's sum rule (see text).

through the upper path. The change in the transmission phase, $\Delta\varphi_{\mathrm{dot}}$, with changing plunger gate voltage is related to the corresponding charge change ΔN in the QD (in units of the electron charge) via Friedel's sum rule, $\Delta N = \Delta\varphi_{\mathrm{dot}}/\pi$ [14]. ΔN as a function of V_{p} is given by the integrated area under the CP (with the background subtracted), divided by the total area of the CP. The measured phase shift shown by the red circles across the CP is in very good agreement with the phase extracted using Friedel's sum rule [14] shown by the solid line.

5.4 Transmission phase shift in the Kondo regime

In the last section we have confirmed a π-phase shift across a CP in the Coulomb blockade regime using Device C as reported in previous experiments [3]. The device is then tuned into the Kondo regime by adjusting V_{L}, V_{p} and V_{R} (see Fig. 5.1a). We first characterize the QD using transport measurements only through the dot. Fig. 5.3a shows the temperature dependence of two CPs, where the Kondo effect appears in the valley between the two peaks around $V_{\mathrm{p}} = -95$ mV. The current I_2^* in the valley increases as the temperature is lowered, a clear signature of the Kondo effect. As we do not reach the unitary limit, T_{K} cannot be determined with high precision, but we find an upper bound of approximately 100 mK from the temperature dependence of I_2^*. Fig. 5.3b shows a Coulomb diamond in this Kondo regime and a clear maximum (vertical yellow ridge) is observed around $V_{\mathrm{sd}} = 0$ V in the Coulomb blockade region, usually referred to as zero bias anomaly.

The transmission phase across these two CPs is then measured by opening the left tunnel gate V_{T1}, and recording the AB oscillations for various V_{p} in Fig. 5.4a. In this experiment the energy scale of the magnetic field is lower than that of the temperature, so that spin is not resolved [91], however, we see clear signatures of the Kondo effect. Already in the raw data, a clear phase shift of approximately $\pi/2$ in the Kondo valley is observed, as indicated by the dotted lines in Fig. 5.4a. To reveal the phase shift across the CPs even more clearly, we determine the phase for each V_{p} by calculating the complex FFT over a field range extending from -50 mT to -80 mT. The obtained transmission phase is presented in Fig. 5.4b, together with I_2. A total phase shift of π when scanning through the two successive CPs is observed and a clear plateau appears at $\pi/2$ in the Kondo valley. This result contrasts with the phase shift across a *normal* CP. Although the conductance does not reach the unitary limit, the transmission phase shift in the Kondo valley already shows the $\pi/2$-phase shift, which is consistent with theoretical predictions that the $\pi/2$-phase shift survives for temperature as large as $T \sim T_{\mathrm{K}}$ [15, 87].

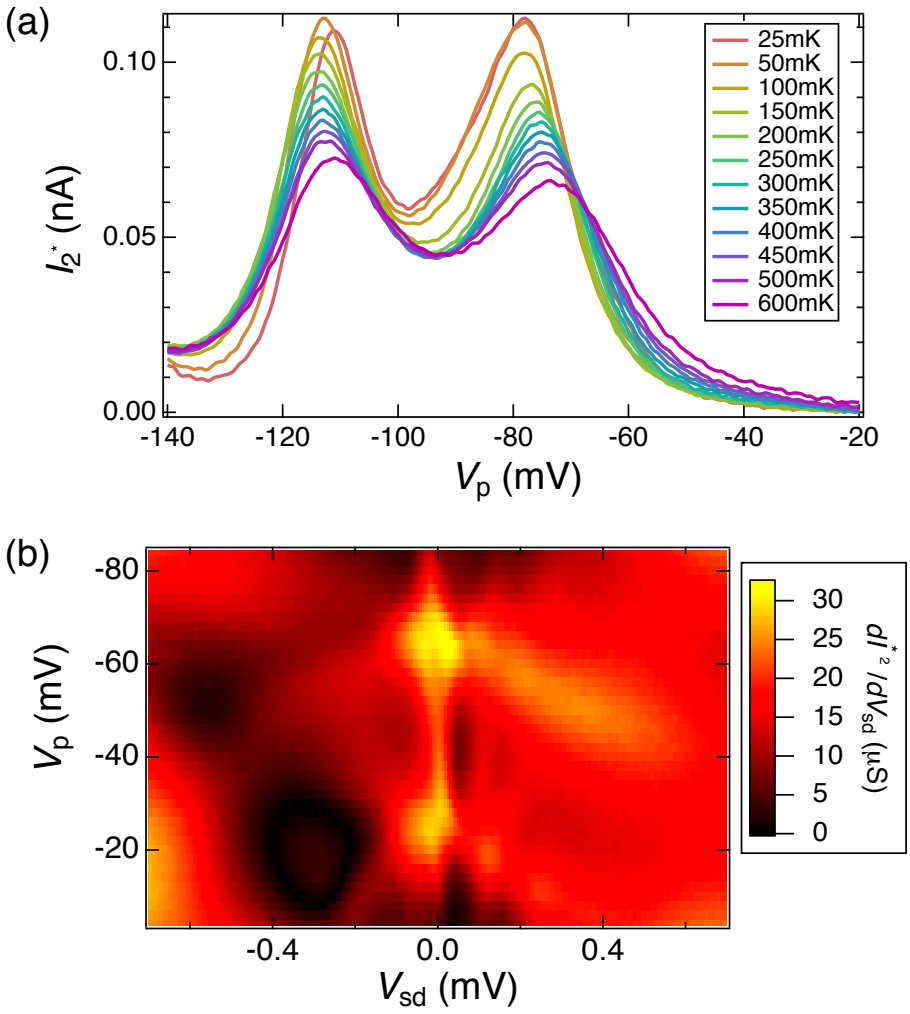

Fig. 5.3 (a) Temperature dependence of two Coulomb peaks which shows Kondo correlations, observed in I_2^* plotted as a function of V_p, where the left tunnel gate V_{T1} is depleted. Here $V_{sd} \sim 3.5\ \mu eV$ is applied to measure the current. (b) Coulomb diamond in the Kondo regime ($T \lesssim T_K$).

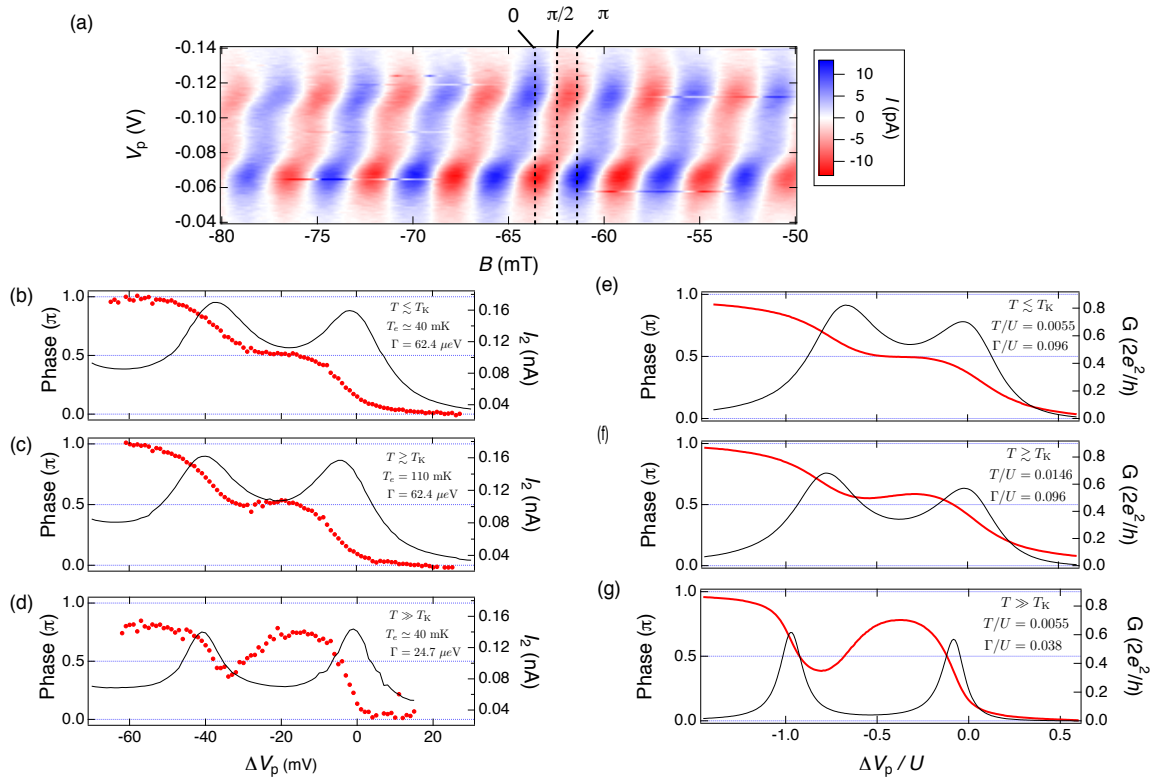

Fig. 5.4 (a) AB oscillation amplitude as a function of magnetic field, obtained by scanning the plunger gate voltage V_p across two successive Coulomb peaks, showing Kondo correlations in the valley between them ($T \lesssim T_K$). The AB oscillation amplitude is obtained from $I = I_1 - I_2$ by subtracting a smoothed background. Dotted lines emphasize the phase shift. (b), (c), (d), The transmission phase (red circles, left axis), determined by a complex FFT of the anti-phase oscillations, together with I_2 (black line, right axis), plotted as a function of the change ΔV_p in plunger gate voltage with respect to its value at the center of the right CP, for three different regimes, (b): $T \lesssim T_K$, (c): $T \gtrsim T_K$ and (d): $T \gg T_K$. I_2 is averaged over one oscillation period of magnetic field. Parameters shown in the figures are estimates, extracted from fitting NRG results to the measured phase curves. (e), (f), (g), Transmission phase (red line) and conductance (black line) calculated by a two-level Anderson impurity model with $s = +$ and the lower level being the Kondo level, for an interaction energy $U = 650$ μeV and a level spacing of $\delta = 0.5U$ (for details see Suppl. materials). Fitting parameters used for the calculations are shown in the figures. Current I_2 of the experimental data (b), (c), (d) contains a linear background from the upper arm of the interferometer whereas the conductance G in the theoretical calculations (e), (f), (g) is the bare conductance across a QD.

When increasing the temperature to approximately 110 mK, the Kondo correlations are reduced ($T \gtrsim T_K$) and the behavior of the transmission phase is slightly altered. The phase climbs slightly above $\pi/2$ before decreasing slightly, forming an *S*-shape (Fig. 5.4c) in the Kondo valley. To further reduce the Kondo correlations, we reduce the coupling energy Γ by suitably tuning V_L, V_p and V_R to lower the Kondo temperature (Fig. 5.4d) such that $T \gg T_K$. In this regime, the *S*-shape structure of the phase evolution is more pronounced and becomes asymmetric with respect to the valley center and the value $\varphi_{dot} = \pi/2$. This suggests that by further reducing the Kondo correlations the phase behavior across each CP would become the same as that observed for *normal* CPs. These results differ strikingly from the observation of ref. [13], where a $\pi/2$-phase shift is observed when $T \gg T_K$.

To further corroborate our findings we perform numerical renormalisation group (NRG) calculations of the conductance as well as the transmission phase [2]. We find that even when the single level spacing δ is larger than Γ, the contribution from multiple levels on the dot plays an important role for the phase behavior. In particular, taking into account only a single level results in a phase evolution, which is symmetric with respect to the centre of the Kondo valley, contrary to our experimental findings (see Fig. 5.4d). In order to accurately reproduce the experimental phase data, we therefore employ a two-level Anderson model (see Appendix A.1). It is crucial to choose correctly the relative sign of the tunnel-coupling coefficients for fitting the data of Fig. 5.4d, since this sign characterizes the influence of the nearby orbital level on the phase evolution. From fitting the predicted phase evolution to the one observed experimentally (see Appendix A.2), it is possible to estimate experimental parameters such as Γ and δ with good precision, which are not easily accessible from the measured conductance data, due to renormalization of the CPs by the Kondo effect. In addition, we can precisely evaluate the Kondo temperature, $T_K \sim 50$ mK for Figs. 5.4b and c. From the temperature evolution of the $\pi/2$-plateau, which is most prominent close to T_K, we are able to evaluate the actual electron temperature of $T_e \sim 40$ mK, consistent with previous measurements in the same electromagnetic environment [92]. The most important finding, however, is the fact that the $\pi/2$-phase shift persists up to a temperature of T_K and then evolves into an *S*-shape at higher temperatures, which is extremely well captured by the NRG calculations.

[2] NRG calculations presented here have been performed by Arne Alex, Andreas Weichselbaum and Jan vonDelft in Ludwig Maximilians-Universität in Munich.

5.5 The phase behavior below and around the Kondo temperature

In the section 5.4 we have found that the phase was locked at $\pi/2$ in the valley already at $T \lesssim T_K$ (Fig. 5.4b). This observation is somewhat surprising because the $\pi/2$-phase shift is the feature of the Kondo singlet state, which should be robust only at $T \ll T_K$ [61, 93]. We address this issue in this section and investigate the phase behavior below the Kondo temperature ($T < T_K$). We use Device D for these measurements.

First we characterize the CPs with the Kondo correlation from the temperature dependence (Fig. 5.5a) and a zero bias anomaly of conductance in the Coulomb diamond (Fig. 5.5b) as performed in section 5.4. The centers of both tunnel-coupled wires are depleted to make all the injected current pass through the QD. Since the conductance at the valley center increases as the temperature is lowered and exceeds the value e^2/h between 100 mK and 120 mK, the Kondo temperature is assumed to be higher than 100 mK, and higher than the base temperature of ~ 70 mK. Therefore we can access the regime of $T < T_K$.

We investigate the transmission phase across these two CPs with the Kondo valley in between as slightly changing the gate voltages V_{rL}, V_L, V_p, V_R and V_{rR}. Basically when the gate condition of the QD is changed while keeping the number of electrons inside the QD unchanged, the charging energy U and δ are not so much affected but Γ can be modulated. By making V_{rL}, V_L, V_R and V_{rR} more negative, Γ becomes small.

Fig. 5.6 shows the results. Γ is the largest for (a), slightly smaller for (b) and the smallest for (c). The phase evolves smoothly by π with almost constant slope across the two peaks in Fig. 5.6a. Then in Fig. 5.6b the slope of the phase in the valley starts to be slightly moderate, which should be a signature of the phase locking feature around $\pi/2$. This phase locking feature is further enhanced in Fig. 5.6c for the smallest Γ and therefore for the largest T/T_K. From the temperature dependence of conductance and the gate voltage condition, we confirm that $T < T_K$ in Fig. 5.6a. Also for the condition in Figs. 5.6b and c the *S*-shape behavior observed in Figs. 5.4c and d does not appear yet, which indicates that the temperature is still lower than the Kondo temperature ($T < T_K$). From the results above the phase locking feature is enhanced when the Kondo temperature approaches the temperature under the condition of $T < T_K$. Considering also the result in section 5.4, it should be most enhanced at $T \sim T_K$ and then the *S*-shape phase appears for $T > T_K$.

The pronounced feature of the phase locking at $T \sim T_K$ can be qualitatively understood by the following scenario. At finite temperatures scattering across a QD involves both elastic and inelastic processes. However in our phase measurement only coherent electrons that

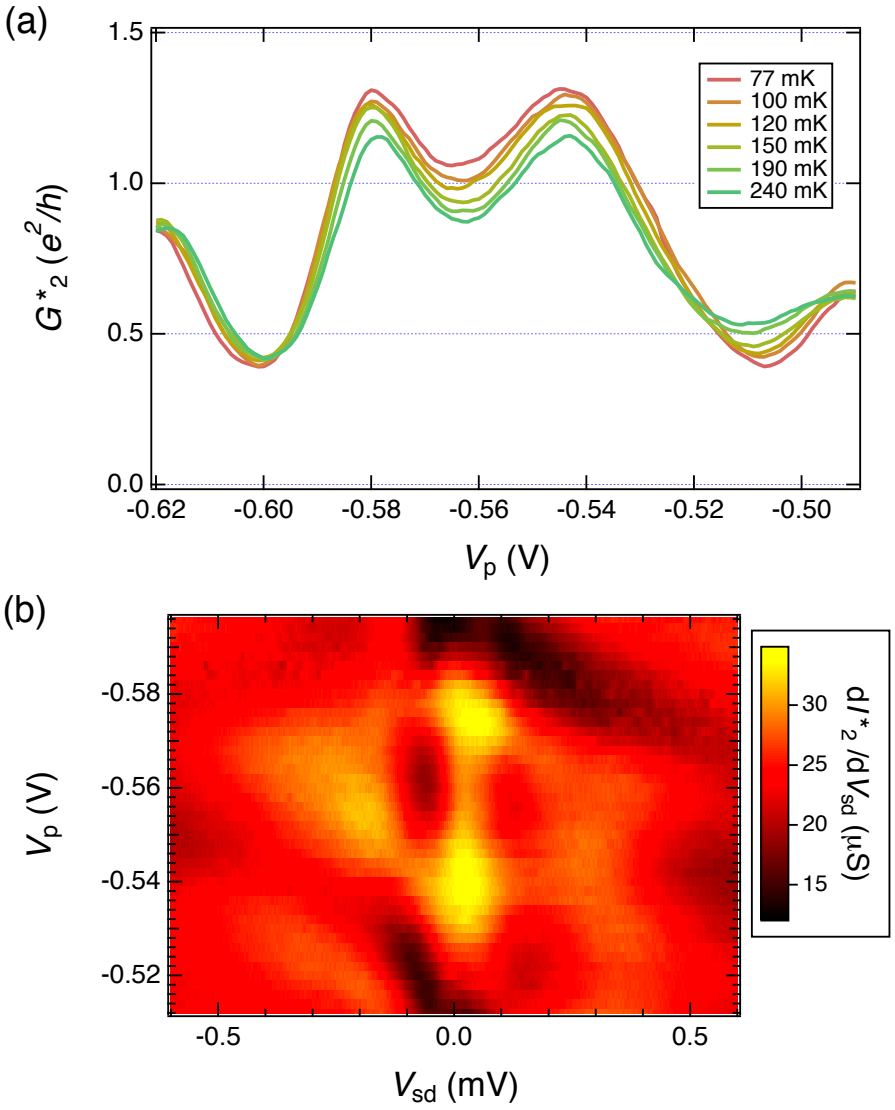

Fig. 5.5 (a) Temperature dependence of the two CPs with the Kondo correlation, where the conductance G_2^* is plotted as a function of V_p in units of (e^2/h). The conductance G_2^* is obtained by $I_2^*/V_\mathrm{sd}^,$, where $V_\mathrm{sd}^,$ is the voltage across the device given by $V_\mathrm{sd}^, = V_\mathrm{sd} - I_2^* \cdot R (= 10\mathrm{k}\Omega)$. (b) Coulomb diamond in the Kondo regime ($T = 70$ mK $< T_\mathrm{K}$).

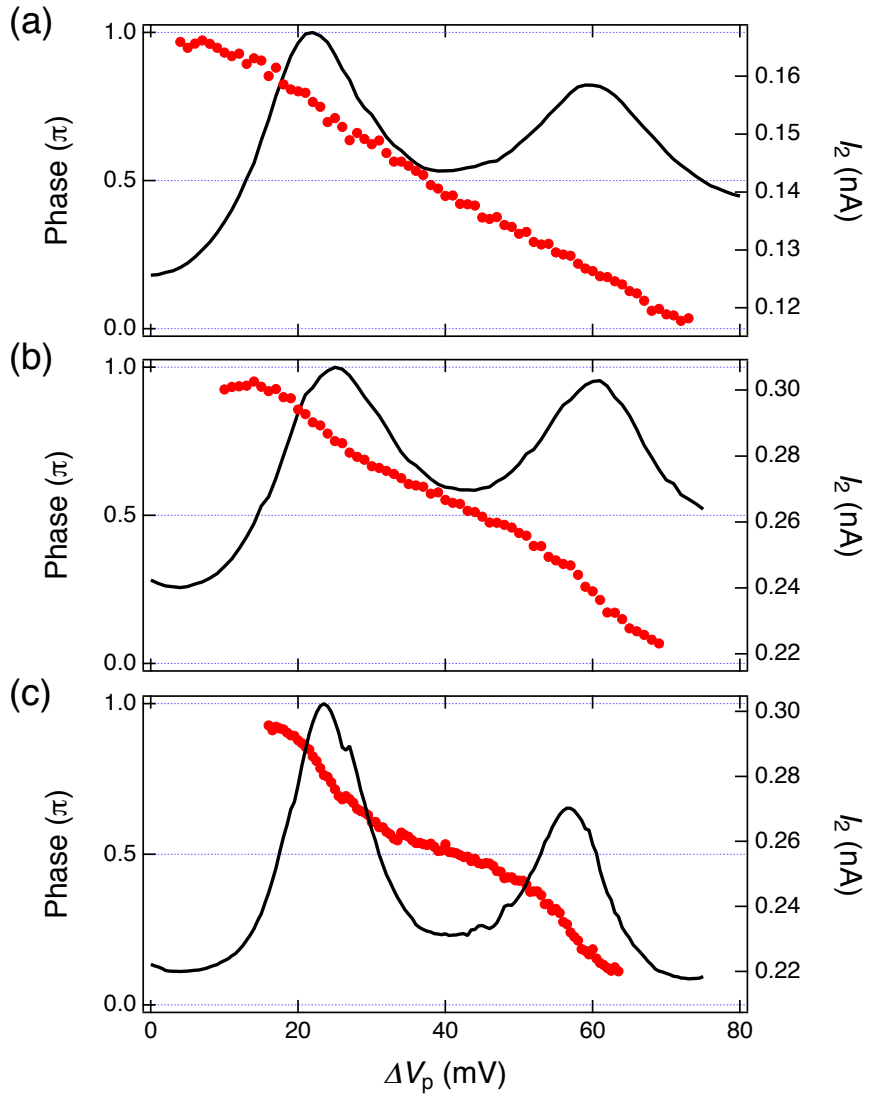

Fig. 5.6 The transmission phase (red circles, left axis), determined by a complex FFT of the anti-phase oscillations, together with I_2 (black line, right axis), plotted as a function of the plunger gate voltage ΔV_p for three different gate conditions. From the gate voltage around the QD, Γ is becoming smaller from (a) to (c).

are elastically scattered through a QD contribute to the interference. Theoretically when electrons are elastically scattered through the Kondo state with the energy shift $\Delta\varepsilon$ from the resonance for $T \leq T_{\mathrm{K}}$, they acquire the phase shift as follows:

$$\Delta\varphi(\Delta\varepsilon) = \frac{\pi}{2} + \frac{\Delta\varepsilon}{k_{\mathrm{B}}T_{\mathrm{K}}}. \tag{5.3}$$

In our phase measurement we observe the thermally averaged phase shift of electrons over the energy window of $\sim k_{\mathrm{B}}T$ around the Fermi energy. When the two CPs are well separated and the stable impurity spin is established around the valley center for $T \leq T_{\mathrm{K}}$, the Kondo state of Lorentzian type resonance in the energy domain is formed centered exactly at the Fermi energy. Since it is symmetric about the Fermi surface, the contributions from the above and below the Fermi energy are cancelled out and the averaged phase shift in the energy window becomes $\pi/2$. On the other hand closer to the CP the occupation of the impurity spin starts to fluctuate, which makes the Kondo resonance asymmetric about the Fermi energy with the resonance center slightly displaced from the Fermi energy. As a result the observed phase shift becomes different from $\pi/2$. For the one side the phase shift is smaller than $\pi/2$ and for the other it is larger. In Fig. 5.6 the phase smoothly evolves π across the two CPs and there is no $\pi/2$-plateau in the valley. This means that the impurity spin fluctuates over the valley due to the overlap of the tails of the two CPs. Only at the center of the valley the influence of the left and right CPs are balanced and the Kondo resonance becomes symmetric about the Fermi energy, where the $\pi/2$-phase shift is observed.

The smaller Γ is, the narrower the CPs become and the weaker the fluctuation of the impurity spin in the valley becomes. Consequently the phase shift inside the valley gets close to $\pi/2$ as shown in Fig. 5.6. Following this trend the $\pi/2$-phase shift in the valley is most enhanced at $T \sim T_{\mathrm{K}}$. For $T > T_{\mathrm{K}}$ the energy window becomes broader than the Kondo state and hence the relation in Eq. 5.3 does not apply, and therefore the *S*-shape behavior is observed in Fig. 5.4c and d. Here we modulated Γ. We also expect the enhancement of the phase locking feature when the temperature is increased below the Kondo temperature. For higher temperature the energy window of the transport becomes larger. As a result even when the Kondo state is slightly asymmetric about the Fermi energy around the valley center, the resonance giving a $\pi/2$-phase shift is covered by the energy window. The $\pi/2$-phase shift around the valley center is, hence, more robust for higher temperature as long as $T \leq T_{\mathrm{K}}$.

Conversely from the discussion above we can determine the Kondo temperature from the

temperature dependence of the transmission phase and by finding the temperature, where the $\pi/2$-phase shift is the most enhanced. This estimation has less uncertainty than the one obtained from the standard conductance measurement. The estimation from the conductance measurement requires a wide range of the temperature dependence. At higher temperatures unknown cotunneling contributions smear the conductance. Also the conductance usually suffers from unwilling series resistance and does not reach the unitary limit of conductance, which leads to another uncertainty. On the other hand, the estimation from the phase measurement only requires measurements around the Kondo temperature.

5.6 Phase behavior in the weak Kondo regime

In section 5.4 we have found that to reproduce the asymmetric phase behavior about the valley center and $\pi/2$ in the NRG calculations of Fig. 5.4d, the relative sign of the tunnel-coupling coefficients t_α^j between level j and channel α (i.e. $s = \mathrm{sgn}(t_\mathrm{L}^1 t_\mathrm{R}^1 t_\mathrm{L}^2 t_\mathrm{R}^2)$) plays an important role. The sign of s corresponds to the parity relation between the orbitals of nearby CPs, and it is theoretically predicted that it is also related to the appearance of a phase lapse (see also section 2.5). $s = +(-)$ means that the parity relation between the orbitals of nearby CPs is the same (different). In this section we experimentally investigated the relation between the asymmetric phase behavior at $T \gg T_\mathrm{K}$ and the orbital parity relation as well as the phase lapse. For the measurements described in this section we use Device D.

Here we study the phase behavior at the two different sets of the CPs with the Kondo correlation (Region A and B). We initially characterize the Kondo effect from the temperature dependence of the CPs and the zero bias anomaly (Fig. 5.7). Fig. 5.7a and c show the data in Region A and Fig. 5.7b and d show the data in Region B. For both regions, the conductance at the valley center decreases as the temperature increases. In Fig. 5.7a the conductance of the left peak decreases as the temperature increases, whereas the one of the right peak increases. This is because the asymmetry of the dot-lead coupling which is different between the two peaks determines the peak height at the higher temperature, but the asymmetry is masked by the renormalization due to the Kondo effect at the lower temperatures. A clear zero bias anomaly is also observed for the both regions.

We modulate Γ by changing the gate voltages V_rL, V_L, V_p, V_R and V_rR around the QD and measure the transmission phase in the two different regions. Firstly we measure the phase at a relatively large Γ. A smooth phase shift across the two peaks is observed in both regions in Fig. 5.8 as expected in the Kondo regime. Therefore we assume $T \lesssim T_\mathrm{K}$ in this condition. In Fig. 5.8a the total phase shift across the two peaks is about 0.4π, rather smaller than π.

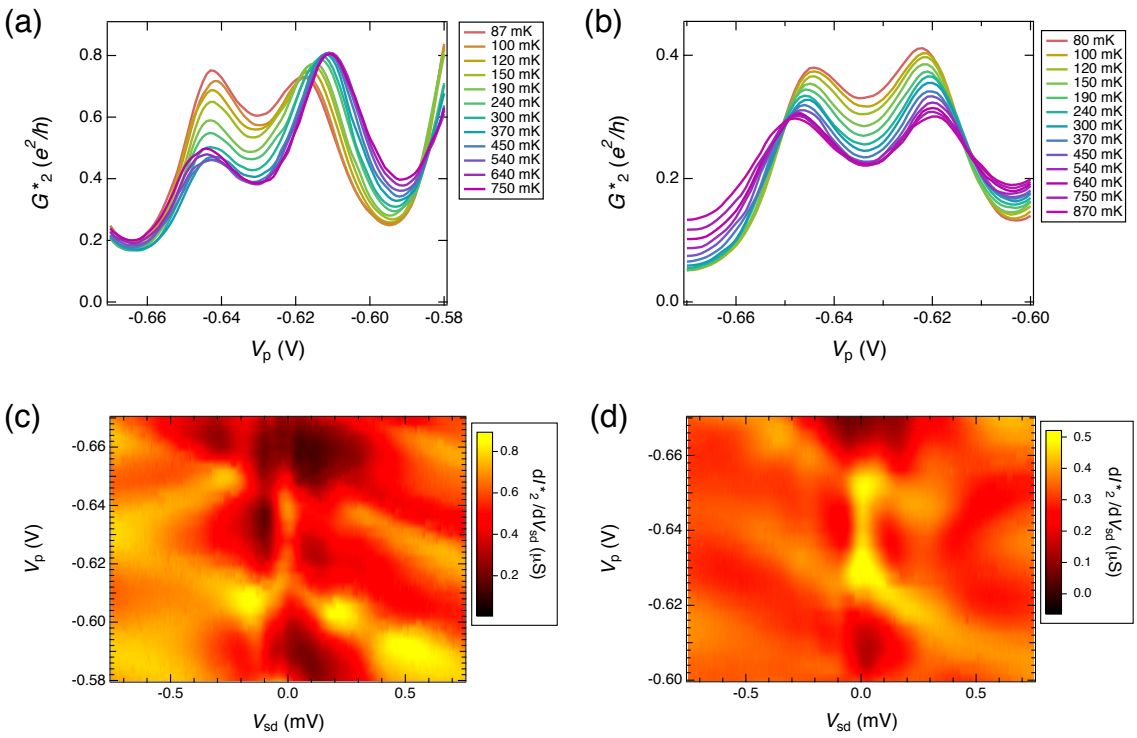

Fig. 5.7 (a), (b): Temperature dependence of the two CPs with the Kondo correlation, where the conductance G_2^* is plotted as a function of V_p in units of (e^2/h) at Region A (a) and B (b). The conductance G_2^* is obtained by $I_2^*/V_{sd}^{'}$, where $V_{sd}^{'}$ is the voltage across the device given by $V_{sd}^{'} = V_{sd} - I_2^* \cdot R(= 10\mathrm{k}\Omega)$. Here I_2^* is measured by depleting underneath the both tunnel-coupled wires, where all the injected electrons pass through the QD. (c), (d): Coulomb diamond observed at Region A (a) and B (b).

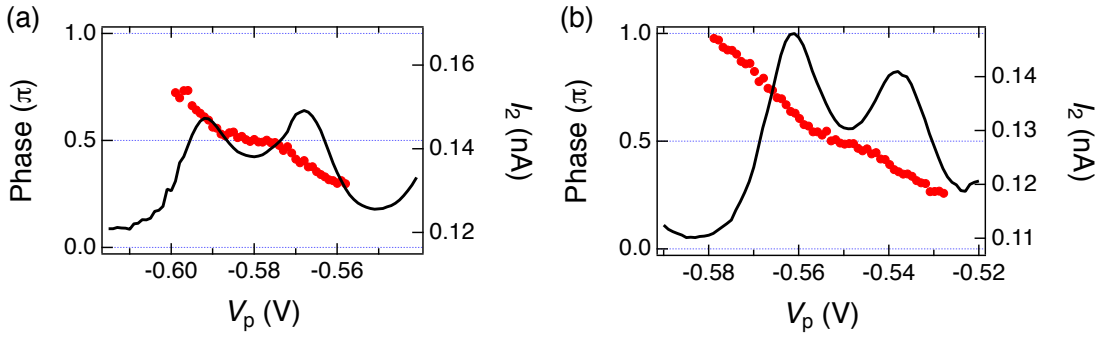

Fig. 5.8 Transmission phase shift at Region A (a) and B (b) in the Kondo regime ($T \lesssim T_K$).

There are two reasons for this: First when Γ is relatively large compared to U, the tails of the nearby CPs overlap and prevent a full phase shift of π. Second around the tail of a CP the conductance is usually small, and it is more difficult to perform reliable phase measurement due to small signal to noise ratio. This also prevents the observation of a full phase shift over the CP.

Then by tuning the gate voltages we reduce Γ as well as T_K and measure the transmission phase shift. The results are shown in Fig. 5.9, where the phase shows the asymmetric S-

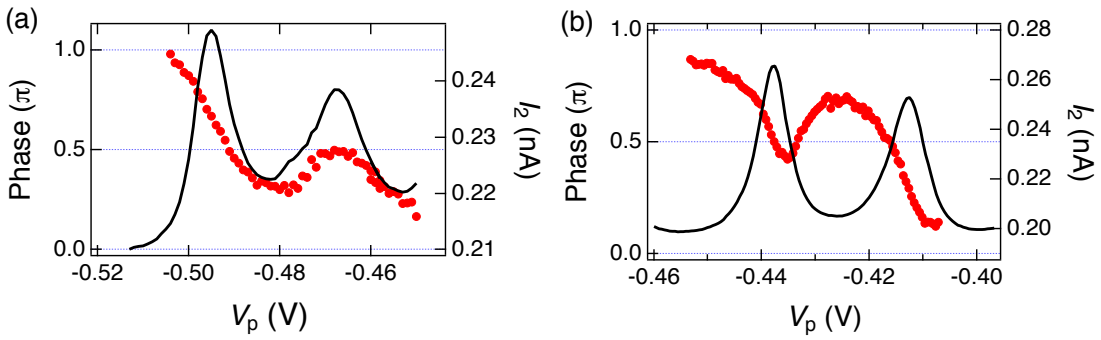

Fig. 5.9 Transmission phase shift at Region A (a) and B (b) in the weak Kondo regime ($T \gg T_K$).

shape behavior as observed in Fig. 5.4d and hence we consider that $T > T_K$. In Region A (Fig. 5.9a) the phase evolves more across the left CP than the right one, whereas in Region B (Fig. 5.9b) it is opposite. When we compare the asymmetry of the phase behavior with the NRG calculations in the weak Kondo regime ($T \gg T_K$) shown in Fig. A.1, the asymmetry of Fig. 5.9a is similar to the one in the two right CPs of Fig. A.1a and the two left CPs of Fig. A.1b. Accordingly the orbital parity relation between the corresponding orbital and the nearby orbital at the left of Region A is most probably $s = +$ and hence appearance of the phase lapse is expected between the left CP of Fig. 5.9a and the next CP at its left. On the other hand the nearby orbital at the right of Region A should have the orbital parity relation $s = -$ and no phase lapse is expected. From the same discussion $s = -$, i.e. no phase lapse is expected at the left of Region B and $s = +$, i.e. appearance of the phase lapse is expected at the right of Region B.

To confirm the above expectations, we measure the phase shift over the region including the nearby CPs. Fig. 5.10 shows the results. For Region B we measure the phase at the slightly different gate voltage condition from the one for Fig. 5.9b, but similar asymmetry is still maintained. Here we only plot the phase as a function of plunger gate voltage V_p, at which anti-phase oscillations are observed. This is because when the oscillations are not anti-phase, the interference is smeared by multiple-path contributions and hence the

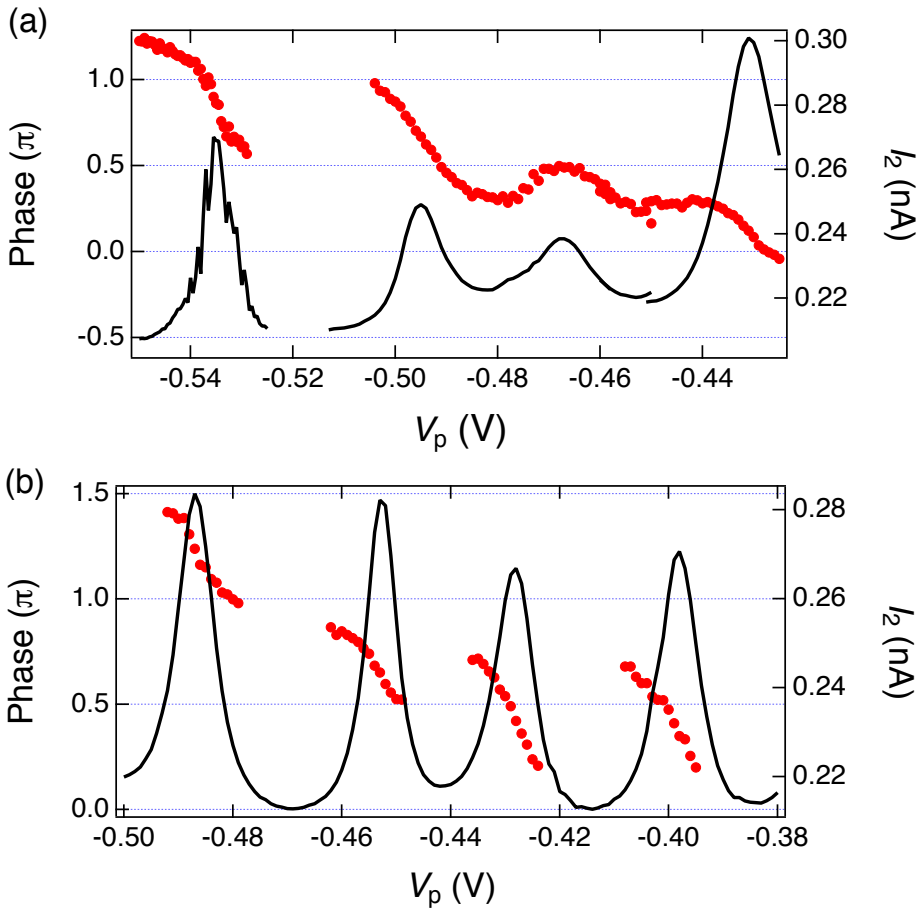

Fig. 5.10 Transmission phase shift across the four CPs including Region A (a) or Region B (b) as the two peaks at the center in the weak Kondo regime.

observed phase is not reliable. We indeed observe the phase lapse at the Coulomb valley predicted for $s = +$ and a smooth phase shift without the phase lapse at the valley predicted for $s = -$.

Consequently we confirm the correspondence between the experimentally observed asymmetric phase behavior and the one predicted by NRG calculations. Our observations lead to the conclusion that the asymmetric phase behavior in the weak Kondo regime depends on the orbital parity relation and which is further confirmed by the appearance of the phase lapse at the Coulomb valley with the nearby CPs.

5.7 Summary and future prospects

We studied the transmission phase shift across a QD with Kondo correlation. Firstly we confirmed the π-phase shift across a normal CP without the Kondo correlation to confirm the fact that our interferometer can be indeed used to measure the transmission phase across a QD with high precision. Then we observed the transmission phase shift in the Kondo regime. For temperatures lower than the Kondo temperature ($T \lesssim T_{\mathrm{K}}$), we observed a clear $\pi/2$-phase shift across each CP with a plateau in the valley in between. When the temperature becomes slightly higher than the Kondo temperature ($T \gtrsim T_{\mathrm{K}}$), an S-shape behavior appears in the valley. The S-shape behavior is further enhanced by increasing the temperature compared to the Kondo temperature ($T \gg T_{\mathrm{K}}$) and the phase behavior approaches to the one of normal CPs without Kondo correlation. We confirmed that these features are well reproduced by NRG calculations.

We also investigated the phase behavior in the Kondo regime ($T < T_{\mathrm{K}}$) and in the weak Kondo regime ($T \gg T_{\mathrm{K}}$). From the experiment in the Kondo regime we found that the phase locking feature around $\pi/2$ is enhanced when the temperature approaches the Kondo temperature. This result offers a new tool to determine the Kondo temperature with less uncertainty compared to the one using the normal conductance measurement. From the experiment in the weak Kondo regime we found that the asymmetry of the phase behavior about the valley center and $\pi/2$ is determined by the orbital parity relation between nearby CPs, which is also related to the appearance of the phase lapse.

The remaining problem is that when we carefully compare the Fig. 5.4b and e, c and f, correspondence between the current and the phase is different. In Fig. 5.4b across the right CP the phase starts to evolve near the middle of the peak ($\Delta V_{\mathrm{p}} \sim 0.15$ V), whereas in Fig. 5.4e the phase starts to evolve with increasing current. This difference may come from the fact that I_2 in Fig. 5.4b includes the current passing through the reference path,

whereas G in Fig. 5.4e is the conductance only through the QD. The other possibility is that in the experimental data the phase is determined only by elastic tunneling through the QD, whereas the NRG calculations of the phase include not only elastic processes but also inelastic processes. In this respect further studies are required.

Chapter 6

Transmission phase through a quantum dot near crossover from single level to multi-level transport

6.1 Introduction

Transmission phase across a QD with a relatively large number of electrons shows an universal behavior regardless of the details of the QD. The phase evolves by π across a CP. In the valleys between two CPs phase lapses appear. The phase jumps by π and returns to the initial phase before crossing the CP. Therefore the phase shift across two neighboring CPs becomes in-phase. This tendency is repeated over an extremely large number of CPs. Such an universal phase behavior has been observed in measurements employing a multi-terminal AB interferometer [3, 4], which works as a direct two-path interferometer and allows to extract the transmission phase under suitable conditions [94]. This universal behavior is a long standing puzzle in mesoscopic physics. Although it has been intensively studied theoretically [65–70], satisfactory explanation has not been given yet. Since the realization of a *pure* two-path interferometer is not trivial at all (see also chapter 3), only a few experiments related to this issue were reported [3, 4]. From these experiments the universal behavior is robust in wide range of parameters of QDs except for a small QD with only a small number of electrons ($\Gamma < \delta$, $N \leq 8$). The only other approach was to investigate the Fano effect in a quantum interferometer, where the in-phase behavior is expected to produce asymmetric tails of the CPs on the same side [95]. To further proceed understanding of the universal behavior, experiments in a *true* two-path interferometer are necessary.

Here we use our original two-path interferometer (chapter 3) to measure the transmission phase across a QD, which shows typical features of relatively large QDs. In particular we investigate the QD in the crossover region from $\Gamma < \delta$ to $\Gamma > \delta$.

6.2 Device and measurement

We use Device D (Fig. 5.1b, c, see also section 5.2), which has a relatively large QD. We employ the same measurement setup as in chapter 5 to perform the phase detection using the Ramsey interference scheme (see Fig. 4.9 and section 5.2).

6.3 Basic properties of the QD

We characterize the QD of Device D from the Coulomb diamond (Fig. 6.1a, c). We measure the phase in two different regions: (a) Region A and (b) Region B. The important feature of these diamonds is that the size of the Coulomb diamond is almost constant or only gradually smaller from the left to the right in a monotonic way, which is a typical feature of QDs with a relatively large number of electrons. When a QD is in the few electron regime, the size of the diamond changes non-monotonically reflecting the energy spectrum of orbitals [51].

In Region A the charging energy U is about $0.8 \sim 0.9$ meV. From the excitation line appeared around the peak 2A we estimate the single level spacing $\delta \sim 0.2$ meV, which is the upper bound of δ in this region. Although in this chapter we do not focus on the Kondo correlation, it is seen in the valleys between the peak 5A and 6A and between the peak 7A and 8A.

In Region B U gradually changes from 0.9 meV at the left (more negative V_{p}) to 0.5 meV at the right (more positive V_{p}) in Fig. 6.1a and c. To estimate δ we retune the QD to make the peak width narrower by reducing the coupling energy Γ between the QD and the leads and then observe the excitation lines. In this way δ is estimated to be about 0.2 meV around the peak 1B and hence for the peaks at more positive V_{p} δ is expected to be smaller. In Region B we also see the Kondo correlation in the valley between the peak 1B and 2B, between the peak 3B and 4B, and between the peak 7B and 8B though in fig. 6.1c and d it is only weakly featured. As known from the charging energy, Region B covers the region where a larger number of electrons are contained in the QD than that in Region A.

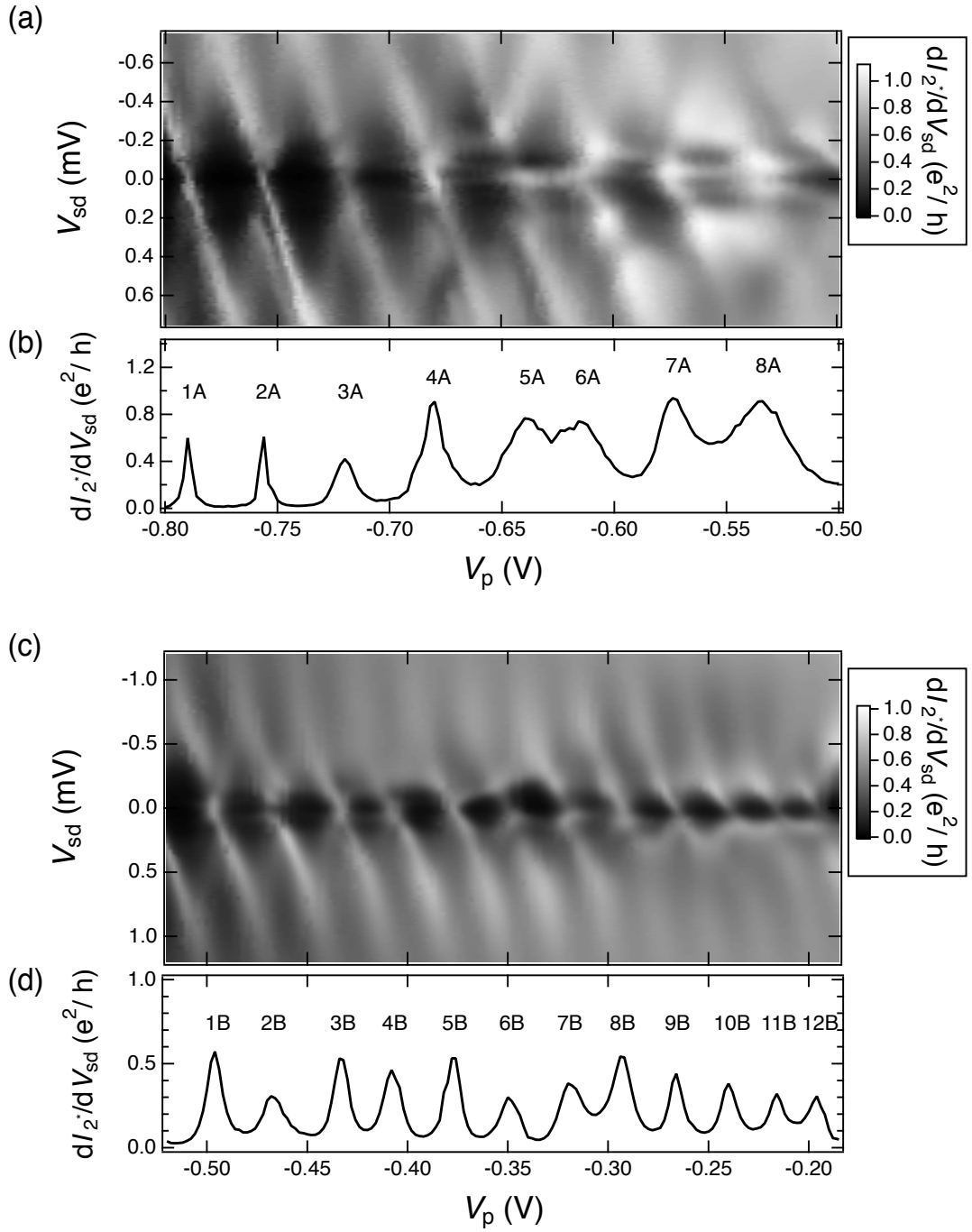

Fig. 6.1 Coulomb diamond (a), (c) and Coulomb oscillations at a zero bias voltage (b), (d) in two different regions. (a), (b) shows the data in Region A. (c), (d) shows the data in Region B. The differential conductance dI_2^*/dV_{sd} is measured by sweeping a DC voltage with a small AC voltage imposed on it, where I_2^* shows the current only through the QD by depleting underneath the both tunnel-coupled wire. The CPs are labeled for discussion.

6.4 Transmission phase across a QD in the many-electron regime

Firstly we measure the transmission phase shift in Region A. Fig. 6.2 shows the result. The black curve is the observed current I_2, showing the CPs on top of the background current flowing through the reference path. The red circle is the phase extracted from anti-phase oscillations by a complex fast Fourier transform (see Fig. 6.2). We can not measure the phase in some regions, where the current is so small that the signal to noise ration is not enough to resolve anti-phase oscillations. For each CP we estimate Γ from the full width of half maximum (FWHM). For the peak 1A and 2A Γ is smaller than δ and for the peak 3A to 8A Γ is larger than δ. In this crossover region from $\Gamma < \delta$ to $\Gamma > \delta$ the transmission

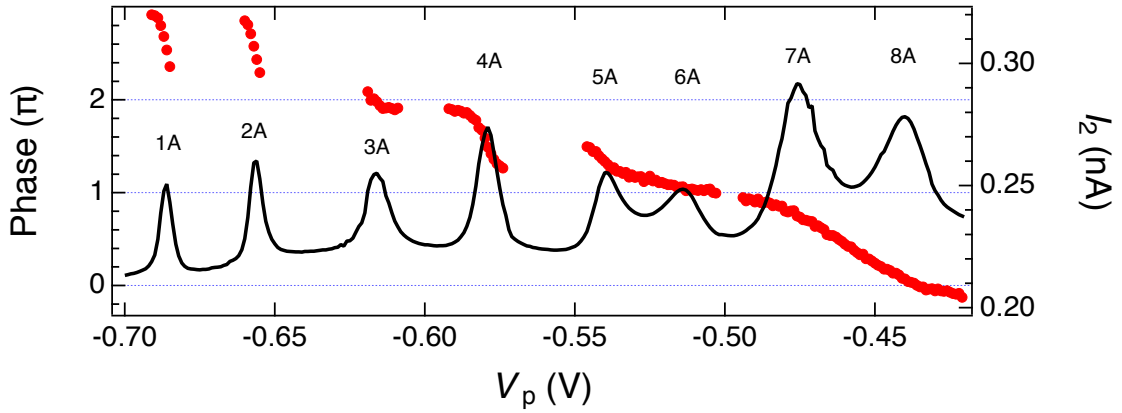

Fig. 6.2 The transmission phase (red circles and left axis) and the current (black line and right axis) as a function of the plunger gate voltage V_p in Region A.

phase behaves as if the system is mesoscopic. This means that the transmission phase shows various behaviors including valleys with and without a phase lapse, which is reflecting the characters of the QD. The total phase shift across the two peaks 7A and 8A (5A and 6A) should be π since the Kondo correlation is observed in the valley between them (see also chapter 5). From Fig. 6.2 the total phase shift across the two peaks 1A and 2A and those 3A and 4A is also π. In the valley between the peak 4A and 5A a phase lapse is observed, whereas in the valley between the peak 2A and 3A and between the peak 6A and 7A the phase smoothly evolves without a phase lapse.

For a peak with $\Gamma < \delta$, the phase behavior can be rather simply understood. It evolves π across the peak as expected from Friedel's sum rule [14]. It is the case observed for the peak 1A and 2A. On the other hand when $\Gamma > \delta$, electron transport across the QD is mediated by

more than two quantized levels. This makes the phase behavior more complicated compared to the single level case. It often leads to a smaller phase shift than π across a peak as seen for the peak 3A.

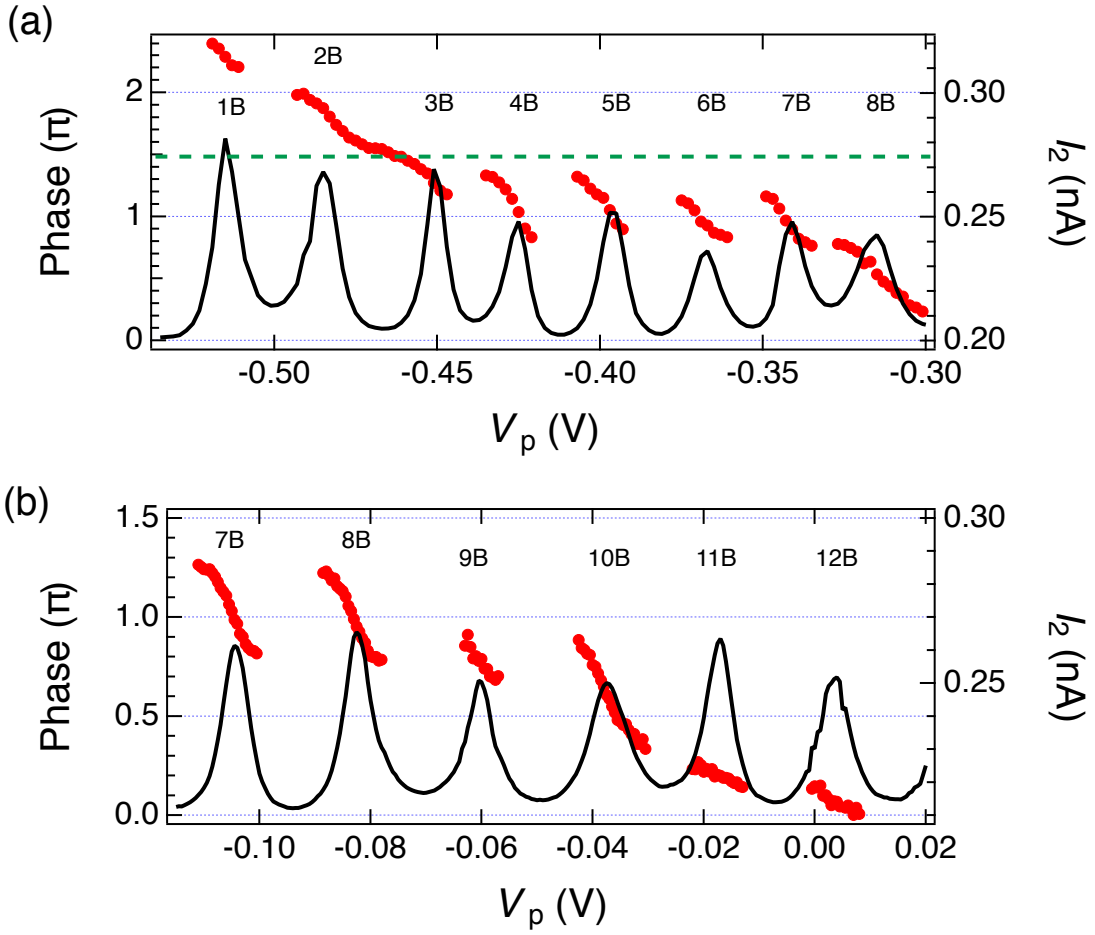

Fig. 6.3 The transmission phase (red circles and left axis) and the current (black line and right axis) as a function of the plunger gate voltage V_p in Region B for two different tuning conditions. In (a) the dashed line is added to emphasize the valley without the phase lapse.

Next we perform the phase measurement in Region B, which covers the region with more electrons than in Region A. The results are shown in Fig. 6.3, where the condition of the QD is changed between (a) and (b). In the condition of Fig. 6.3a Γ is estimated to be 0.23 to 0.31 meV and hence it is larger than δ ($\lesssim$ 0.2 meV). The valley without the phase lapse, a typical mesoscopic behavior, is still observed between the peak 2B and 3B. For the peaks 7B and 8B the phase behavior in the Kondo regime is observed.

To investigate the universal phase behavior in the region with even more electrons in

the QD, we tune the QD to reduce Γ and measure the phase (Fig. 6.3b). In this region U becomes small and hence we have to reduce Γ to observe a clear phase shift [1]. However especially for the peaks 11B and 12B we can not reduce Γ enough to measure a clear phase shift due to limited tunability of our QD. Therefore we can not measure the phase in the QD with a larger number of electrons than this region. Γ in the condition of Fig. 6.3 is estimated to be 0.16 to 0.24 meV. δ for the peaks 7B to 12B should be smaller than ≈ 0.2 meV for the peak 1B. Therefore Γ is considered to be larger than δ.

From Fig. 6.3b the phase seems to pile up between the peak 8B and 9B without a phase lapse. Although the phase shift across the peak 11B and 12B is very small, the total phase shift from the peak 7B to the peak 12B exceeds π, which suggests that our QD does not show the universal phase behavior but instead still maintains somewhat the mesoscopic behavior. As a result we do not find the universal phase behavior in our QD. This result is in contrast with previous reports [4], where the universal behavior appears with a smaller number ($\sim$14) of electrons in a QD whose dimension is a bit smaller than the one used in this work. According to theory, crossover from the mesoscopic to universal behavior can occur when the number of the electrons becomes large or Γ becomes much larger than δ. Our work shows that the mesoscopic behavior is still dominant in our QD even when the number of electrons is relatively large and Γ is slightly larger than δ. To achieve the universal behavior, we probably need to measure the phase with even larger QDs.

6.5 Phase lapse and Fano line shape

Finally in this section we focus on the asymmetric tail of CPs in FFT amplitude, which is related to Fano effect. We investigate the relation between the Fano line shape and the phase lapse. As discussed in section 5.6, the appearance of the phase lapse is connected to the orbital parity relation between nearby QD levels. The Fano effect is quantum interference between a discrete energy state and a continuous energy state [96]. It has been observed for an AB ring with a QD embedded into one of the two arms [97, 98] and a quantum wire with a side coupled QD [99]. They observed CPs having an asymmetric tail about the center of the peak as a signature of the Fano effect, and utilized the Fano interference to investigate the universal phase behavior in a large QD [95], where the in-phase behavior in the universal phase behavior is expected to produce asymmetric tails of the CPs on the same side. When the asymmetric tail is present on the opposite side between two neighboring

[1] When the tails of CPs overlap, the phase shift of π reflecting full occupation of one quantized level cannot be observed.

CPs, the orbital parity relation should be opposite between the two peaks and hence no phase lapse is expected in the valley between them.

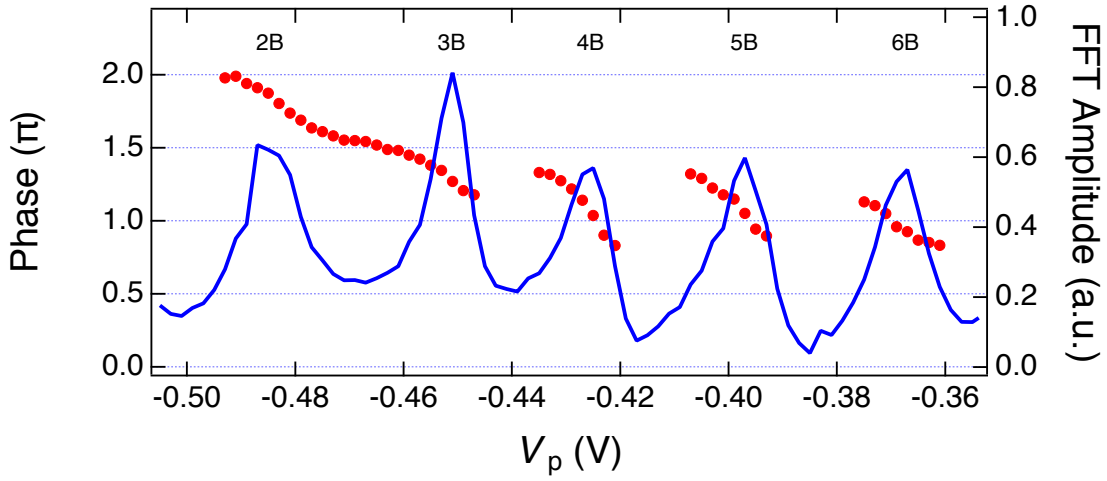

Fig. 6.4 The transmission phase and the FFT amplitude as a function of the plunger gate voltage V_p in Region B.

Fig. 6.4 shows the phase (red circles) and the FFT amplitude (blue curve) as a function of plunger gate voltage V_p. The phase data is the same as the one plotted in Fig. 6.3a. The current in Fig. 6.3a does not show any clear asymmetric feature but the FFT amplitude in Fig. 6.3 does. This may be because the current contains both coherent and in-coherent components, whereas the FFT amplitude only contains information about coherent electrons. Since the Fano effect is a coherent phenomenon, it is considered to appear more strongly in the FFT amplitude. On the other hand previous works [97] reported that an asymmetric tail of a Fano resonance is flipped by magnetic field. The FFT amplitude is averaged over the magnetic field and hence such an asymmetric feature is expected to be smoothed out. However it is also pointed out that the asymmetry can appear more strongly in one side when sweeping magnetic field [98]. In such a case the asymmetry is expected to remain in the FFT amplitude as observed in Fig. 6.4.

From the data in Fig. 6.4 the phase lapse appears between the peaks with the asymmetric tail on the same side, whereas in the valley between the peak 2B and 3B the asymmetry seems to be flipped and no phase lapse occurs as discussed above. This result suggests that the asymmetric Fano line shape is indeed related to the phase lapse as well as the orbital parity relation between nearby levels as discussed in the preceding experiment [95]. If so, we may also expect the quasi-universal behavior of the transmission phase in a larger QD, where a level strongly coupled to the leads determines the orbital parity of many successive

CPs [66, 67].

6.6 Summary and future plans

We investigated the transmission phase shift across a QD with a relatively large number of electrons. In particular the phase was investigated around the crossover from $\Gamma < \delta$ to $\Gamma > \delta$. We found that the transmission phase behaves in the same way as that of the mesoscopic regime in the crossover region. When Γ is smaller than δ, electron-transport is only mediated by a single level. The observed phase behavior could be simply understood from Friedel's sum rule and the orbital parity relation between nearby levels. On the other hand when Γ is larger than δ, more than two levels contribute to electron transport. The phase behavior becomes influenced by hybridization of multiple orbitals. But in our QD, we still observed the mesoscopic behavior of the phase even for $\Gamma > \delta$. Then as the QD is made larger to find the universal phase behavior predicted for $\Gamma \gg \delta$, at some point Γ/U becomes so large that neighboring CPs overlap, where a clear phase shift can not be observed. Indeed we could not find the universal phase behavior in the large QDs studied here. This result suggests that the universal phase behavior is not so robust as expected from previous experiments [3, 4]. We also found coincidence between the phase lapse and the Fano line shape. This result, combined with the previous experiment of the Fano line shape in a larger QD, suggests possibility of observing quasi-universal behavior of the phase for $\Gamma \gg \delta$. For a future plan, we would like to measure the transmission phase shift in a much larger QD, where Γ is much larger than δ, to confirm the quasi-universal behavior.

Chapter 7

Towards realization of single electron flying charge qubit using surface acoustic waves

7.1 Introduction

A flying qubit is in general implemented by an architecture, where a quantum state is controlled during transfer, and hence it should be suitable to create a non-local coherence or quantum entanglement, which is a key concept in quantum mechanics. Creation of the non-local entanglement can be confirmed by demonstrating the violation of Bell's inequality [100], which has been tested in various quantum systems [101–104]. In chapter 4 we have demonstrated the realization of an electron flying qubit with a two-path interferometer [76]. However the visibility of the qubit gate is as low as $\sim 10\%$, which is far below the value required for quantum operations with entanglement including quantum teleportation and violation of Bell's inequality. The visibility is limited by backscattering of electrons and existence of a few transmitting channels. Therefore it is important to prepare a highly coherent single transmitting channel without backscattering.

A surface acoustic wave (SAW) is a sound wave propagating near the surface of materials, which is generated by applying a radio frequency voltage on metallic gates deposited on the surface (see also section 2.6). In GaAs/AlGaAs 2DEG systems when we combine the potential of surface acoustic waves with that of a quantum wire, it is possible to make moving QDs and transfer an integer number of electrons in each potential minimum of the waves. As a result, a quantized current of $I = nef$ is observed, where n is an integer number,

e is an elementary charge and f is a SAW frequency. Initially this technique was developed to determine the value of e [33] in the field of quantum metrology. Recently the moving QDs have been used to investigate the dynamics of single electrons [105, 106] or to develop a single electron source and detector (see chapter 8) [25, 26] as important tools to perform quantum electron optical experiments [28, 30, 31].

Here we utilize this technique to make a single electron flying qubit architecture. We inject single electrons into a depleted AB ring with tunnel-coupled wires using SAWs to realize the flying qubit operations for single electrons. Since each single electron is transferred by large potentials of SAWs, it will not suffer from backscattering. Further more an electron being transferred through a depleted quantum wire should not be affected by electron-electron interactions, which is usually the main source of decoherence at low temperatures.

In this chapter we describe the control of single electrons injected by SAWs in a tunnel-coupled wire as a first step towards the full flying qubit operation. This demonstration also corresponds to a beam splitter operation for single flying electrons, which is a key technique for quantum electron optics using a SAW.

7.2 Device and measurement setup

The device is fabricated in a GaAs/AlGaAs heterostructure ($n = 1.35 \times 10^{11}$ cm^{-2}, $\mu = 1.5 \times 10^{6}$ cm^2/Vs at 4K) and fine structures are defined by surface Schottky gates. Fig.

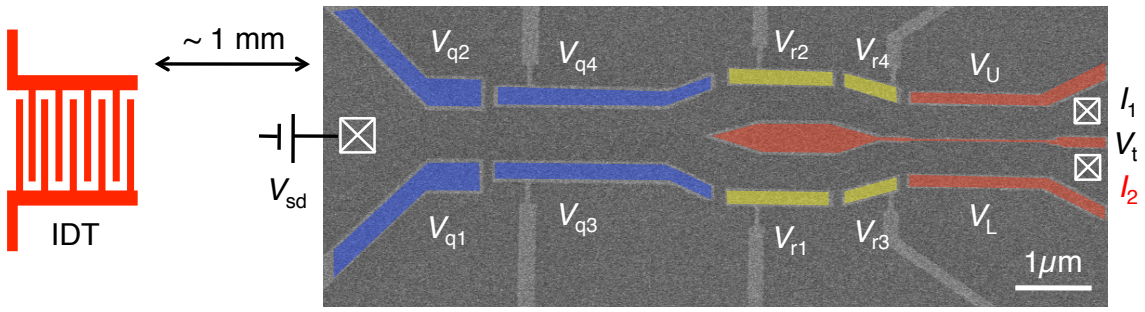

Fig. 7.1 SEM picture of the device and a schematic picture of the IDT.

7.1 shows the SEM image of the device and a schematic picture of an interdigital transducer (IDT). By applying appropriate voltages V_{q1}, V_{q2}, V_{q3} and V_{q4} to the four blue gates current through the gated channel is quantized. This channel is connected to an AB ring, and the current path to either the upper arm or the lower arm can be controlled by the voltages V_{r1},

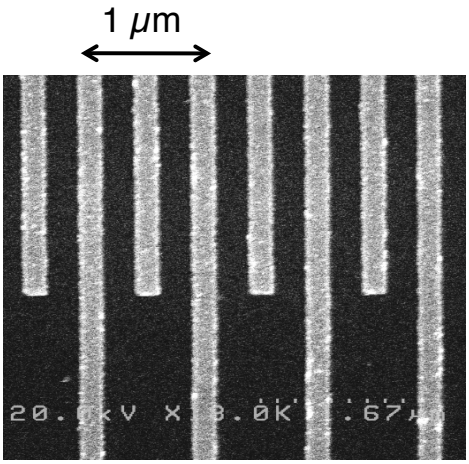

Fig. 7.2 SEM picture of the half wave length IDT.

V_{r2}, V_{r3} and V_{r4} applied to the four yellow gates. The output of the AB ring is connected to a tunnel-coupled wire which is defined by the voltages V_U, V_t and V_L applied to the three red gates. V_t mainly controls the tunnel-coupling energy between the two parts of the wire, whereas V_U and V_L mainly control the energy detuning between them. The IDT to generate SAWs is placed at about 1 mm apart from the fine structure. We employ the half wave length IDT as shown in Fig. 7.2, which is made of 100 pairs of metallic finger gates 60 μm in length and 250 nm in width with a 1 μm period. The IDT is orientated perpendicular to the direction of the 1D channel defined along the crystal axis [110] of the GaAs substrate.

The measurement in this section is performed in a He^3 refrigerator with the base temperature of ~ 0.3 K. A radio frequency voltage to generate SAWs is applied through a coaxial cable with a -13 dB loss at 2 to 3 GHz from the top of the fridge to the bottom at the device. All dc lines are electrically filtered out by a *RC*-filter ($R = 1\text{k}\Omega$, $C = 1\text{nF}$) at the base temperature. The output currents I_1 and I_2 of the tunnel-coupled wire are measured after conversion into voltages by current amplifiers at room temperature.

7.3 Current quantization in electron transport by surface acoustic waves

In this section we describe a quantized current transferred by SAWs through the quantum wire formed by the four blue gates in Fig. 7.1. For this measurement the upper right ohmic contact is floated and the current is measured between two terminals. Initially we check the

resonant frequency of the IDT. Fig. 7.3a shows the pinch off curve obtained by sweeping the voltages V_{q1} and V_{q2}. Then we set V_{q1} and V_{q2} to -0.96 V to suppress a normal dc current and applied the radio frequency (RF) voltage to the IDT to generate SAWs. We sweep the frequency to find the IDT resonance. The power of the RF voltage is set to be 5 dBm with duty cycle of 1/10 to avoid the device heating. A peak due to the resonance is observed at $f_0 = 2.6909$ GHz as shown in Fig. 7.3b. This value is consistent with the expected resonant frequency, i.e. sound velocity divided by the wavelength of the SAW defined by the period of the IDT (~ 2700 [m/s] /1 [μm] $= 2.7$ [GHz]). At the resonant frequency, SAWs generated in each finger of the IDT are in-phase and hence strong potential waves propagate through the device.

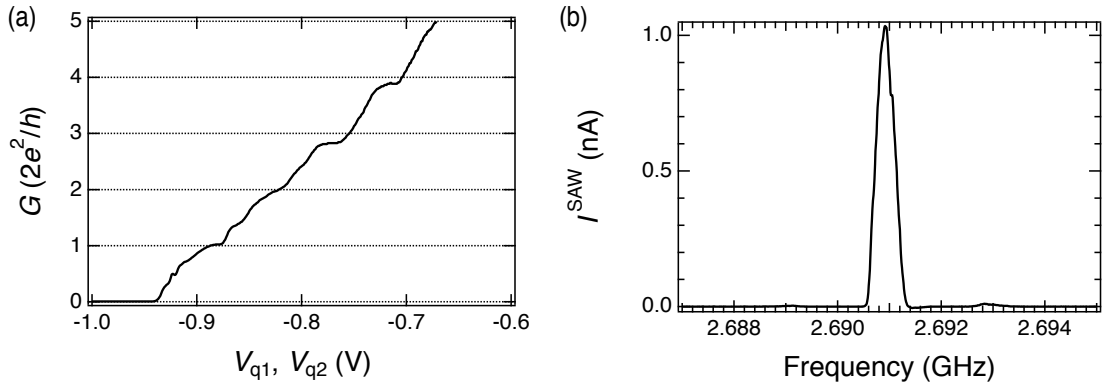

Fig. 7.3 (a) Pinch off curve when the gate voltages V_{q1} and V_{q2} are swept at the same time. The current observed in I_2 is converted into conductance by using the value of the bias voltage and the series resistance. (b) The current generated by SAWs as a function of the frequency of the RF voltage. The RF power of 5 dBm is applied with duty cycle of 1/10.

Next we use the four blue gates in Fig. 7.1 to observe the quantized currents. A normal dc current is suppressed by applying a more negative gate voltage than the channel pinch-off voltage. The frequency of the RF voltage is set to f_0 with the power of 15 dBm and the duty ratio of $1/20$ ($= 100$ [μs]$/2000$ [μs]). While a normal dc current is suppressed, the current transferred by SAWs is observed. Fig. 7.4 shows the SAW current as a function of the gate voltage V_{q4}. A clear plateau structure appears at around the value of nef_0, where n is an integer and e is an elementary charge [33]. Here the potential of SAWs and the quantum wire form moving QDs. The number of electrons inside the moving QDs are quantized due to strong Coulomb interactions in the narrow confinement. At the n-th plateau n electrons are included in each minimum of SAWs and transferred across the quantum wire. For the higher plateau ($n \geq 3$) the value becomes lower than nef_0. This is because charging energy,

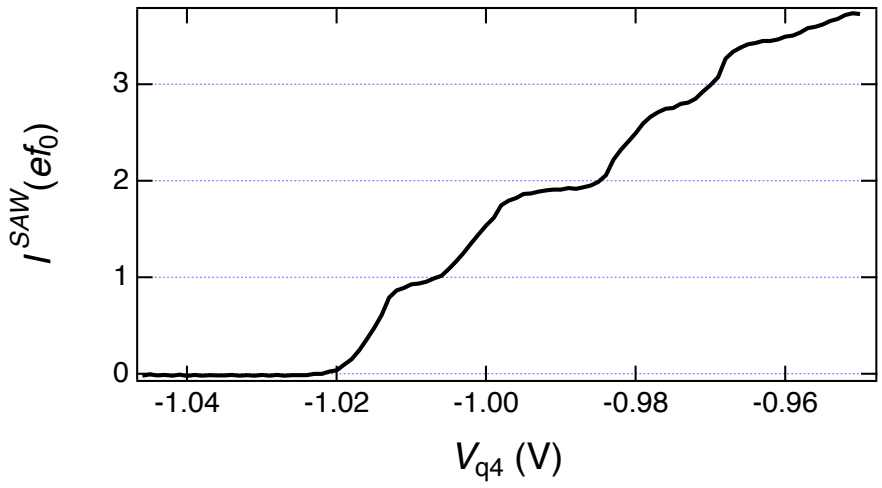

Fig. 7.4 The current transferred by SAWs I^{SAW} as a function of the gate voltage V_{q5}. I^{SAW} is scaled in a unit of ef_0, where e is an elementary charge and $f_0 = 2.6909$ GHz is the resonant frequency of the IDT.

which determines the stability of the plateau, is smaller for the larger QDs. For the smaller charging energy more error events can occur during the quantization process, and reduce the observed current. When we set the gate voltage at the first plateau ($I^{\mathrm{SAW}} = ef_0$), single electrons can be injected continuously. We use this technique in the following experiment.

In this device it is necessary to use the four blue gates (see Fig. 7.1) to establish the potential profile required to observe nice quantized currents. This is because the power of the SAW is not large enough to transfer quantized currents defined by the first (left) two gates. Note that the number of electrons at each moving QD is determined by the competition between the potential slope defined by the gate voltage and the amplitude of the potential generated by the SAW. When we try to quantize the SAW current with only the first two gates, potential slope at the entrance becomes so large that we need more amplitude of the SAW potential, which is not accessible in our setup.

7.4 Control of single electrons transferred by surface acoustic waves in a tunnel-coupled wire

Here we control single electrons transferred by SAW-induced moving QDs in a depleted tunnel-coupled wire. When we define a pseudo spin by the presence of an electron at either part of the wire, tunneling of an electron between the two parts is equivalent to rotation of

the flying qubit state in the Bloch sphere (Fig. 4.2b) as discussed in chapter 4. For zero energy detuning between the two parts of the tunnel-coupled wire the qubit state is rotated about the X-axis in the Bloch sphere. When the detuning is not zero, the rotation axis tilts to the Z-axis in the XZ-plane, which in principle allows us to achieve an arbitrary qubit state in the Bloch sphere. In this section we also modulate the energy detuning to confirm a coherent electron oscillation in a tunnel-coupled wire. We measure a different device from the one used in the experiment described in section 7.3 but with the same design.

For the measurement we control the gate voltages V_{q1}, V_{q2}, V_{q3} and V_{q4} to inject electrons one by one into the tunnel-coupled wire formed by the gate voltages V_U, V_t and V_L. The injection of single electrons into the tunnel-coupled wire is controlled by the gate voltages V_{r1}, V_{r2}, V_{r3} and V_{r4}. The resonant frequency f_0 of the IDT is found to be 2.704 GHz for

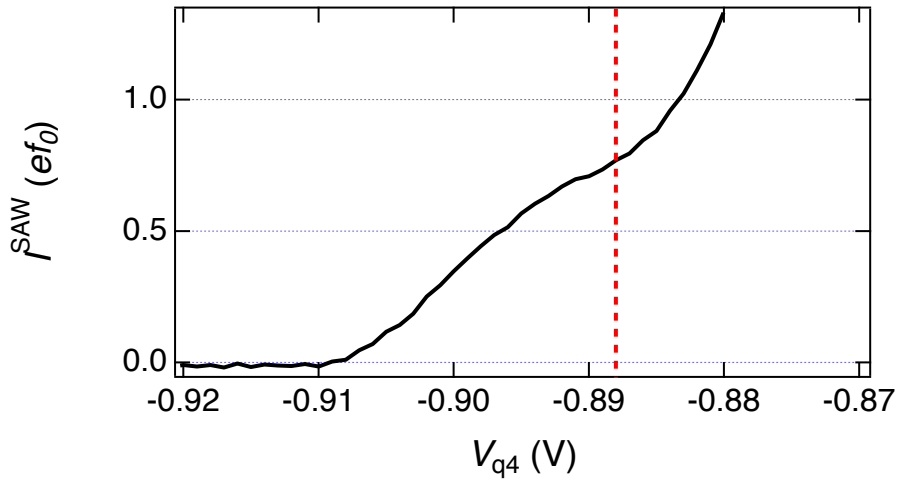

Fig. 7.5 Tuning of injected electrons to the tunnel-coupled wire. The SAW current I^{SAW} is plotted as a function of the voltage V_{q4}. The plotted current is sum of the current I_1 and I_2. The current is shown in a unit of ef_0. The dashed line indicate the gate voltage we set in the following experiment.

this device. The power of the RF voltage is set to 16 dBm and the duty cycle is set to 1/20 (=100 [μs]/2000 [μs]).

Fig. 7.5 shows the current transferred by SAWs as a function of V_{q4}, where a normal dc current was pinched off. Compared to the data in Fig. 7.4, the plateau is less flat and the value of the current is lower than ef_0. At the gate condition in Fig. 7.5 all the gate voltages in Fig. 7.1 are applied to form the whole structure for this experiment. In such a condition more RF power is required to generate SAW currents compared to the situation where only the four gate voltages V_{q1}, V_{q2}, V_{q3} and V_{q4} to control the quantized current are applied. On the other hand 16 dBm is the maximum power we can apply in our setup. Therefore when

we improve the setup and apply more RF power to the IDT, we expect to see a better plateau. However in Fig. 7.5 the first plateau can still be resolved, and therefore we set the voltage V_{q4} to the value at the dashed line in Fig. 7.5. Here the current smaller than ef_0 ensures that each minimum of the SAWs contains either zero or one electron.

We apply large negative voltages V_{r2} and V_{r4} to prevent single electrons injected from the upper side, whereas we apply less negative voltages V_{r1} and V_{r3}, which are just enough to form an one dimensional channel. As a result single electrons are injected only from the lower part of the tunnel-coupled wire.

Before showing the experimental results, we discuss the expected output current in the following. Here single electrons are transferred being confined in moving double QDs formed by the potential of the SAWs and the tunnel-coupled wire. Hamiltonian of the system can be written in terms of the pseudo spin notation used in section 4.3 (See also Fig. 4.2) as follows:

$$H = \varepsilon_{\uparrow} |\uparrow\rangle \langle\uparrow| + \varepsilon_{\downarrow} |\downarrow\rangle \langle\downarrow| - \tau(|\downarrow\rangle \langle\uparrow| + |\uparrow\rangle \langle\downarrow|), \tag{7.1}$$

where $\varepsilon_{\uparrow(\downarrow)}$ is the confinement energy of the upper (lower) QD and τ is the tunnel-coupling energy between the two QDs. The eigenstate and eigenenergy of the Hamiltonian are

$$|\psi_{\pm}\rangle = \frac{\tau}{\sqrt{\tau^2 + (\Delta\varepsilon \mp \sqrt{\Delta\varepsilon^2 + \tau^2})^2}} \left[|\uparrow\rangle + \frac{\Delta\varepsilon \mp \sqrt{\Delta\varepsilon^2 + \tau^2}}{\tau} |\downarrow\rangle \right] \tag{7.2}$$

$$E_{\pm} = \frac{\varepsilon_{\uparrow} + \varepsilon_{\downarrow}}{2} \pm \sqrt{\Delta\varepsilon^2 + \tau^2}, \tag{7.3}$$

where $\Delta\varepsilon$ is defined by $\frac{\varepsilon_{\uparrow} - \varepsilon_{\downarrow}}{2}$. Corresponding unitary operation can be written by

$$\begin{aligned} U_{\mathrm{T}}(\theta) &= \left[\cos\left(\frac{\theta}{2}\right) - \frac{i\Delta\varepsilon}{\sqrt{\Delta\varepsilon^2 + \tau^2}} \sin\left(\frac{\theta}{2}\right) \right] |\uparrow\rangle \langle\uparrow| \\ &+ \left[\cos\left(\frac{\theta}{2}\right) + \frac{i\Delta\varepsilon}{\sqrt{\Delta\varepsilon^2 + \tau^2}} \sin\left(\frac{\theta}{2}\right) \right] |\downarrow\rangle \langle\downarrow| \\ &+ \frac{i\tau}{\sqrt{\Delta\varepsilon^2 + \tau^2}} \sin\left(\frac{\theta}{2}\right) [|\uparrow\rangle \langle\downarrow| + |\downarrow\rangle \langle\uparrow|] \end{aligned} \tag{7.4}$$

$$\theta = \frac{2\sqrt{\Delta\varepsilon^2 + \tau^2}}{\hbar} \cdot t_0 \,, \tag{7.5}$$

where $t_0 = L/v_{\mathrm{SAW}}$ is the traveling time of a moving double QD through a tunnel-coupled wire. In this experiment t_0 is estimated to be about 0.74 [ns] (2 [μm]/2700 [m/s]).

In the experiment single electrons are injected only from the lower part of the tunnel-coupled wire and hence the initial state is $|\downarrow\rangle$. When we adopt the above unitary operation to $|\downarrow\rangle$, the final state in the tunnel-coupled wire becomes

$$\begin{aligned} U_{\mathrm{T}}(\theta)\,|\downarrow\rangle &= \frac{i\tau}{\sqrt{\Delta\varepsilon^2+\tau^2}}\sin\left(\frac{\theta}{2}\right)|\uparrow\rangle \\ &+ \left[\cos\left(\frac{\theta}{2}\right)+\frac{i\Delta\varepsilon}{\sqrt{\Delta\varepsilon^2+\tau^2}}\sin\left(\frac{\theta}{2}\right)\right]|\downarrow\rangle\,. \end{aligned} \tag{7.6}$$

Then the output currents I_1 and I_2 should be

$$\begin{aligned} I_1 &= |\langle\uparrow|U_{\mathrm{T}}(\theta)|\downarrow\rangle|^2\cdot I_0^{\mathrm{SAW}} \\ &= \frac{\tau^2}{\Delta\varepsilon^2+\tau^2}\cdot\left(\frac{1-\cos\theta}{2}\right)\cdot I_0^{\mathrm{SAW}} \end{aligned} \tag{7.7}$$

$$\begin{aligned} I_2 &= |\langle\downarrow|U_{\mathrm{T}}(\theta)|\downarrow\rangle|^2\cdot I_0^{\mathrm{SAW}} \\ &= \left[1-\frac{\tau^2}{\Delta\varepsilon^2+\tau^2}\cdot\left(\frac{1-\cos\theta}{2}\right)\right]\cdot I_0^{\mathrm{SAW}}, \end{aligned} \tag{7.8}$$

where $I_0^{\mathrm{SAW}}(\lesssim ef_0)$ is the injected current by SAWs. From Fig. 7.5 I_0^{SAW} is about $0.77ef_0$ in our measurement. $\Delta\varepsilon$ and τ are controlled by V_{U}, V_{t} and V_{L} in the experiment and oscillations of the currents I_1 and I_2 are observed.

First we deplete the tunnel-coupled wire and modulate τ while keeping $\Delta\varepsilon$ equal to zero. At the zero energy detuning the normalized output current $T_{1(2)} = I_{1(2)}/(I_1+I_2) = I_{1(2)}/I_0^{\mathrm{SAW}}$ is

$$T_{1(2)} = \frac{1\mp\cos\theta}{2}\,, \tag{7.9}$$

where $\theta = \frac{2\tau t_0}{\hbar}$ is proportional to τ. The normalized current $T_{1(2)}$ as a function of V_{U}, V_{t} and V_{L} is plotted in Fig. 7.6. From the right to the left V_{t} is swept to the negative direction, whereas V_{U} and V_{L} are swept to the positive, to keep the width of the wire constant while reducing the tunnel-coupling energy τ. At the left for sufficiently negative V_{t}, the two parts of the wire are totally decoupled by depleting a region underneath the center tunnel-coupling gate and hence all electrons injected from the lower part of the wire are observed in the lower contact at the right. By increasing the tunnel-coupling energy τ to the right of Fig. 7.6, the normalized currents oscillate in anti-phase as expected from Eq. 7.9. Since the peaks and dips appears at $\theta = n\pi$, where n is an integer, τ can be estimated at the peaks and dips using the expression of $\tau = \frac{\theta\hbar}{2t_0}$ as shown in Fig. 7.6. Note that τ does not change linearly with

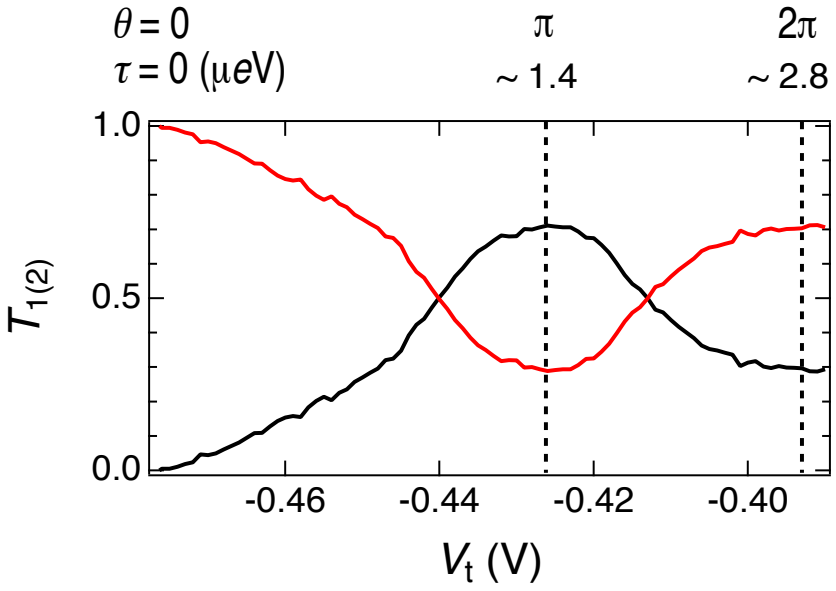

Fig. 7.6 Normalized current T_1 (black curve) and T_2 (red curve) as a function of V_t. V_U, V_L are also swept along the lateral axis to keep the width of the wire constant (see text). θ and τ at the peak position is written in the upper side.

the gate voltages along the lateral axis because τ depends on the details of the confinement potential, which is generally not proportional to the gate voltages. At the right of Fig. 7.6 the 2DEG underneath the center tunnel-coupling gate starts to open, and the current flowing directly between the two contacts in the right side prevents measurements for larger τ. The visibility of the oscillation defined by $|(I_1 - I_2)/(I_1 + I_2)|$ at $\theta = \pi/2$ is calculated to be about 40%, which is much larger than that for ballistic electrons shown in Fig. 4.4 since the pseudo spin state is operated at a single transmitting channel at each part of the wire without backscattering.

At zero energy detuning we observe the SAW current oscillation with a relatively high visibility and assign it to quantum oscillation of an electron. However since we modulate the three gate voltages at the same time, it would also be possible to explain the feature in Fig. 7.6 by a classical picture in terms of balance of the conductance between the two parts of the wire. To exclude this possibility, we measure the current oscillation at finite energy detunings and try to confirm the coherent electron tunneling from Eq. 7.7, 7.8. The energy detuning $\Delta\varepsilon$ is induced by increasing $(V_U - V_L)$ from the zero detuning condition at each V_t.

Fig. 7.7 shows the normalized current T_1 plotted in the plane of V_t or tunnel-coupling energy τ along the lateral axis and $\Delta V_U - \Delta V_L$ or the energy detuning $\Delta\varepsilon$ along the vertical axis. Only the oscillating component is plotted to show the feature clearly. Around the zero

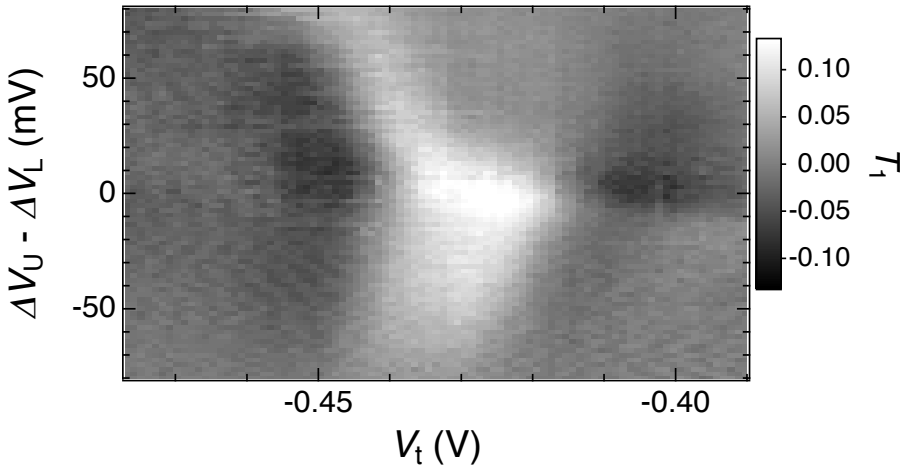

Fig. 7.7 Normalized current T_1 plotted in the plane of V_U, V_t, V_L and $(\Delta V_U - \Delta V_L)$. $\Delta V_{U(L)}$ is shift of gate voltage from zero detuning condition at each V_t. ΔV_U and ΔV_L are symmetrically moved to opposite direction in 1 mV step from zero detuning. The smoothed background current is subtracted from the raw data to show the feature clearly.

detuning a large oscillation with a longer period along the lateral axis is observed. As $|\Delta\varepsilon|$ increased, the oscillation amplitude becomes smaller and the period becomes shorter. This behavior is indeed expected from Eq. 7.7. The oscillation amplitude should be proportional to $\frac{\tau^2}{\Delta\varepsilon^2+\tau^2}$ and the period should be proportional to $\frac{d\tau}{d\theta} = \frac{\hbar\sqrt{1+(\Delta\varepsilon/\tau)^2}}{2t_0}$.

Although the observed tendency is consistent with the expectation from Eq. 7.7, the observed pattern in Fig. 7.7 and the expected one in Fig. 7.8 do not perfectly coincide. Several reasons are considered for this discrepancy. Firstly the tunnel-coupling energy and the energy detuning are modulated by the gate voltages in this experiment. However generally the relation between them is not linear and hence the axis of Fig. 7.7 and 7.8 should be non-linearly scaled. Secondly although the 2DEG in the tunnel-coupled wire is depleted around the zero energy detuning, at the detuning away from $\Delta\varepsilon = 0$ the 2DEG can be recovered in either of the two parts, which would also change the situation from the calculation because gate voltages become less effective due to the screening. Nonetheless of importance is that the expected feature for the coherent electron oscillation in the amplitude as well as the period as shown in Fig. 7.8 is successfully observed in Fig. 7.7.

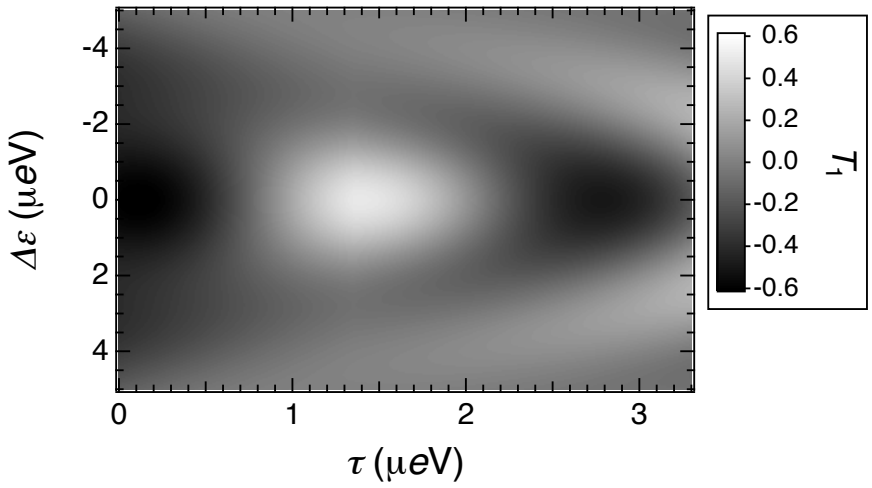

Fig. 7.8 Normalized current T_1 plotted in the plane of a tunnel-coupling energy τ and an energy detuning $\Delta\varepsilon$ calculated from Eq. 7.7. A smoothed subtracted current is subtracted from the bare current to only show the oscillating component for comparison with the experimental data in Fig. 7.7.

Finally we measure the SAW current oscillation around zero energy detuning at different temperatures (Fig. 7.9). In Fig. 7.9a the observed oscillation is slightly different between the base temperature and the higher temperature. However the oscillation amplitude itself is unchanged. To compare the oscillation amplitude precisely, a smoothed background current is subtracted from the raw data and the oscillating component is extracted as shown in Fig. 7.9b. The oscillation amplitude is almost equivalent between the base temperature and the high temperature ($\sim$ 1.9K). This result suggests that decoherence sources which depend on the temperature such as electron-electron interaction and electron-phonon interaction do not play an important role in limiting the visibility of the observed oscillations ($\sim$ 40%). Since single electrons are transferred through the depleted wire by moving QDs, suppression of an electron-electron interaction can be simply understood. When an electron is confined into a QD, phonons with smaller energy than energy separation of quantized levels in the QD do not play a role. Further more an electron confined into a smaller space couples with a smaller number of phonons. A SAW induced moving QD has a stronger confinement than a standard static QD so that it has a larger energy spacing in the quantized levels and a more confined wave function. Therefore an electron in the moving QD is less affected by phonons. Also different from the static QD, the influence of phonons is averaged during transport of the moving QD, which may also reduce the phonon induced decoherence.

The possible reasons for the limited visibility are as follows. In this experimental setup

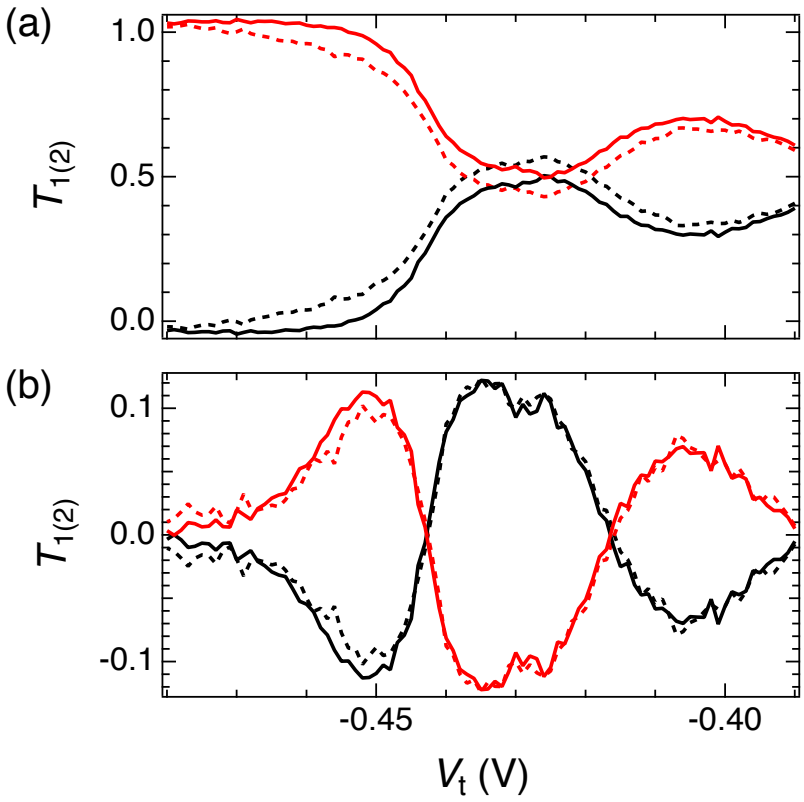

Fig. 7.9 Normalized currents T_1 (black curve) and T_2 (red curve) as a function of the gates V_U, V_t and V_L at two different temperatures. The solid line is measured at the base temperature (~ 0.3K) and the dashed line is measured at about 1.9K. (a) Raw data. (b) Oscillation parts extracted by subtracting smoothed background from the raw data.

due to the limitation of the SAW power the 2DEG at the entrance of the tunnel-coupled wire may not be fully depleted when electrons are injected into the depleted tunnel-coupled wire. Therefore single electrons are picked up from the 2DEG at the entrance (lower arm of the AB ring) and enter the tunnel-coupled wire. After this process an electron state in the moving QD can become a superposition of eigenstates with different energy levels which have different tunnel-coupling strengths. This lowers the visibility of the oscillation. Another possibility is that again due to the limitation of the setup the parameter range we can access is relatively narrow. As a result the tuning of the potential in the tunnel-coupled wire might not be good enough and a finite energy detuning might be left at some parts of the wire even at the zero energy detuning where we obtain the maximum visibility of the oscillation.

To improve the visibility further, improvement of the setup to apply stronger SAWs to the device is first required. This could be done by changing the material of the coaxial lines for the RF voltages or by revising the design of the IDT. It should make the tunable range wider and allow to deplete the whole structure to realize a smooth potential profile.

7.5 Summary and future plans

We performed the control of single electrons transferred by SAWs in a depleted tunnel-coupled wire. We successfully observed an oscillation of single electrons as a function of tunnel-coupling energy. At finite energy detuning the amplitude of the oscillation becomes weaker and the period becomes shorter compared to the case of zero energy detuning. This feature is expected for a coherent electron oscillation. The visibility obtained at zero energy detuning is about 40%, which is much higher than the one for ballistic electrons as show in section 4.3. Finally the measurement at two different temperatures revealed the robustness of the oscillation against electron-electron interaction and electron-phonon interaction. When we define pseudo spins by the presence of an electron at either part of the tunnel-coupled wire, the transport electron can be considered as a flying qubit and the observed electron oscillation corresponds to rotation of the qubit state.

The next step of the present study should be realization of a full qubit operation with two independent rotation axes in an AB ring with a tunnel-coupled wire. Also improvement of the visibility should be an important step modifying the experimental setup and the device geometry. Once a high visibility flying qubit is realized, it will be realistic to generate the non-local entanglement state and to confirm it by observing violation of Bell's inequality in the scheme proposed theoretically [5].

Further more the electron control in the tunnel-coupled wire achieved here corresponds to be a beam spitter operation for single electrons, which is a key component to perform electron quantum optical experiments [28, 30, 31] using a SAW. When this technique is combined with the single electron source and detector [25, 26], experiments to study the quantum nature of electrons at the single electron level and by single shot measurement will be within experimental reach.

Chapter 8

Single electron transfer between distant quantum dots using a surface acoustic wave

8.1 Introduction

Quantum electron optics [27–31] attracts particular interests since it is considered to be a promising candidate to construct scalable quantum systems. In contrast with photons, electrons are strongly interacting particles and they usually propagate in a Fermi sea filled with other electrons. Each electron therefore inevitably mixes with the others of the Fermi sea, which implies that the quantum information stored within the charge or the spin of the single electron will be lost over short lengths. To perform quantum electron-optical experiments at the single-electron level, one therefore needs a source of single electrons, a controlled propagating medium and a single-electron detector. It has been proposed that edge states in the quantum Hall effect can serve as a one-dimensional (1D) propagating channel for flying electrons. As a result of Coulomb blockade, QDs have been demonstrated to be a good source of single electrons [85, 107] and can also serve as a single-electron detector. Indeed, once an electron has been stored in a QD, its presence can be inferred routinely by charge detection [108]. Nevertheless, re-trapping the electron in another quantum dot after propagation in an edge state turns out to be extremely difficult, and currently all the information extracted from such experiments is coming from ensemble measurements [31, 80, 81]. Here we show that a single flying electron can be sent on demand from a QD by means of a 1D

quantum channel and re-trapped in a second QD after propagation [1] [25, 26]. The 1D quantum channel consists of a depleted region several micrometers long in a 2DEG. The electron is dragged along by exciting a SAW and propagates isolated from the other electrons inside the 1D channel [74]. The processes of loading and unloading of the flying electron from the quantum channel into a QD turn out to be highly efficient. Moreover, we show that the transfer of the electron can be triggered with a timescale shorter than the coherence time T_2^* of GaAs spin qubits [22]. Because both electron spin directions are treated on the same foot in the SAW quantum channel, one expects that the spin coherence during the transport is conserved. Naturally, new possibilities will emerge to address the question of scalability in spin qubit systems [21, 22, 109].

8.2 Device and measurement setup

The device is defined by Schottky gates in an AlGaAs/GaAs 2DEG-based heterostructure (the properties of the 2DEG are as follows: $\mu \approx 10^6 \mathrm{cm}^2/\mathrm{Vs}$, $n_\mathrm{s} \approx 1.4 \times 10^{11} \mathrm{cm}^{-2}$, depth 125 nm) with standard split-gate techniques (Fig. 8.1). The charge configuration of both dots is measured by means of the conductance of both QPCs [108] by biasing it with a direct-current voltage of 300 μV; the current is measured with a current-to-voltage converter with a bandwidth of 1.4 kHz. The voltage on each gate can be varied on a timescale down to microseconds. In addition, the gate biased with voltage V_c, controlling the coupling between the left dot and the 1D channel, is connected to a homemade bias tee to allow nanosecond manipulation of the dot potential by means of an arbitrary function generator (Tektronix AWG 5014). The IDT, which is place about 2mm to the left of the sample, is made of 70 pairs of lines 70 μm in length and 250 nm in width with a 1-μm spacing. The IDT is orientated perpendicular to the direction of the 1D channel defined along the crystal axis [110] of the GaAs wafer; it has a frequency bandwidth of about 20 MHz. By applying a microwave burst 65 ns long on the IDT, a train of about 150 moving QDs is created in the 1D channel.

[1] The experiments presented in this chapter has been achieved by a close collaboration with the group in Grenoble. The measurements and analysis were performed by Sylvain Hermelin *et al.* in Grenoble. We designed and fabricated the device, and performed early states of the experiment in Japan.

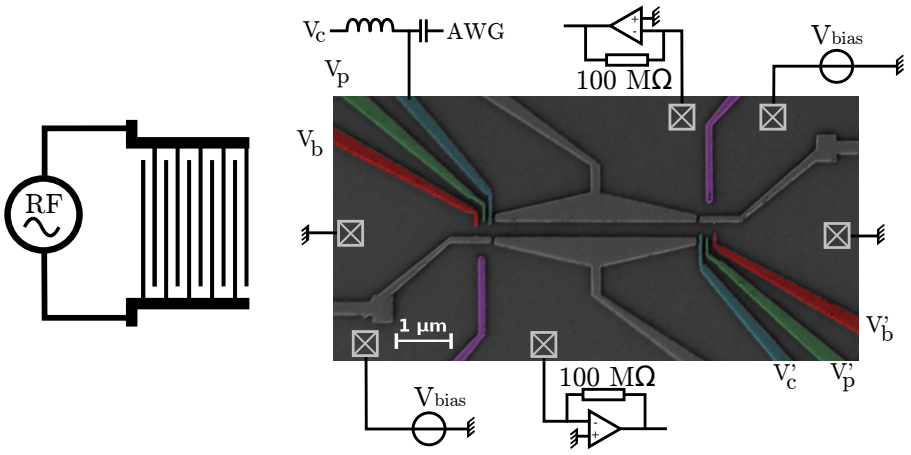

Fig. 8.1 SEM image of the single-electron transfer device, and diagram of the experimental setup. Two quantum dots, which can be brought into the single-electron regime, are separated by a 1D channel 3 μm long, as shown.

8.3 Single electron transfer between distant QDs

To transport a single electron from one QD to the other separated by a 3-μm 1D channel (see Fig. 8.1), the following procedure is applied. First, the region between the two electrodes, which define the 1D channel, is fully depleted. As a consequence, direct linear electron transport from one end of the channel to the other is blocked because the Fermi energy lies below the potential induced by the gates. Second, by applying microwave excitation to the IDT, SAW-induced moving QDs are generated [74] as a result of the piezoelectric properties of GaAs. By adding a QD to each side of the 1D channel and tuning both QDs into the single electron regime, it is then possible to transport a single electron from one QD across the 1D channel and catch it inside the second QD. Stability diagrams for both QDs as a function of the applied voltage on the two gates controlling the two barriers of the QD are shown in Fig. 8.2a, b. They demonstrate that the system can be tuned into a regime consisting of few electrons. As expected, the charge degeneracy lines disappear when the barrier height between each dot and the reservoir is increased (corresponding to increasingly negative voltages V_b and $V_{b'}$). This also changes the position of the QD minimum and brings the electron closer to the 1D channel, to a position where a better transfer to SAW QDs is expected.

The protocol of the single-electron source for a SAW quantum channel is a sequence made of three dot-gate voltage steps (see Fig. 8.2a). At working point A on Fig. 8.2a, the left QD (the single-electron source) is loaded with one electron on a timescale close to

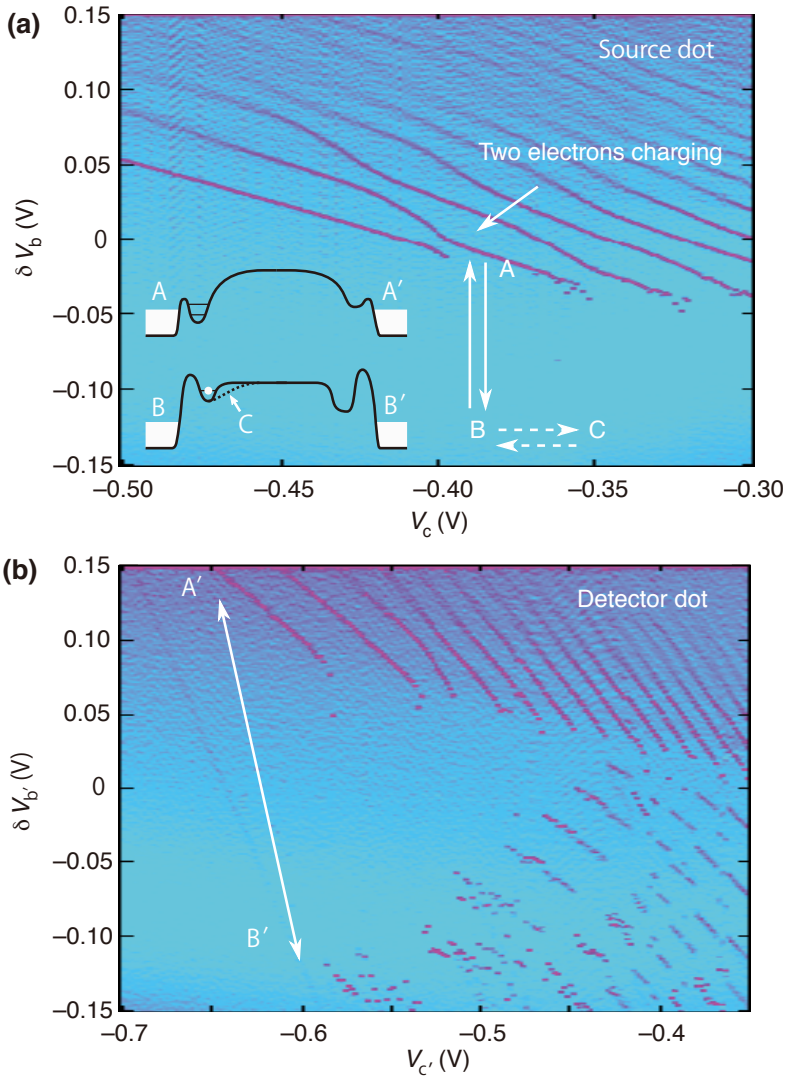

Fig. 8.2 (a), (b) Stability diagram of the left (a) and right (b) dot obtained via charge detection by varying respectively gate voltages (V_b or V_c) and ($V_{b'}$ or $V_{c'}$) (see Fig. 8.1). Sweeps in V_b and $V_{b'}$ are fast and are performed within 1s from +0.15 V to -0.15 V (3 ms per point). When the barrier height is made higher (V_b or $V_{b'}$ more negative), metastable charge states with timescales longer than the V_b or $V_{b'}$ sweep time are observed. In the very negative $V_{b'}$ part of the diagram for the right dot, the electrons will finally tunnel out. When the sweep direction of $V_{b'}$ is reversed, these charge detection steps are absent. Inset to (a): schematic diagram of the dots and channel electrostatic potential applied by the gates to the electron at different points in the stability diagram (see text).

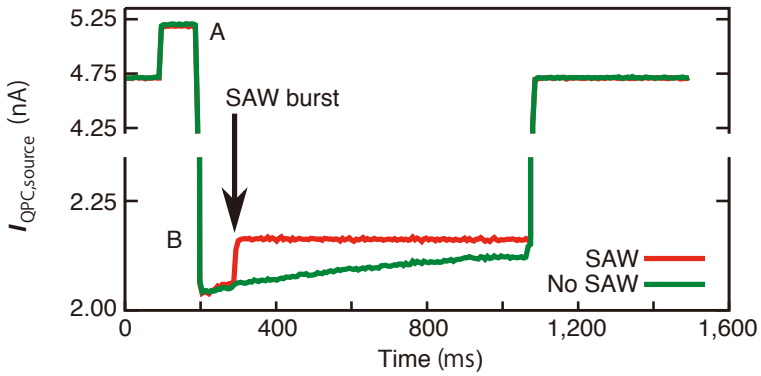

Fig. 8.3 Average QPC time trace along the voltage sequence of the single-electron source. Without the microwave burst applied on the IDT, we observe a lifetime for the metastable one-electron charge state of 700 ms. Applying a microwave burst, the electron in the metastable state is forced to quit the quantum dot with very high probability.

microseconds and unresolved with the setup detection bandwidth. It is then brought rapidly to working point B, where the chemical potential of the single electron state lies above the Fermi energy and the coupling to the 1D channel is expected to be large. The actual position of B is not crucial as long as the electron is sufficiently protected from tunneling out of the dot and the dot potential is high enough to facilitate the charging of the electron into the moving SAW dot (see inset to Fig. 8.2a). For each sequence, the QPC conductance time-trace is recorded to observe single-shot loading and unloading of the dot. This sequence is repeated 1,000 times to obtain measurement statistics; the resulting averaged time-trace are shown in Fig. 8.3. An exponential decay of the presence of the electron in the dot as a function of the time spent at working point B is observed in the experimental data, corresponding to a tunneling time close to 1s as indicated by the green line. This gate pulsing sequence is then repeated by adding a burst of microwaves to the IDT with a pulse length of several tens of nanoseconds, applied 100 ms after the system is brought into position B. The microwave burst creates a moving QD, which lifts the electron, initially trapped in the left QD, above the tunnel barrier and drags it out of the QD. This results in a jump in the QPC current, as shown by the red line.

To demonstrate that the electron has been loaded into a moving QD and not expelled into the reservoir, it is essential to detect the coincidence between events when the electron leaves the single-electron source (left dot) and when it is trapped in the single-electron detector (right dot). This is realized by a second voltage pulse sequence on the right dot: when the single-electron source is brought in position B, the detector dot is armed by pulsing

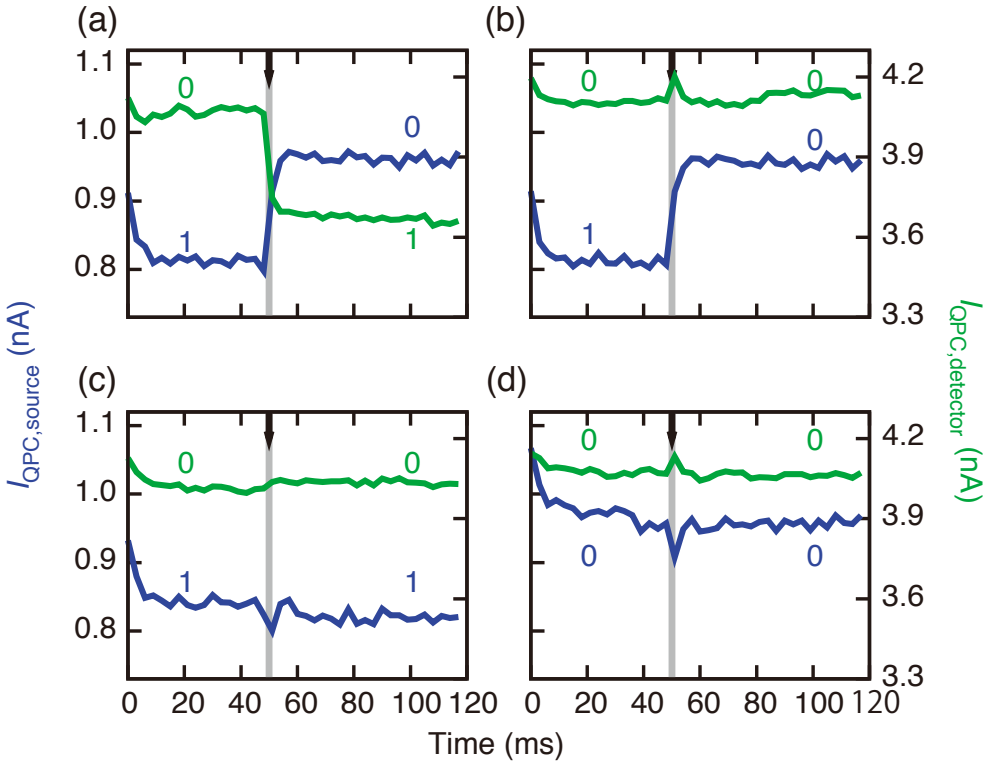

Fig. 8.4 (a)-(d) Coincidence between the two single-shot QPC time traces at voltage working points B and B′ corresponding to the different events N_{1001} (a), N_{1000} (b), N_{1100} (c) and N_{0000} (d). The position in time of the RF burst is indicated by the black arrow. At this specific time, the small peak or dip observed on time traces is the result of the SAW-induced enhancement or reduction, respectively, of the QPC current. The notation $N_{\alpha\beta\gamma\delta}$ corresponds to the number of events with α or β electrons in the source dot before or after the microwave burst, respectively, and to γ or δ electrons in the receiver dot before or after the microwave burst, respectively. Event N_{1000} corresponds to the situation in which the electron has been transferred from the source to the detector and is immediately kicked out of the detector dot by the same RF burst and is therefore not detected. Events for which $\beta + \delta > \alpha + \gamma$ are called 'bad' events.

its gate to working point B′, where the steady state is the zero-electron state and the coupling to the channel is large. At this working point both QPC traces are recorded simultaneously. No charge variation is observed during the first 50 ms where the system is kept in position B. A microwave pulse is sent with a time lag of 50 ms. After the recording, the detector is reinitialized to zero electron at working point A′, where the captured electron can tunnel efficiently into the reservoir. Typical single-shot readout curves are presented in Fig. 8.4a-d. Coincidences are observed between events when an electron leaves the source QD and an electron is detected in the receiver QD within the same time slot (Fig. 8.4a). These events correspond to the situation in which one electron has been loaded in the electron source (left dot), is then transferred in the quantum channel (the moving QDs) and is received in the detector (right dot). In contrast with photon detectors, here the electron still exists after detection. A set of experiments described in Fig. 8.4 allows the full characterization of the high quantum efficiency of both the single-electron source and the single-electron detector observed in the experiment: 96% for the single-electron source and 92% for the single-electron detector (see Table. 8.1).

Table 8.1 Summary table for the different events over 10,001 traces for different source dot loading probabilities (N_{1xxx}) with or without the RF burst. When an index of N is replaced by x, the corresponding output result is disregarded. The loading probability can be tuned on demand by changing the voltage gate position A in the stability diagram around the charge degeneracy point. The summation at the bottom table is for $(\beta+\alpha) > (\delta+\gamma)$.

	SAW				
Event	On	Off	On	On	On
N_{1xxx}	9,841	10,001	16	5,154	1,462
N_{10xx}	9,408 (95.6%)	0 (0%)	15 (94%)	4,954 (96.1%)	1395 (95.4%)
N_{100x}	9,128	0	14	4,807	1,349
N_{1001}	8,393 (91.9%)	0 (0%)	14 (100%)	4,417 (91.9%)	1,244 (92.2%)
$\Sigma N_{\alpha\beta\gamma\delta}$	0	1	0	0	0

8.4 Two electron transfer between distant QDs

In QDs it is possible to load not just one but two electrons. By waiting long enough [110], the two electrons will be in a singlet state at zero magnetic field and are hence entangled in the spin degree of freedom. The ability to separate the two electrons and to bring only one of them to the second QD is of potential interest for the transfer of quantum information and is the essence of the quantum teleportation protocol [111–113]. By analogy with photons, this is the equivalence of a two-photon entangled source [114]. Moreover, in contrast with a photon detector, the electron detector can discriminate easily whether one, two or more electrons have left the single-electron source and are captured in the single-electron detector (see Fig. 8.2a). The protocol consists of loading the left dot with exactly two electrons by moving gate voltages V_b and V_c into the two-electron regime of the stability diagram. The quantum dot is then tuned towards the working point where loading of the moving QDs is possible (point B). Different possibilities for the emission of electrons into the quantum channel are observed. Indeed, when starting with exactly two electrons in the source dot, one can achieve the outcome that either exactly one or both electrons are emitted from the source and received in the detector dot, as shown by the single-shot traces for QPC detection of the two dots (see Fig. 8.5a-d). The probability of each event varies with the working voltage at point B. For very negative gate voltage V_c, about half of the time the two electrons are separated, meaning that only one electron is transferred, and the other half of the time both electrons are transported (see Table 8.2). For the events in which both electrons leave the dot, the electrons are most probably loaded into two different moving QDs. More interestingly, when pulsing gate voltage V_c more positively, a situation can be realized in which only one of the two electrons of the left dot is efficiently emitted and consequently captured by the right dot (see Table 8.2). In this case, the probability of sending the two electrons is markedly reduced, to less than 3%, and the probability of effectively separating the two electrons approaches 90%.

8.5 Measurement of time scale of single electron transfer

To use single-electron transfer in quantum operations using spin qubits, one has to show that coherence of the electron spin after electron transfer is preserved. Measurement and coherent manipulations of electron spins can be straightforwardly implemented in our setup, and the spin coherence time T_2^* of an ensemble of electrons stored in SAW-assisted moving QDs has been shown to be as long as 25 ns (ref. [71]). A necessary condition for investigating co-

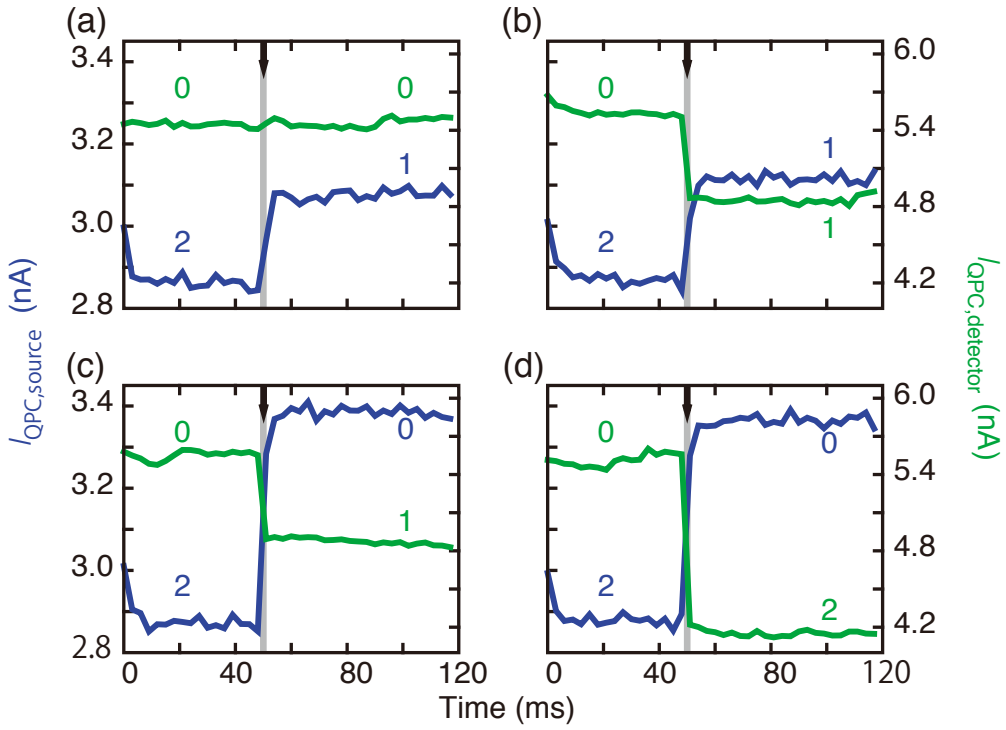

Fig. 8.5 (a)-(d) Coincidence between the two single-shot QPC time traces at voltage working points B and B′ corresponding to the different events N_{2100} (a), N_{2101} (b), N_{2001} (c) and N_{2002} (d).

Table 8.2 Summary table for the different events over 1,005 traces for dot configurations $V_c = -0.388$ V and $V_c = -0.322$ V.

	V_c (mV)	
Event	−388	−322
N_{21xx}	445 (44.3%)	970 (96.5%)
N_{2101}	443 (99.6%)	878 (90.5%)
N_{20xx}	558 (55.5%)	30 (3%)
N_{2001}	62 (11%)	4 (13%)
N_{2002}	496 (88.9%)	26 (87%)

herent transport of a single electron spin is to be able to trigger the electron transfer within a timescale that is short compared with T_2^*. Indeed, a microwave pulse 250 ns in duration corresponds to about 700 moving QDs, and the experiments described above demonstrate the ability to load the electron into one of the moving QDs produced by each SAW microwave burst. We now show that the number of minima of the microwave burst in which the electron is loaded can be reduced to two. For this purpose, the single-electron source voltage sequence is slightly modified. After charging of the quantum dot, the system is brought to position B (see Fig. 8.2a) slightly on the more negative side with respect to V_c, and the duration of the microwave pulse is shortened to a minimum of 65 ns. At this voltage position, the barrier height to the quantum channel is increased and the transfer probability of an electron into the quantum channel is as low as 5% when excited with the SAW microwave burst. To trigger single-electron transfer, a 1-ns voltage pulse on V_c with a positive value (voltage position C in Fig. 8.2a) is added to this sequence. In Fig. 8.6a the evolution of the number of events in which one electron leaves the single-electron source and one electron is detected in the single-electron detector (N_{1001}) is plotted as a function of the delay between the 1-ns gate pulse and the 65-ns microwave burst. High transfer probabilities reaching 90% are observed only for time delays of roughly 765 ns, corresponding to the propagation time

of the SAW from the IDT to the dot region. Taking into account the pulse length of the gate and the distance between two minima of the SAW, only two moving quantum dots can then be the hosts of the transported electron during the gate pulse, as indicated schematically in Fig. 8.6b. This demonstrates the ability to load on demand and in a very reproducible manner one of the two minima of the train of moving QDs with a single electron during the 1-ns gate pulse. The use of a faster arbitrary waveform generator should allow the electron to be loaded on demand into the same moving QD.

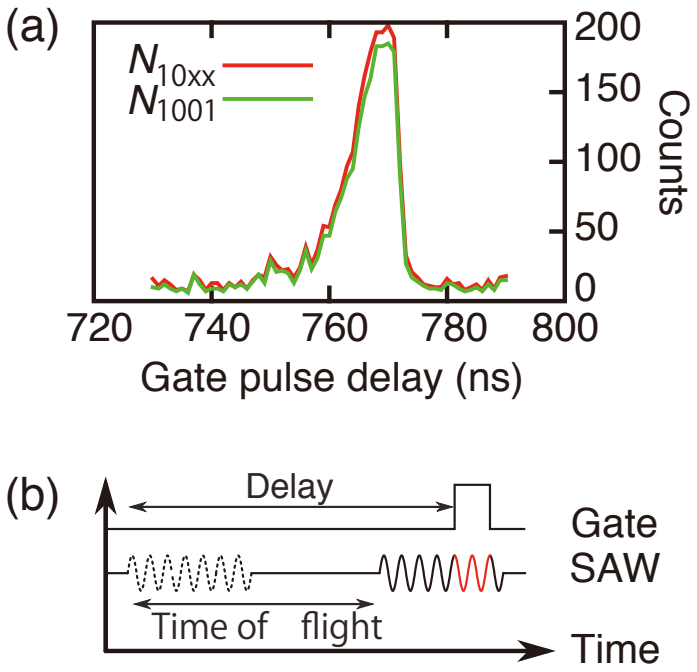

Fig. 8.6 (a) Evolution of the number of N_{1001} and N_{10xx} events as a function of the delay between the 1-ns gate pulse and the 65-ns microwave burst when a single electron is loaded into the single-electron source. (b) Schematic diagram of the timing sequence between the 1-ns gate pulse and the microwave burst applied to the IDT.

8.6 Summary and future prospects

The experiments performed here represent the first milestone on the road to a new experimental platform for realizing quantum optics with flying electrons implemented in gated 2DEG heterostructures and transported by SAWs. High quantum efficiency of both the single-electron detector and the single-electron source are shown and potentially enable the

measurement of all moments of the electron correlations [115]. In comparison with other implementations in similar systems, the propagating electron is physically isolated from the other conduction electrons of the heterostructure. In bringing together two propagating quantum buses separated by a tunnel barrier, a beam splitter for flying electrons can be implemented (see also chapter 7) [19, 20] and Hanbury Brown and Twiss-type experiments in which there are stronger Coulomb interactions between electrons could be realized. Future experiments should allow coherent spin transfer and provide new insight into the feasibility of quantum teleportation protocols and on the potential scalability of spin qubits.

List of Publications

[1] Sylvain Hermelin, Shintaro Takada, Michihisa Yamamoto, Seigo Tarucha, Andreas D Wieck, Laurent Saminadayar, Christopher Bäuerle, and Tristan Meunier. Electrons surfing on a sound wave as a platform for quantum optics with flying electrons. Nature, 477(7365):435–8, Sep 2011. doi: 10.1038/nature10416.

[2] Michihisa Yamamoto, Shintaro Takada, Christopher Bäuerle, Kenta Watanabe, Andreas D Wieck, and Seigo Tarucha. Electrical control of a solid-state flying qubit. Nature Nanotech., 7(4):247–51, 2012. doi: 10.1038/nnano.2012.28.

[3] Michihisa Yamamoto, Shintaro Takada, Seigo Tarucha, Sylvain Hermelin, Christopher Bäuerle, and Tristan Meunier. Single electron transfer using surface acoustic wave: towards quantum optics with flying electrons. KOTAIBUTSURI, 47(4):163–169, April 2012.

[4] S. Hermelin, S. Takada, M. Yamamoto, S. Tarucha, A. D. Wieck, L. Saminadayar, C. Bäuerle, and T. Meunier. Fast and efficient single electron transfer between distant quantum dots. Journal of Applied Physics, 113:136508, Apr 2013.

[5] Michihisa Yamamoto, Shintaro Takada, and Seigo Tarucha. Quantum Information Transfer over a Long Distance and Attempts for Quantum Electron Optics. BUTSURI, 68(5):288, MAY 2013.

[6] S. Takada, C. Bäuerle, M. Yamamoto, S. Hermelin, T. Meunier, A. Alex, A. Weichselbaum, J. von Delft, A. D. Wieck, and S. Tarucha. Transmission phase in the Kondo regime revealed in a two-path interferometer. arXiv, 11 2013. URL `http://arxiv.org/abs/1311.6884`.

[7] Tobias Bautze, Christoph Süssmeier, Shintaro Takada, Christoph Groth, Tristan Meunier, Michihisa Yamamoto, Seigo Tarucha, Xavier Waintal, and Christopher Bäuerle.

From numerical to real experiments: a study of a solid state implementation of a flying qubit. arXiv, 12 2013. URL http://arxiv.org/abs/1312.5194.

[8] A. Aharony, S. Takada, O. Entin-Wohlman, M. Yamamoto, and S. Tarucha. Aharonov-Bohm interferometry with a tunnel-coupled wire. arXiv, 12 2013. URL http://arxiv.org/abs/1312.5177.

References

[1] P. Nozières. A "Fermi-Liquid" Description of the Kondo Problem at Low Temperatures. Journal of Low Temperature Physics, 17(1-2):31–42, 1974. doi: 10.1007/BF00654541.

[2] Ulrich Gerland, Jan von Delft, T. A. Costi, and Yuval Oreg. Transmission Phase Shift of a Quantum Dot with Kondo Correlations. Phys. Rev. Lett., 84(16):3710–3713, Apr 2000. doi: 10.1103/PhysRevLett.84.3710.

[3] R. Schuster, E. Buks, M. Heiblum, D. Mahalu, V. Umansky, and H. Shtrikman. Phase measurement in a quantum dot via a double-slit interference experiment. Nature, 385: 417–420, Jan 1997.

[4] M. Avinun-Kalish, M. Heiblum, O. Zarchin, D. Mahalu, and V. Umansky. Crossover from 'mesoscopic' to 'universal' phase for electron transmission in quantum dots. Nature, 436:529–533, June 2005.

[5] Radu Ionicioiu, Paolo Zanardi, and Fausto Rossi. Testing Bell's inequality with ballistic electrons in semiconductors. Phys. Rev. A, 63(5):050101, Apr 2001. doi: 10.1103/PhysRevA.63.050101.

[6] M. Büttiker. Four-Terminal Phase-Coherent Conductance. Phys. Rev. Lett., 57(14): 1761–1764, Oct 1986. doi: 10.1103/PhysRevLett.57.1761.

[7] M. Büttiker. Symmetry of electrical conduction. IBM J. Res. Dev., 32:317, 1988.

[8] A. Yacoby, M. Heiblum, D. Mahalu, and Hadas Shtrikman. Coherence and Phase Sensitive Measurements in a Quantum Dot. Phys. Rev. Lett., 74(20):4047–4050, May 1995. doi: 10.1103/PhysRevLett.74.4047.

[9] M. Sigrist, A. Fuhrer, T. Ihn, K. Ensslin, S. E. Ulloa, W. Wegscheider, and M. Bichler. Magnetic-Field-Dependent Transmission Phase of a Double-Dot System in a Quantum Ring. Phys. Rev. Lett., 93:066802, Aug 2004. doi: 10.1103/PhysRevLett.93.066802. URL `http://link.aps.org/doi/10.1103/PhysRevLett.93.066802`.

[10] Sven S. Buchholz, Saskia F. Fischer, Ulrich Kunze, Matthew Bell, Dirk Reuter, and Andreas D. Wieck. Control of the transmission phase in an asymmetric four-terminal Aharonov-Bohm interferometer. Phys. Rev. B, 82(4):045432, Jul 2010. doi: 10.1103/PhysRevB.82.045432.

[11] A. Yacoby, R. Schuster, and M. Heiblum. Phase rigidity and h/2e oscillations in a single-ring Aharonov-Bohm experiment. Phys. Rev. B, 53(15):9583–9586, Apr 1996. doi: 10.1103/PhysRevB.53.9583.

[12] Yang Ji, M. Heiblum, D. Sprinzak, D. Mahalu, and Hadas Shtrikman. Phase Evolution in a Kondo-Correlated System. Science, 290:779–783, Oct 2000.

[13] M. Zaffalon, Aveek Bid, M. Heiblum, D. Mahalu, and V. Umansky. Transmission Phase of a Singly Occupied Quantum Dot in the Kondo Regime. Phys. Rev. Lett., 100(22):226601, Jun 2008. doi: 10.1103/PhysRevLett.100.226601.

[14] A. Levy Yeyati and M. Büttiker. Aharonov-Bohm oscillations in a mesoscopic ring with a quantum dot. Phys. Rev. B, 52(20):R14360–R14363, Nov 1995. doi: 10.1103/PhysRevB.52.R14360.

[15] T. Hecht, A. Weichselbaum, Y. Oreg, and J. von Delft. Interplay of mesoscopic and Kondo effects for transmission amplitude of few-level quantum dots. Phys. Rev. B, 80:115330, Sep 2009. doi: 10.1103/PhysRevB.80.115330. URL http://link.aps.org/doi/10.1103/PhysRevB.80.115330.

[16] O. Entin-Wohlman, A. Aharony, Y. Imry, Y. Levinson, and A. Schiller. Broken Unitarity and Phase Measurements in Aharonov-Bohm Interferometers. Phys. Rev. Lett., 88:166801, Apr 2002. doi: 10.1103/PhysRevLett.88.166801. URL http://link.aps.org/doi/10.1103/PhysRevLett.88.166801.

[17] Amnon Aharony and Ora Entin-Wohlman. Measuring the Kondo effect in the Aharonov-Bohm interferometer. Phys. Rev. B, 72:073311, Aug 2005. doi: 10.1103/PhysRevB.72.073311. URL http://link.aps.org/doi/10.1103/PhysRevB.72.073311.

[18] Pascal Simon, O. Entin-Wohlman, and A. Aharony. Flux-dependent Kondo temperature in an Aharonov-Bohm interferometer with an in-line quantum dot. Phys. Rev. B, 72:245313, Dec 2005. doi: 10.1103/PhysRevB.72.245313. URL http://link.aps.org/doi/10.1103/PhysRevB.72.245313.

[19] Jesús A. del Alamo and Cristopher C. Eugster. Quantum fieldâĂŘeffect directional coupler. Applied Physics Letters, 56(1):78–80, Oct 1990. doi: http://dx.doi.org/10.1063/1.102657. URL http://scitation.aip.org/content/aip/journal/apl/56/1/10.1063/1.102657.

[20] N. Tsukada, A. D. Wieck, and K. Ploog. Proposal of novel electron wave coupled devices. Appl.Phys.lett., 56:2527, 1990.

[21] F. H. L. Koppens, C. Buizert, K. J. Tielrooij, I. T. Vink, K. C. Nowack, T. Meunier, L. P. Kouwenhoven, and L. M. K. Vandersypen. Driven coherent oscillations of a single electron spin in a quantum dot. Nature, 442:766, Aug 2006.

[22] J. R. Petta, A. C. Johnson, J. M. Taylor, E. A. Laird, A. Yacoby, M. D. Lukin, C. M. Marcus, M. P. Hanson, and A. C. Gossard. Coherent Manipulation of Electron Spins in Semiconductor Quantum Dots. Science, 309:2180, 2005.

[23] M. Pioro-Ladriere, T. Obata, Y. Tokura, Y. S. Shin, T. Kubo, K. Yoshida, T. Taniyama, and S. Tarucha. Electrically driven single-electron spin resonance in a slanting Zeeman field. Nature. Phys., 4:776, Oct 2008.

[24] T. Hayashi, T. Fujisawa, H. D. Cheong, Y. H. Jeong, and Y. Hirayama. Coherent Manipulation of Electronic States in a Double Quantum Dot. Phys. Rev. Lett., 91 (22):226804, Nov 2003.

[25] Sylvain Hermelin, Shintaro Takada, Michihisa Yamamoto, Seigo Tarucha, Andreas D Wieck, Laurent Saminadayar, Christopher Bäuerle, and Tristan Meunier. Electrons surfing on a sound wave as a platform for quantum optics with flying electrons. Nature, 477(7365):435–8, Sep 2011. doi: 10.1038/nature10416.

[26] R. P. G. McNeil, M. Kataoka, C. J. B. Ford, C. H. W. Barnes, D. Anderson, G. A. C. Jones, I. Farrer, and D. A. Ritchie. On-demand single-electron transfer between distant quantum dots. Nature, 477:439–442, Sep 2011.

[27] R. C. Liu, B. Odom, Y. Yamamoto, and S. Tarucha. Quantum interference in electron collision. Nature, 391(6664):263–265, 01 1998. URL http://dx.doi.org/10.1038/34611.

[28] William D. Oliver, Jungsang Kim, Robert C. Liu, and Yoshihisa Yamamoto. Hanbury Brown and Twiss-Type Experiment with Electrons. Science, 284(5412):299–301, 1999. doi: 10.1126/science.284.5412.299. URL http://www.sciencemag.org/content/284/5412/299.abstract.

[29] M. Henny, S. Oberholzer, C. Strunk, T. Heinzel, K. Ensslin, M. Holland, and C. Schönenberger. The Fermionic Hanbury Brown and Twiss Experiment. Science, 284 (5412):296–298, 1999. doi: 10.1126/science.284.5412.296. URL http://www.sciencemag.org/content/284/5412/296.abstract.

[30] I. Neder, N. Ofek, Y. Chung, M. Heiblum, D. Mahalu, and V. Umansky. Interference between two indistinguishable electrons from independent sources. Nature, 448 (7151):333–337, 07 2007. URL http://dx.doi.org/10.1038/nature05955.

[31] E. Bocquillon, V. Freulon, J.-M Berroir, P. Degiovanni, B. Plaçais, A. Cavanna, Y. Jin, and G. Fève. Coherence and Indistinguishability of Single Electrons Emitted by Independent Sources. Science, 339(6123):1054–1057, Mar 2013. doi: 10.1126/science.1232572. URL http://www.sciencemag.org/content/339/6123/1054.abstract.

[32] H.-W. Lee. Generic Transmission Zeros and In-Phase Resonances in Time-Reversal Symmetric Single Channel Transport. Phys. Rev. Lett., 82(11):2358–2361, Mar 1999. doi: 10.1103/PhysRevLett.82.2358.

[33] J M Shilton, V I Talyanskii, M Pepper, D A Ritchie, J E F Frost, C J B Ford, C G Smith, and G A C Jones. High-frequency single-electron transport in a quasi-one-dimensional GaAs channel induced by surface acoustic waves. Journal of Physics: Condensed Matter, 8(38):L531, 1996. URL http://stacks.iop.org/0953-8984/8/i=38/a=001.

[34] B. J. van Wees, H. van Houten, C. W. J. Beenakker, J. G. Williamson, L. P. Kouwenhoven, D. van der Marel, and C. T. Foxon. Quantized conductance of point contacts in a two-dimensional electron gas. Phys. Rev. Lett., 60(9):848–850, Feb 1988. doi: 10.1103/PhysRevLett.60.848.

[35] D. A. Wharam, T. J. Thornton, R. Newbury, M. Pepper, H. Ahmed, J. E. F. Frost, D. G. Hasko, D. C. Peacock, D. A. Ritchie, and G. A. C. Jones. One-dimensional transport and the quantisation of the ballistic resistance. J. PHys. C, 21:L209, 1988.

[36] Suprio Datta. Electronic Transport in Mesoscopic Systems. CAMBRIDGE UNIVERSITY PRESS, 1995.

[37] S. Katsumoto. Mesoscopic systems. Asakura, Feb 2003.

[38] Lars Onsager. Reciprocal Relations in Irreversible Processes. I. Phys. Rev., 37:405–426, Feb 1931. doi: 10.1103/PhysRev.37.405. URL `http://link.aps.org/doi/10.1103/PhysRev.37.405`.

[39] Lars Onsager. Reciprocal Relations in Irreversible Processes. II. Phys. Rev., 38:2265–2279, Dec 1931. doi: 10.1103/PhysRev.38.2265. URL `http://link.aps.org/doi/10.1103/PhysRev.38.2265`.

[40] H. B. G. Casimir. On Onsager's Principle of Microscopic Reversibility. Rev. Mod. Phys., 17:343–350, Apr 1945. doi: 10.1103/RevModPhys.17.343. URL `http://link.aps.org/doi/10.1103/RevModPhys.17.343`.

[41] Y. Aharonov and D. Bohm. Significance of Electromagnetic Potentials in the Quantum Theory. Phys. Rev., 115(3):485–491, Aug 1959. doi: 10.1103/PhysRev.115.485.

[42] R. A. Webb and S. Washburn. QUANTUM INTERFERENCE FLUCTUATIONS IN DISORDERED METALS. Physics Today, 41:46, Dec 1988.

[43] Akira Tonomura, Tsuyoshi Matsuda, Ryo Suzuki, Akira Fukuhara, Nobuyuki Osakabe, Hiroshi Umezaki, Junji Endo, Kohsei Shinagawa, Yutaka Sugita, and Hideo Fujiwara. Observation of Aharonov-Bohm Effect by Electron Holography. Phys. Rev. Lett., 48(21):1443–1446, May 1982. doi: 10.1103/PhysRevLett.48.1443.

[44] S. Washburn and R. A. Webb. Quantum transport in small disordered samples from the diffusive to the ballistic regime. Rep. Prog. Phys., 55:1311–1383, 1992.

[45] A. G. Huibers, M. Switkes, C. M. Marcus, K. Campman, and A. C. Gossard. Dephasing in Open Quantum Dots. Phys. Rev. Lett., 81(1):200–203, Jul 1998. doi: 10.1103/PhysRevLett.81.200.

[46] A. E. Hansen, A. Kristensen, S. Pedersen, C. B. Sørensen, and P. E. Lindelof. Mesoscopic decoherence in Aharonov-Bohm rings. Phys. Rev. B, 64(4):045327, Jul 2001. doi: 10.1103/PhysRevB.64.045327.

[47] K. Kobayashi, H. Aikawa, S. Katsumoto, and Y. Iye. Probe-Configuration-Dependent Decoherence in an Aharonov-Bohm Ring. J. Phys. Soc. Jpn., 71(9):2094–2097, SEPTEMBER 2002.

[48] Georg Seelig and Markus Büttiker. Charge-fluctuation-induced dephasing in a gated mesoscopic interferometer. Phys. Rev. B, 64(24):245313, Dec 2001. doi: 10.1103/PhysRevB.64.245313.

[49] G. Seelig, S. Pilgram, A. N. Jordan, and M. Büttiker. Probe-configuration-dependent dephasing in a mesoscopic interferometer. Phys. Rev. B, 68(16):161310, Oct 2003. doi: 10.1103/PhysRevB.68.161310.

[50] M. Jung, K. Hirakawa, Y. Kawaguchi, S. Komiyama, S. Ishida, and Y. Arakawa. Lateral electron transport through single self-assembled InAs quantum dots. Applied Physics Letters, 86(3):033106, 2005. doi: http://dx.doi.org/10.1063/1.1853516. URL http://scitation.aip.org/content/aip/journal/apl/86/3/10.1063/1.1853516.

[51] Tarucha, Austing, Honda, van der Hage RJ, and Kouwenhoven. Shell Filling and Spin Effects in a Few Electron Quantum Dot. Phys Rev Lett, 77(17):3613–3616, Oct 1996.

[52] M. Ciorga, A. S. Sachrajda, P. Hawrylak, C. Gould, P. Zawadzki, S. Jullian, Y. Feng, and Z. Wasilewski. Addition spectrum of a lateral dot from Coulomb and spin-blockade spectroscopy. Phys. Rev. B, 61(24):R16315, June 2000.

[53] K. Ono, D. G. Austing, Y. Tokura, and S. Tarucha. Current Rectification by Pauli Exclusion in a Weakly Coupled Double Quantum Dot System. Science, 297(5585): 1313–1317, 2002. doi: 10.1126/science.1070958. URL http://www.sciencemag.org/content/297/5585/1313.abstract.

[54] E. Buks, R. Schuster, M. Heiblum, D. Mahalu, and V. Umansky. Dephasing in electron interference by a 'which-path' detector. Nature, 391:871–874, FEBRUARY 1998.

[55] Daniel Loss and David P. DiVincenzo. Quantum computation with quantum dots. Phys. Rev. A, 57:120–126, Jan 1998. doi: 10.1103/PhysRevA.57.120. URL http://link.aps.org/doi/10.1103/PhysRevA.57.120.

[56] L P Kouwenhoven, D G Austing, and S Tarucha. Few-electron quantum dots. Reports on Progress in Physics, 64(6):701, 2001. URL http://stacks.iop.org/0034-4885/64/i=6/a=201.

[57] R. Hanson, L. P. Kouwenhoven, J. R. Petta, S. Tarucha, and L. M. K. Vandersypen. Spins in few-electron quantum dots. Rev . Mod . Phys ., 79:1217, Oct 2007.

[58] Jun Kondo. Resistance Minimum in Dilute Magnetic Alloys. Progress of Theoretical Physics, 32(1):37–49, 1964. doi: 10.1143/PTP.32.37. URL http://ptp.ipap.jp/link?PTP/32/37/.

[59] D. Goldhaber-Gordon, Hadas Shtrikman, D. Mahalu, David Abusch-Magder, U. Meirav, and M. A. Kastner. Kondo effect in a single-electron transistor. Nature, 391:156–159, Jan 1998.

[60] S. M. Cronenwett, T. H. Oostrkamp, and L. P. Kouwenhoven. A Tunable Kondo Effect in Quantum Dots. Science, 281:540, July 1998.

[61] W. G. van der Wiel, S. De Franceschi, T. Fujisawa, J. M. Elzerman, S. Tarucha, and L. P. Kouwenhoven. The Kondo Effect in the Unitary Limit. Science, 289(5487): 2105–8, Sep 2000.

[62] Sasaki, De Franceschi S, Elzerman, van der Wiel WG, Eto, Tarucha, and Kouwenhoven. Kondo effect in an integer-spin quantum dot. Nature, 405(6788):764–7, Jun 2000. doi: 10.1038/35015509.

[63] S. Sasaki, S. Amaha, N. Asakawa, M. Eto, and S. Tarucha. Enhanced Kondo Effect via Tuned Orbital Degeneracy in a Spin $1/2$ Artificial Atom. Phys. Rev. Lett., 93: 017205, Jul 2004. doi: 10.1103/PhysRevLett.93.017205. URL http://link.aps.org/doi/10.1103/PhysRevLett.93.017205.

[64] Pablo Jarillo-Herrero, Jing Kong, Herre S J van der Zant, Cees Dekker, Leo P Kouwenhoven, and Silvano De Franceschi. Orbital Kondo effect in carbon nanotubes. Nature, 434(7032):484–8, Mar 2005. doi: 10.1038/nature03422.

[65] A. Levy Yeyati and M. Büttiker. Scattering phases in quantum dots: An analysis based on lattice models. Phys. Rev. B, 62:7307–7315, Sep 2000. doi: 10.1103/PhysRevB.62.7307. URL http://link.aps.org/doi/10.1103/PhysRevB.62.7307.

[66] P. G. Silvestrov and Y. Imry. Towards an Explanation of the Mesoscopic Double-Slit Experiment: A New Model for Charging of a Quantum Dot. Phys. Rev. Lett., 85(12): 2565–2568, Sep 2000. doi: 10.1103/PhysRevLett.85.2565.

[67] C. Karrasch, T. Hecht, A. Weichselbaum, Y. Oreg, J. von Delft, and V. Meden. Mesoscopic to Universal Crossover of the Transmission Phase of Multilevel Quantum Dots. Phys. Rev. Lett., 98:186802, 2007.

[68] Reinhard Baltin and Yuval Gefen. An Approximate Sign Sum Rule for the Transmission Amplitude through a Quantum Dot. Phys. Rev. Lett., 83(24):5094–5097, Dec 1999.

[69] R. Baltin, Y. Gefen, G. Hackenbroich, and H.A. Weidenmüller. Correlations of conductance peaks and transmission phases in deformed quantum dots. The European Physical Journal B - Condensed Matter and Complex Systems, 10(1):119–129, 1999. ISSN 1434-6028. doi: 10.1007/s100510050835. URL http://dx.doi.org/10.1007/s100510050835.

[70] Rafael A. Molina, Rodolfo A. Jalabert, Dietmar Weinmann, and Philippe Jacquod. Scattering Phase of Quantum Dots: Emergence of Universal Behavior. Phys. Rev. Lett., 108:076803, Feb 2012. doi: 10.1103/PhysRevLett.108.076803. URL http://link.aps.org/doi/10.1103/PhysRevLett.108.076803.

[71] J. A. H. Stotz, R. Hey, P. V. Santos, and K. H. Ploog. Coherent spin transport through dynamic quantum dots. Nature Materials, 4:585–588, 2005.

[72] F. Alsina, P. V. Santos, H.-P. Schönherr, W. Seidel, K. H. Ploog, and R. Nötzel. Surface-acoustic-wave-induced carrier transport in quantum wires. Phys. Rev. B, 66 (16):165330, Oct 2002. doi: 10.1103/PhysRevB.66.165330.

[73] C. H. W. Barnes, J. M. Shilton, and A. M. Robinson. Quantum computation using electrons trapped by surface acoustic waves. Phys. Rev. B, 62(12):8410–8419, Sep 2000. doi: 10.1103/PhysRevB.62.8410.

[74] V. I. Talyanskii, J. M. Shilton, M. Pepper, C. G. Smith, C. J. B. Ford, E. H. Linfield, D. A. Ritchie, and G. A. C. Jones. Single-electron transport in a one-dimensional channel by high-frequency surface acoustic waves. Phys. Rev. B, 56(23):15180–15184, Dec 1997. doi: 10.1103/PhysRevB.56.15180.

[75] J. Cunningham, V. I. Talyanskii, J. M. Shilton, M. Pepper, M. Y. Simmons, and D. A. Ritchie. Single-electron acoustic charge transport by two counterpropagating surface acoustic wave beams. Phys. Rev. B, 60(7):4850–4855, Aug 1999. doi: 10.1103/PhysRevB.60.4850.

[76] Michihisa Yamamoto, Shintaro Takada, Christopher Bäuerle, Kenta Watanabe, Andreas D Wieck, and Seigo Tarucha. Electrical control of a solid-state flying qubit. Nature Nanotech., 7(4):247–51, Feb 2012. doi: 10.1038/nnano.2012.28.

[77] A. Aharony, S. Takada, O. Entin-Wohlman, M. Yamamoto, and S. Tarucha. Aharonov-Bohm interferometry with a tunnel-coupled wire. cond-mat, 12 2013. URL http://arxiv.org/abs/1312.5177.

[78] Tobias Bautze, Christoph Süssmeier, Shintaro Takada, Christoph Groth, Tristan Meunier, Michihisa Yamamoto, Seigo Tarucha, Xavier Waintal, and Christopher Bäuerle. From numerical to real experiments: a study of a solid state implementation of a flying qubit. cond-mat, 12 2013. URL http://arxiv.org/abs/1312.5194.

[79] Luka Trifunovic, Oliver Dial, Mircea Trif, James R. Wootton, Rediet Abebe, Amir Yacoby, and Daniel Loss. Long-Distance Spin-Spin Coupling via Floating Gates. Phys. Rev. X, 2:011006, Jan 2012. doi: 10.1103/PhysRevX.2.011006. URL http://link.aps.org/doi/10.1103/PhysRevX.2.011006.

[80] Yang Ji, Yunchul Cung, D. Sprinzak, M. Heiblum, D. Mahalu, and Hadas Shtrikman. An electronic Mach-Zehnder interferometer. Nature, 422:415, March 2003.

[81] Preden Roulleau, F. Portier, P. Roche, A. Cavanna, G. Faini, U. Gennser, and D. Mailly. Direct Measurement of the Coherence Length of Edge States in the Integer Quantum Hall Regime. Phys. Rev. Lett., 100:126802, Mar 2008. doi: 10.1103/PhysRevLett.100.126802. URL http://link.aps.org/doi/10.1103/PhysRevLett.100.126802.

[82] P. Samuelsson, E. V. Sukhorukov, and M. Büttiker. Two-Particle Aharonov-Bohm Effect and Entanglement in the Electronic Hanbury Brown–Twiss Setup. Phys. Rev. Lett., 92:026805, Jan 2004. doi: 10.1103/PhysRevLett.92.026805. URL http://link.aps.org/doi/10.1103/PhysRevLett.92.026805.

[83] Leo Yu and Oleksandr Voskoboynikov. Ballistic Aharonov–Bohm quantum bits and quantum gates. Solid State Communications, 145(9–10):447 – 450, 2008. ISSN 0038-1098. doi: http://dx.doi.org/10.1016/j.ssc.2007.12.017. URL http://www.sciencedirect.com/science/article/pii/S0038109807008861.

[84] M. D. BLUMENTHAL, B. KAESTNER, L. LI, S. GIBLIN, T. J. B. M. JANSSEN, M. PEPPER, D. ANDERSON, G. JONES, and D. A. RITCHIE. Gigahertz quantized charge pumping. Nature. Phys., 3(582):343–47, MAY 2007.

[85] G. Fève, A. Mahe, J.-M. Berroir, T. Kontos, B. Placais, D. C. Glattli, A. Cavanna, B. Etienne, and Y. Jin. An On-Demand Coherent Single-Electron Source. Science, 316(5828):1169–1172, 2007. URL http://www.sciencemag.org/content/316/5828/1169.abstract.

[86] Henning Schomerus and John P Robinson. Entanglement between static and flying qubits in an Aharonov–Bohm double electrometer. New Journal of Physics, 9(3):67, 2007. URL http://stacks.iop.org/1367-2630/9/i=3/a=067.

[87] P. G. Silvestrov and Y. Imry. Enhanced Sensitivity of the Transmission Phase of a Quantum Dot to Kondo Correlations. Phys. Rev. Lett., 90:106602, Mar 2003. doi: 10.1103/PhysRevLett.90.106602. URL http://link.aps.org/doi/10.1103/PhysRevLett.90.106602.

[88] Yang Ji, M. Heiblum, and Hadas Shtrikman. Transmission Phase of a Quantum Dot with Kondo Correlation near the Unitary Limit. Phys. Rev. Lett., 88(7):076601, Jan 2002. doi: 10.1103/PhysRevLett.88.076601.

[89] Masahiro Sato, Hisashi Aikawa, Kensuke Kobayashi, Shingo Katsumoto, and Yasuhiro Iye. Observation of the Fano-Kondo Antiresonance in a Quantum Wire with a Side-Coupled Quantum Dot. Phys. Rev. Lett., 95(6):066801, Aug 2005. doi: 10.1103/PhysRevLett.95.066801.

[90] S. Katsumoto, H. Aikawa, M. Eto, and Y. Iye. Tunable Fano-Kondo effect in a quantum dot with an Aharonov-Bohm ring. Phys. Stat. Sol., 3(12):4208–4213, 2006.

[91] Assaf Carmi, Yuval Oreg, Micha Berkooz, and David Goldhaber-Gordon. Transmission phase shifts of Kondo impurities. Phys. Rev. B, 86:115129, Sep 2012. doi: 10.1103/PhysRevB.86.115129. URL http://link.aps.org/doi/10.1103/PhysRevB.86.115129.

[92] Yasuhiro Niimi, Yannick Baines, Thibaut Capron, Dominique Mailly, Fang-Yuh Lo, Andreas D. Wieck, Tristan Meunier, Laurent Saminadayar, and Christopher Bäuerle. Quantum coherence at low temperatures in mesoscopic systems: Effect of disorder. Phys. Rev. B, 81:245306, Jun 2010. doi: 10.1103/PhysRevB.81.245306. URL http://link.aps.org/doi/10.1103/PhysRevB.81.245306.

[93] F. Mallet, J. Ericsson, D. Mailly, S. Ünlübayir, D. Reuter, A. Melnikov, A. D. Wieck, T. Micklitz, A. Rosch, T. A. Costi, L. Saminadayar, and C. Bäuerle. Scaling of the Low-Temperature Dephasing Rate in Kondo Systems. Phys. Rev. Lett., 97:226804, Nov 2006. doi: 10.1103/PhysRevLett.97.226804. URL http://link.aps.org/doi/10.1103/PhysRevLett.97.226804.

[94] A. Aharony, O. Entin-Wohlman, B. I. Halperin, and Y. Imry. Phase measurement in the mesoscopic Aharonov-Bohm interferometer. Phys. Rev. B, 66:115311, Sep 2002. doi: 10.1103/PhysRevB.66.115311. URL http://link.aps.org/doi/10.1103/PhysRevB.66.115311.

[95] Hisashi Aikawa, Kensuke Kobayashi, Akira Sano, Shingo Katsumoto, and Yasuhiro Iye. Interference Effect in Multilevel Transport through a Quantum Dot. Journal of the Physical Society of Japan, 73(12):3235–3238, 2004. doi: 10.1143/JPSJ.73.3235. URL http://jpsj.ipap.jp/link?JPSJ/73/3235/.

[96] U. Fano. Effects of Configuration Interaction on Intensities and Phase Shifts. Phys. Rev., 124:1866–1878, Dec 1961. doi: 10.1103/PhysRev.124.1866. URL http://link.aps.org/doi/10.1103/PhysRev.124.1866.

[97] Kensuke Kobayashi, Hisashi Aikawa, Shingo Katsumoto, and Yasuhiro Iye. Tuning of the Fano Effect through a Quantum Dot in an Aharonov-Bohm Interferometer. Phys. Rev. Lett., 88(25):256806, Jun 2002. doi: 10.1103/PhysRevLett.88.256806.

[98] Kensuke Kobayashi, Hisashi Aikawa, Shingo Katsumoto, and Yasuhiro Iye. Mesoscopic Fano effect in a quantum dot embedded in an Aharonov-Bohm ring. Phys. Rev. B, 68:235304, Dec 2003. doi: 10.1103/PhysRevB.68.235304. URL http://link.aps.org/doi/10.1103/PhysRevB.68.235304.

[99] Kensuke Kobayashi, Hisashi Aikawa, Akira Sano, Shingo Katsumoto, and Yasuhiro Iye. Fano resonance in a quantum wire with a side-coupled quantum dot. Phys. Rev. B, 70:035319, Jul 2004. doi: 10.1103/PhysRevB.70.035319. URL http://link.aps.org/doi/10.1103/PhysRevB.70.035319.

[100] J. S. Bell. ON THE EINSTEIN PODOLSKY ROSEN PARADOX. Physics, 1(3):195–200, Nov 1964.

[101] Gregor Weihs, Thomas Jennewein, Christoph Simon, Harald Weinfurter, and Anton Zeilinger. Violation of Bell's Inequality under Strict Einstein Locality Conditions. Phys. Rev. Lett., 81:5039–5043, Dec 1998. doi: 10.1103/PhysRevLett.81.5039. URL http://link.aps.org/doi/10.1103/PhysRevLett.81.5039.

[102] M. A. Rowe, D. Kielpinski, V. Meyer, C. A. Sackett, W. M. Itano, C. Monroe, and D. J. Wineland. Experimental violation of a Bell's inequality with efficient detection. Nature, 409(6822):791–794, 02 2001. URL http://dx.doi.org/10.1038/35057215.

[103] D. N. Matsukevich, P. Maunz, D. L. Moehring, S. Olmschenk, and C. Monroe. Bell Inequality Violation with Two Remote Atomic Qubits. Phys. Rev. Lett., 100(15):150404, Apr 2008.

[104] Markus Ansmann, H. Wang, Radoslaw C. Bialczak, Max Hofheinz, Erik Lucero, M. Neeley, A. D. O'Connell, D. Sank, M. Weides, J. Wenner, A. N. Cleland, and John M. Martinis. Violation of Bell's inequality in Josephson phase qubits. Nature, 461(08363):504–506, SEPTEMBER 2009.

[105] M. Kataoka, C.H.W. Barnes, C.J.B. Ford, H.E. Beere, D.a. Ritchie, D. Anderson, G.a.C. Jones, and M. Pepper. Single-electron transfer between double quantum dots defined by surface acoustic waves. Physica E: Low-dimensional Systems and Nanostructures, 34(1-2):546–549, August 2006. ISSN 13869477. doi: 10.1016/j.physe.2006.03.030. URL http://linkinghub.elsevier.com/retrieve/pii/S1386947706001573.

[106] M. Kataoka, M. Astley, a. Thorn, D. Oi, C. Barnes, C. Ford, D. Anderson, G. Jones, I. Farrer, D. Ritchie, and M. Pepper. Coherent Time Evolution of a Single-Electron Wave Function. Physical Review Letters, 102(15):1–4, April 2009. ISSN 0031-9007. doi: 10.1103/PhysRevLett.102.156801. URL http://link.aps.org/doi/10.1103/PhysRevLett.102.156801.

[107] Janine Splettstoesser, Sveta Ol'khovskaya, Michael Moskalets, and Markus Büttiker. Electron counting with a two-particle emitter. Phys. Rev. B, 78:205110, Nov 2008. doi: 10.1103/PhysRevB.78.205110. URL http://link.aps.org/doi/10.1103/PhysRevB.78.205110.

[108] M. Field, C. G. Smith, M. Pepper, D. A. Ritchie, J. E. F. Frost, G. A. C. Jones, and D. G. Hasko. Measurements of Coulomb blockade with a noninvasive voltage probe. Phys. Rev. Lett., 70:1311–1314, Mar 1993. doi: 10.1103/PhysRevLett.70.1311. URL http://link.aps.org/doi/10.1103/PhysRevLett.70.1311.

[109] Hendrik Bluhm, Sandra Foletti, Izhar Neder, Mark Rudner, Diana Mahalu, Vladimir Umansky, and Amir Yacoby. Dephasing time of GaAs electron-spin qubits coupled to a nuclear bath exceeding 200[thinsp][mu]s. Nat Phys, 7(2):109–113, 02 2011. URL http://dx.doi.org/10.1038/nphys1856.

[110] T. Meunier, I. T. Vink, L. H. Willems van Beveren, K-J. Tielrooij, R. Hanson, F. H. L. Koppens, H. P. Tranitz, W. Wegscheider, L. P. Kouwenhoven, and L. M. K. Vandersypen. Experimental Signature of Phonon-Mediated Spin Relaxation in a Two-Electron Quantum Dot. Phys. Rev. Lett., 98:126601, Mar 2007. doi: 10.1103/PhysRevLett.98.126601. URL http://link.aps.org/doi/10.1103/PhysRevLett.98.126601.

[111] Dik Bouwmeester, Jian-Wei Pan, Klaus Mattle, Manfred Eibl, Harald Weinfurter, and Anton Zeilinger. Experimental quantum teleportation. Nature, 390(6660):575–579, 12 1997. URL http://dx.doi.org/10.1038/37539.

[112] M. D. Barrett, J. Chiaverini, T. Schaetz, J. Britton, W. M. Itano, J. D. Jost, E. Knill, C. Langer, D. Leibfried, R. Ozeri, and D. J. Wineland. Deterministic quantum teleportation of atomic qubits. Nature, 429(6993):737–739, 06 2004. URL http://dx.doi.org/10.1038/nature02608.

[113] M. Riebe, H. Haffner, C. F. Roos, W. Hansel, J. Benhelm, G. P. T. Lancaster, T. W. Korber, C. Becher, F. Schmidt-Kaler, D. F. V. James, and R. Blatt. Deterministic quantum teleportation with atoms. Nature, 429(6993):734–737, 06 2004. URL http://dx.doi.org/10.1038/nature02570.

[114] R. M. Stevenson, R. J. Young, P. Atkinson, K. Cooper, D. A. Ritchie, and A. J. Shields. A semiconductor source of triggered entangled photon pairs. Nature, 439 (7073):179–182, 01 2006. URL http://dx.doi.org/10.1038/nature04446.

[115] S. Gustavsson, R. Leturcq, B. Simovič, R. Schleser, T. Ihn, P. Studerus, K. Ensslin, D. C. Driscoll, and A. C. Gossard. Counting Statistics of Single Electron Transport in a Quantum Dot. Phys. Rev. Lett., 96:076605, Feb 2006. doi: 10.1103/PhysRevLett.96.076605. URL http://link.aps.org/doi/10.1103/PhysRevLett.96.076605.

[116] Kenneth G. Wilson. The renormalization group: Critical phenomena and the Kondo problem. Rev. Mod. Phys., 47:773–840, Oct 1975. doi: 10.1103/RevModPhys.47.773. URL http://link.aps.org/doi/10.1103/RevModPhys.47.773.

[117] Ralf Bulla, Theo A. Costi, and Thomas Pruschke. Numerical renormalization group method for quantum impurity systems. Rev. Mod. Phys., 80:395–450, Apr 2008. doi: 10.1103/RevModPhys.80.395. URL http://link.aps.org/doi/10.1103/RevModPhys.80.395.

[118] Andreas Weichselbaum and Jan von Delft. Sum-Rule Conserving Spectral Functions from the Numerical Renormalization Group. Phys. Rev. Lett., 99:076402, Aug 2007. doi: 10.1103/PhysRevLett.99.076402. URL http://link.aps.org/doi/10.1103/PhysRevLett.99.076402.

[119] Andreas Weichselbaum. Non-abelian symmetries in tensor networks: A quantum symmetry space approach. Annals of Physics, 327(12):2972 – 3047, 2012. ISSN 0003-4916. doi: 10.1016/j.aop.2012.07.009. URL http://www.sciencedirect.com/science/article/pii/S0003491612001121.

[120] Yigal Meir and Ned S. Wingreen. Landauer formula for the current through an interacting electron region. Phys. Rev. Lett., 68:2512–2515, Apr 1992. doi: 10.1103/PhysRevLett.68.2512. URL http://link.aps.org/doi/10.1103/PhysRevLett.68.2512.

Appendix A

NRG calculations

A.1 Details of NRG calculations

We performed NRG calculations [116–119] using the generalized Anderson Hamiltonian [15, Eq. (1)]

$$H = \sum_{j,\sigma} \varepsilon_j n_{j,\sigma} + \frac{U}{2} \sum_{j,\sigma \neq j',\sigma'} n_{j,\sigma} n_{j',\sigma'} + \sum_{\alpha,k,\sigma} \varepsilon_k c^{\dagger}_{\alpha,k,\sigma} c_{\alpha,k,\sigma} + \sum_{j,\alpha,k,\sigma} (t^j_{\alpha} c^{\dagger}_{\alpha,k,\sigma} d_{j,\sigma} + \text{H.c.}) \quad \text{(A.1)}$$

,where $j = 1,2$ labels the dot levels, $\sigma = \uparrow, \downarrow$ describes the electron spin, $\alpha = \text{L}, \text{R}$ denotes the channel index, $\varepsilon_1 < \varepsilon_2$ are level positions, U is the Coulomb interaction strength, t^j_{α} are hopping amplitudes between level j and channel α, and ε_k denotes the dispersion relation of a flat band. To avoid a proliferation of parameters, we choose the magnitudes of the tunneling matrix elements to be left-right symmetric and level-independent, $|t^1_L| = |t^1_R| = |t^2_L| = |t^2_R|$, with relative sign $s = \text{sgn}(t^1_{\text{L}} t^1_{\text{R}} t^2_{\text{L}} t^2_{\text{R}})$, and characterize the overall coupling strength in terms of the parameter $\Gamma = (\pi\rho)/2\sum_{j,\alpha} |t^j_{\alpha}|^2$. As the magnetic field is smaller than all other energy scales, we have neglected its presence. Therefore, our calculations have fully exploited $\text{U}(1)$ charge and $\text{SU}(2)$ spin symmetries. The discretization parameter was set to $\Lambda = 4$, keeping approximately 6000 multiplets (corresponding to 20000 states) per iteration, which is required for the spinful two-channel calculation under consideration. NRG produces the correlation function of any pair of local operators; using Kramers-Kronig relations yields the full Green's function. Transmission amplitude and phase have been obtained from the complex quantity [15, Eq. (3)]

$$t_{d\sigma}(T) = \int \text{d}E \left(-\frac{\partial f_0(E,T)}{\partial E} \right) \sum_{j,j',\sigma} 2\pi\rho t^j_L t^{j'}_R \mathscr{G}^R_{j,\sigma;j',\sigma}(E,T). \quad \text{(A.2)}$$

For Figs. 3e-g in the main paper, where $s = +$, the conductance through the dot is calculated using $\sum_\sigma \mathrm{Im}[t_{d\sigma}(T)]$, which equals the prediction of the Meir-Wingreen formula [120].

A.2 Comparison between experimental data and NRG calculations

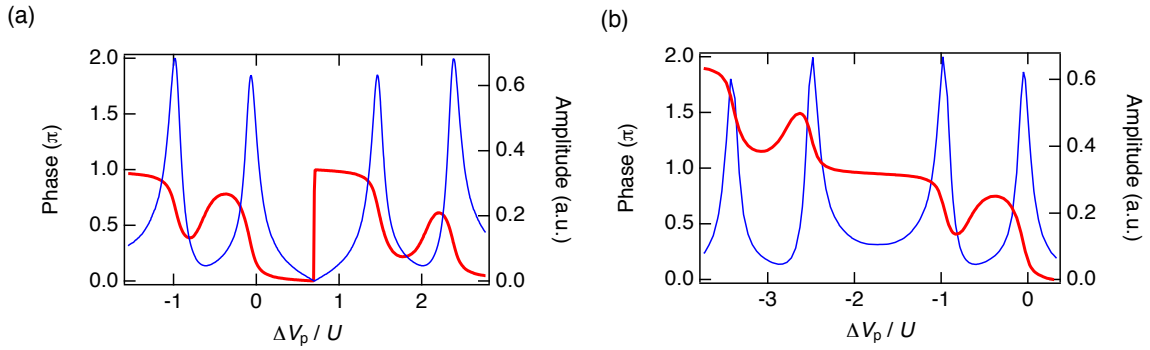

Fig. A.1 Transmission phase (red) and transmission amplitude (blue) of a quantum dot calculated by a two-level Anderson model in the weak Kondo regime ($T \gg T_\mathrm{K}$) for the case of $s = +$ (a) and $s = -$ (b). The fitting parameters, $\Gamma/U = 0.038$, $T/U = 0.0055$ and $\delta/U = 0.5$ were used for both (a) and (b).

In our fitting procedure in section 5.4 using the numerical calculations of a two-level Anderson model, fitting parameters are the tunnel-coupling coefficients t_α^j between the dot level j and the channel α, the single level spacing δ, the temperature T and the bandwidth of the leads D, which are all given in units of the charging energy U. In the whole fitting process D is fixed to 20 times bigger than U. Here the choice of D does not change the result when it is large enough compared to all the other parameters. To reduce the parameter space, we set $|t_L^1| = |t_R^1| = |t_L^2| = |t_R^2|$. Prior to the fitting, the charging energy U is first estimated. We obtained $U \sim 650$ μeV from the gate capacitance extracted from the Coulomb diamond at the base temperature and the Coulomb peak spacing at a temperature sufficiently high that the Kondo effect is so weak that the renormalization of the charging energy is negligible. Another important parameter to be fixed before fitting is the relative sign of the tunnel-coupling coefficient for neighboring energy levels, $s_j = \mathrm{sgn}(t_\mathrm{L}^j t_\mathrm{R}^j t_\mathrm{L}^{j+1} t_\mathrm{R}^{j+1})$. Figure A.1 shows transmission phase and amplitude calculated numerically by a two-level Anderson model at $T \gg T_\mathrm{K}$ for different signs of s. For $s = +$, a singular point called *transmission zero* [32] appears, which leads to a π-phase lapse and zero transmission amplitude when the Fermi

level lies symmetrically between the two different levels (Fig. A.1a). On the other hand for $s = -$, there is no such singular point and the phase smoothly evolves between two different levels (Fig. A.1b). We assume from the current around the Coulomb peaks shown in Fig. 5.3a the relative sign between the Kondo level (governing the Kondo valley in the conductance) and the next-higher (next-lower) levels at more positive (negative) V_p is $s_j = +$ ($s_j = -$). For our two-level Anderson model calculations, we therefore focus on the phase evolution of either a lower Kondo level with $s = +$, or an upper Kondo level with $s = -$ for comparison with the experimental data. This assumption is consistent with the asymmetry of the phase evolution in the weak Kondo regime of the experiment (Fig. 5.4d).

Here we describe the fitting procedure for $s = +$, whose results are presented in chapter 5. To determine the parameters used in Fig. 5.4f, we first fitted the data of Fig. 5.4c, where we can safely assume that the electron temperature is comparable to the fridge temperature of 110 mK, i.e. $T_e = 110$ mK. We then tune only fitting parameters, Γ and δ. To capture the most important feature of the phase evolution, we compared experimental data and calculations for the phase slope around the middle of the Kondo valley, $\Delta V_\mathrm{p} \sim 0.125$ V. To fit the experimental data, δ has to be large enough compared to Γ (i.e. $\delta/\Gamma \gg 1$) and we confirmed numerically that the precise value of δ only plays a minor role for the phase behavior, as long as $\delta > 0.4\,U$. We therefore fixed δ to $0.5\,U$. By varying Γ as a single fitting parameter, we obtained $\Gamma \sim 62.4\ \mu$eV. With these parameters, T_K is determined to be approximately 50 mK. The Kondo temperature is calculated by $T_\mathrm{K} = \chi_0/4$, where χ_0 is the local spin susceptibility at zero temperature.. Let us emphasize that a different choice of δ does not lead to a significant change in T_K, instead, it leads to a slightly different value of Γ. In such a way a very similar T_K-value is obtained. The phase evolution at this temperature therefore allows for a precise evaluation of T_K, with an uncertainty of ± 10 mK.

To determine the parameters used in Fig. 5.4e, we proceeded as follows: with $\Gamma = 62.4\ \mu$eV and $\delta = 325\ \mu$eV, temperature is then lowered as a fitting parameter to fit the phase curve in Fig. 5.4b. We note that for these Γ/U values the $\pi/2$-plateau has still a finite and temperature dependent slope, even at zero temperature. This allows for a relatively precise determination of the electron temperature of about 40 mK, somewhat higher than the fridge base temperature, but in good agreement with former measurements on 2DEGs in the same electromagnetic environment [92].

Finally, to determine the parameters used in Fig. 5.4g, we proceeded as follows: with $T = 40$ mK and $\delta = 325\ \mu$eV, Γ is varied to fit the data in Fig. 5.4d. The data is fit best for $\Gamma = 24.7\ \mu$eV. The determination of the exact Kondo temperature in this weak Kondo regime is more delicate as the exponential dependence on Γ/U leads to relatively large

uncertainties. Nevertheless we estimate T_K to be more than 30 times smaller than the actual electron temperature. Finally let us mention that the values for Γ extracted from the NRG fitting are much smaller than if one would take simply the width of the CPs (in our case $24.7\mu eV$ compared to $130\mu eV$). The asymmetry in the phase evolution in Fig. 5.4g around $\Delta V_p/U = -0.5$ originates from the influence of the nearby level and reflects the orbital parity, $s_j = +$. We also performed the same fitting procedure with the other choice of sign, $s_j = -$, which led to very similar parameters.

For both fitting procedures we get remarkable agreement between the experimental data and the NRG calculations for the phase evolution. The $\pi/2$-phase shift persisting up to T_K (Fig. 5.4b) clearly indicates that coherent current flows through the Kondo resonance once a localized spin is formed in the quantum dot for $T \leq T_K$. Compared to the phase, agreement between the current I_2 in the experiment and the conductance G in the calculations is not as good. This may arise from several reasons: one possibility is that in our calculation we did not include left-right asymmetry of the tunnel-coupling between the leads and the quantum dot whereas for the actual quantum dot this asymmetry exists. Another possible reason is that in the experiment there is a linear background from the upper path of the interferometer whereas the calculated conductance G does not contain such a contribution.

In the V_p regime in which the current I_2 shows the Coulomb blockade peak on the right, the phase decrease towards zero with increasing V_p occurs somewhat sooner (relative to the position of the Coulomb peak) for the experimental data in Fig. 5.4c and d than for the NRG calculations in Fig. 5.4f and g. This deviation between experiment and theory in the tails of the phase curve may be due to the fact that we experimentally extract the phase from the *coherent*âĂă part of the current whereas the *total* current I_2 that is plotted in Figs. 5.4b - d also contains the incoherent part. In this context, further theoretical studies are necessary.